

ABSTRACT

ARTNER, MIRELA ANGELITA. Understanding the Processing-Structure-Properties Relationship of Cellulose Nanofibrils Towards a High-Quality Grade for Packing Applications (Under the direction of Dr. Nathalie Lavoine and Dr. Melissa A. Pasquinelli).

Polymers derived from fossil fuels have been largely used in the preservation of food products. However, conventional plastics used as food packaging materials have caused environmental pollution on land and sea. An increased interest in using biomass for packaging applications is thus growing as it provides a platform for the design and engineering of sustainable alternatives to petroleum-based materials. In this dissertation, the potential of cellulose nanofibrils (CNFs) isolated from wood pulp to replace some of the petroleum-derived plastic materials used in food packaging, is explored. Despite significant research and development efforts in CNFs, some technological gaps still limit their transition from laboratory to marketplace. End-users are hesitant to adopt CNFs due to high costs compared to traditional plastics used in packaging and a lack of awareness about CNFs' applications and performance, particularly concerning water and moisture barriers. Despite numerous strategies, including pre- and post-treatment of CNFs, achieving the required water barrier performance for food packaging remains challenging. Therefore, our research focuses on understanding the process-structure-performance relationships of CNFs. Our strategy is to explore each stage of production, from the influence of the raw materials and processing conditions to post-production functionalization to understand how these different steps influence the performance of CNFs, and how they can be optimized to enhance the barrier of CNF films against water and moisture barrier for packaging applications.

The first part of this research (Chapter 2) investigates a still-unexplored production route for CNFs: the use of an Aqueous Counter Collision (ACC), a high-shear

mechanical equipment that has shown promise in the individualization of macroscale fibers into their elementary fibril structure. This chapter specifically focuses on the processing-properties relationship of CNFs. According to the literature, varying the processing conditions of biomass to produce CNF suspensions has been shown to result in CNF grades with distinct properties. Controlling these processing conditions to enable the production of a specific CNF grade remains, however, a challenge. In this Chapter, we investigated the processing conditions that would result in the production of a high-quality grade of CNFs for packaging applications, and specifically in the engineering of CNF films with high tensile strength and low water vapor permeability. This research revealed that it is not possible to endow CNF films with both a high tensile strength and a high moisture barrier using one set of processing parameters only. Varying the mechanical shearing action applied to the cellulosic fibers upon processing impacted the morphology of the CNFs, and in turn their interaction and entanglement upon water evaporation. While the tensile strength of CNF films is influenced by the nanofibrils' morphology, the moisture barrier properties rely on the density, inter-nanofibril interactions, and their interaction with moisture. This study also demonstrated that the moisture barriers achieved by processing only were not sufficient for packaging application; hence, another strategy is needed to endow CNF films with competitive moisture barrier.

The second part of this work (Chapter 3) investigates the post-chemical surface modification of CNF films by plasma; a sustainable processing that aims to solely alter the surface properties of the films while preserving their bulk properties. Surface modification by plasma does not rely on the use of solvents and can be performed at atmospheric pressure and low temperature. In this chapter, CNF films were functionalized by the deposition of an organosilicon layer using a dielectric barrier discharge plasma. Two main approaches were

investigated to enhance the barrier performance of the films: (i) the identification of process parameters that resulted in the uniform deposition of a hydrophobic layer using 2,4,6,8-tetramethylcyclotetrasiloxane (TMCTS) fragments on the CNF films' surface and (ii) the creation of a multilayer structure made of tailored, successive, hydrophilic, and hydrophobic layers. The CNF films were endowed with a superhydrophobic surface, and their barrier against water absorption and water vapor transmission were considerably improved by >100% and 15%, respectively. This study contributed to deciphering the effect of plasma treatment on the surface chemistry and topography of nanocellulosic materials with the goal of proposing a scalable, sustainable, and effective solution for advanced materials development.

The third part of this research (Chapter 4) builds on the outcomes of the second and third chapters and aims to investigate the influence of biomass chemistry on the CNF films' properties. Previous chapters have suggested that the water vapor transmission rate and its optimization depend on both the surface and bulk properties of the CNF films. Literature has shown that lignin can enhance the performance of CNFs and/or play a significant role in the processing of biomass. Hence, Chapter 4 investigates the bulk structure of CNFs, and more precisely attempts to elucidate how variations in chemical composition of the woody biomass may affect the defibrillation performance of lignocellulosic fibers, as well as the structure and properties of the resulting CNFs. The novelty of this chapter relies on the use of CRISPR-Cas genome edited trees as raw materials for CNF production, which offer a platform to tailor and tune the chemical composition of wood. This chapter demonstrated that higher carbohydrate-to lignin (C/L) ratio, and CRISPR-modified lignin, contributed to a 25% reduction in the energy consumption required for CNF production. The moisture barrier was compromised by

the high C/L ratios; however, the CNF presented a high degree of fibrillation, enhanced mechanical performance.

This dissertation explores the potential of CNFs for packaging applications through variations in process conditions, chemical surface modifications, and biomass chemistry. We elucidated that these elements should be evaluated prior to any pre- or post-treatment of CNFs. This work demonstrates that CNFs derived from wood pulp can serve as a sustainable alternative to petroleum-based plastics.

© Copyright 2024 by Mirela Angelita Artner

All Rights Reserved

Understanding the Processing-Structure-Properties Relationship of Cellulose Nanofibrils
towards a High-Quality Grade for Packaging Applications.

by
Mirela Angelita Artner

A dissertation submitted to the Graduate Faculty of
North Carolina State University
in partial fulfillment of the
requirements for the degree of
Doctor of Philosophy

Forest Biomaterials

Raleigh, North Carolina
2024

APPROVED BY:

Dr. Nathalie Lavoine
Committee Co-Chair

Dr. Melissa A. Pasquinelli
Committee Co-Chair

Dr. Joel Pawlak

Dr. Jacopo Profili

Dr. Jack P. Wang
Graduate School Representative

DEDICATION

To my grandmothers, mom, and sister.

Eu dedico essa tese para as minha avós, mãe e irmã.

BIOGRAPHY

Mirela Artner was born March 24, 1991, in Santa Catarina, Brazil. She graduated from Universidade Federal de Santa Catarina in August of 2016 with a Bachelor of Science degree in Industrial Chemistry. During her junior year, Mirela worked as a quality control intern in the Department of Food Science at the Federal University of Santa Catarina. During her senior year, Mirela joined Núcleo Ressacada: Environmental Research Center for two years as an intern. After graduation, she worked for three years as a R&D Scientist at one of the largest thermoset polymers producers in Latin America. In 2018, she joined the Department of Materials Science and Engineering at the Federal University of Parana and earn her Master of Science in 2020. In 2021, Mirela joined the Department of Forest Biomaterials at North Carolina State University under the supervision of Dr. Nathalie Lavoine and Dr. Melissa A. Pasquinelli. During her Ph.D., she had the opportunity to join the Laboratoire d'Ingénierie de Surface, Centre de recherche du in Québec Canada for four months as a Graduate Research Assistant. Mirela is passionate about the interfaces between science, industry and commercialization, and will continue to build her expertise in this direction.

ACKNOWLEDGEMENT

I would like to express my gratitude to Dr. Nathalie Lavoine and Dr. Melissa A. Pasquinelli, for their encouraging guidance and advice in my research and throughout my Ph.D. journey. I would also like to thank my committee members, Dr. Joel Pawlak and Dr. Jacopo Profili and Dr. Jack Wang for their advice and assistance in my research.

To all my dear friends for the supporting words and patience. I could not make it without you. I am very grateful for all the connections I have made during this journey.

Finally, I give sincere thanks to my mom for being my inspiration, and to show me the meaning of “*Education is the best way to build a better life and future, and that knowledge is something that no one can take away from you.*” Finally, thank you to my family and boyfriend for waiting for me to finish this chapter of my life.

TABLE OF CONTENTS

LIST OF TABLES	viii
LIST OF FIGURES	x
CHAPTER 1	1
1.1. Introduction.....	1
1.2. Multilayer Flexible Packaging for Food.....	1
1.3. Exploring the Potential of Biomass at the Nanoscale.....	3
1.4. The potential of CNF films for packaging.....	4
1.5. The limitation: The use of CNFs for packaging application and its susceptibility to water and moisture.....	5
1.6. Strategy one, the processing: Production routes of cellulose nanofibrils	8
1.7. Strategy two, the surface: post-treatment.....	12
1.8. Strategy three, the bulk: Influence of biomass chemical composition on the production and properties of CNFs.....	14
1.9. Research Objectives.....	17
CHAPTER 2: Tailoring Cellulose Nanofibrils Films for Improved Performance through Optimization of Aqueous Counter Collision Processing Conditions.....	19
2.1. Abstract.....	19
2.2. Introduction.....	19
2.3. Materials and Method	23
2.3.1. Materials	23
2.3.2. Methods.....	23
Production of Cellulose Nanofibrils (CNFs)	23
Design of Experiment	24
Characterization of CNF suspension	25
Preparation of CNF films.....	26
Testing of CNF films	26
Surface accessibility of cellulose fibrils studied by hydrogen-deuterium exchange:	27
2.4. Results and Discussion.....	28
2.4.1. Design of Experiments.....	28
2.4.2. Fiber Morphology	29
2.4.3. Tensile Index of CNF Films	30
2.4.4. Water Vapor Permeability	32

2.4.5.	The CNF Surface study via D ₂ O.....	35
2.4.6.	Predictive Model and Optimization.....	37
2.4.7.	Response Surface Methodology (RSM).....	39
2.5.	Conclusions.....	40
CHAPTER 3: Tuning the Surface Chemistry and Properties of Cellulose Nanofibril (CNF) Films by Dielectric Barrier Discharge (DBD) Plasma for Packaging Applications		42
3.1.	Abstract.....	42
3.2.	Introduction.....	43
3.3.	Experimental Section.....	48
3.3.1.	Materials	48
3.3.2.	Production of Cellulose Nanofibril (CNF) and CNF Films.....	48
3.3.3.	Dielectric Barrier Discharge (DBD) Plasma Treatment	48
3.3.4.	Characterization of the TMCTS-plasma-induced coating	50
3.3.5.	Attenuated Total Reflectance Fourier Transformed Infrared Spectroscopy (ATR-FTIR)	51
3.3.6.	Water Contact Angle (WCA).....	51
3.3.7.	X-ray Photoelectron Spectroscopy (XPS)	51
3.3.8.	Atomic Force Microscopy (AFM)	52
3.3.9.	Water Vapor Transmission Rate (WVTR) and Water Uptake of CNF films	52
3.4.	Results and Discussion.....	53
3.4.1.	Influence of organosilicon plasma-induced deposition on CNF films' topography	53
3.4.2.	Influence of Plasma-Induced Fragmentation of TMCTS on CNF Films' Surface Properties	56
3.4.3.	Wetting Behavior of Plasma-Treated CNF films.....	60
3.4.4.	Plasma-induced organosilicon deposition in dynamic mode.....	61
3.4.5.	Surface chemistry of CNF films functionalized in dynamic mode.....	63
3.4.6.	Tuning the wettability of CNF films by multilayer plasma treatment.....	66
3.5.	Conclusions.....	74
CHAPTER 4: Exploring the role of biomass' chemical composition in the production and properties of lignin-containing cellulose nanofibrils (LCNFs) through CRISPR multiplex-edited hardwood		76
4.1.	Abstract.....	76
4.2.	Introduction.....	78

4.3. Experimental Section	82
4.3.1. Materials	82
4.3.2. Methods.....	82
4.3.3 Biomass feedstock	82
4.3.4. Micro Kraft pulping	83
4.4.5. Chemical composition analysis of biomass and pulps (Wet chemistry).....	83
4.4.6. Chemical analysis of biomass by 2D HSQC NMR	84
4.4.7 Determination of hydroxyl groups in Kraft pulps.....	85
4.4.8. Determination of Kraft pulp Water Retention Value (WRV):.....	86
4.4.9. Production of LCNF from the transgenic and wildtype poplar kraft pulps	86
4.4.10. Morphology of LCNF	86
4.4.11. Preparation of LCNF films	87
4.4.12. SEM- Cross section.....	87
4.4. 13. Grammage.....	87
4.4.14. Density	88
4.4.15. Mechanical performance of LCNF films in tensile mode.....	88
4.4.16. Water vapor transmission rate (WVTR):	88
4.5. Results and Discussion	89
4.5.1. Chemical structural alterations in transgenic poplars	89
4.5.2. Kraft pulping.....	92
4.5.3 Impact of Chemical Composition on Lignin-Containing Cellulose Nanofibrils (LCNFs) from Wildtype and CRISPR-Edited Kraft Pulps.....	94
4.5.4. Performance of LCNF films	99
4.5.5. How to explain similarities between CRISPR OKC and K3	104
Chapter 5. Conclusions and Future Work	110
References	112
APPENDICES	146
Appendix A: Supporting information for Chapter 2 Tailoring cellulose nanofibrils films for improved performance through optimization of aqueous counter collision processing conditions.....	147
Appendix B: Supporting information for Chapter 3: Tuning the Surface Chemistry and Properties of Cellulose Nanofibril (CNF) Films by Dielectric Barrier Discharge (DBD) Plasma for Packaging Applications	153

LIST OF TABLES

Table 1.1 Strategies to improve water vapor transmission rates and water contact angles of cellulosic materials.....	6
Table 2.1 Factors and design levels for the BBD	24
Table 2.2 Experimental design matrix for the BBD with the factors and respective design levels	25
Table 2.3 WVP, standard deviations, and density of CNF films processed in the ACC.....	34
Table 3.1 Average roughness (R_a) values of CNF films before and after plasma treatment at the position 1 cm (a1), 1.5 cm (a3) and 3 cm (a4) away from the reactor entrance. The average roughness values were measured by Atomic Force Microscopy.	55
Table 3.2 XPS percentage atomic concentrations of C1s components on the CNF films' surface after organosilicon deposition by plasma, in dynamic mode.....	65
Table 3.3 Average roughness (R_a) values of first TMCTS/ N_2 , second N_2O/N_2 and third plasma layer using TMCTS/ N_2 . The average roughness values were measured by Atomic Force Microscopy.	68
Table 3.4 Averages and standard deviations of XPS screenings of a first layer with TMCTS/ N_2 , second layer with N_2O/N_2 , and a third layer with TMCTS/ N_2	70
Table 4.1 Main components of biomass (cellulose, hemicelluloses, and total lignin) and Lignin composition (%) for syringyl (S) and guayacil (G) units and interunit linkages of wildtype and CRISPR edited hardwoods (HW).	90

Table 4.2 Structural and mechanical properties of LCNF films from wildtype and CRISPR- edited hardwoods	100
--	-----

LIST OF FIGURES

Figure 1.1 Example of multilayer film structure for packaging applications.	2
Figure 1.2. Examples of required WVTR values at 37.8°C, and 90% Relative Humidity (RH), for flexible multilayer packaging, and the current value for CNF films. (Adapted from Butler & Morris, 2009).	3
Figure 1.3 Illustration of the hierarchical structure of wood fibers in trees. (Adapted from Benitez & Walther, 2017).	4
Figure 1.4 Schematic illustration of processing, raw materials, and surface treatment of CNFs.	8
Figure 1.5 Conventional defibrillation methods of CNF: High-Pressure Homogenization, Microfluidization, and Grinding. (Reproduced from Nechyporchuk et al. 2016, Copyright © 2016, Elsevier Ltd.)	9
Figure 1.6 ACC ball-type chamber, in green color symbolizing the CNF suspension being injected into the chamber.	11
Figure 1.8 The multiple treatment steps from biomass to CNFs.	15
Figure 2.1 TEM of CNF processed under different conditions showing the increased defects when the number of passes is increased from 1 (left) to 6 (middle) and 11(right).....	29
Figure 2.2 Average tensile index of EC _{Low} -CNFs, A: combination of concentration and passes; B: Pressure and passes, C: concentration and pressure. Tensile index of EC _{High} -CNFs, D: concentration and passes, E: Pressure and passes, F: concentration and pressure. ...	31

Figure 2.3 Variation in water vapor permeability values of ECHigh-CNF films as a function of the processing conditions, A) concentration x number of passes, B) Jet pressure x number of passes, C) Concentration x Jet pressure. 34

Figure 2.4 FT-IR spectra of CNF films sample #4 (6p, 220MPa, 0.1 wt.%), #11 (11p, 220MPa, 0.33wt%) and #15 (6p, 220MPa) exposed to D₂O for 48h and one week..... 36

Figure 2.5 Predictive graph and maximum desirability to optimize processing conditions of EC-high-CNF. Red dotted lines mark the points of maximum tensile index and minimum WVP..... 38

Figure 2.6 a) Predictive response surface of the tensile index - EC-CNF_{High} in the function of concentration wt.% and passes; b) WVP in the function of pressure (MPa) and passes c) and passes and concentration wt.%..... 39

Figure 3.1 Schematic of the side view of the DBD plasma reactor. The inlet gases used as precursor carriers were injected on the upper left, at the entrance of the reactor. The different sample areas of deposition were labelled a0, a1, a2, a3, and a4, corresponding to a distance of 1, ~1.2, 1.5, and 3 cm away from the reactor entrance, respectively. 50

Figure 3.2 Scanning Electron Microscopy (SEM) images of CNF films' surface coated by organosilicon plasma in static mode. (A) Untreated CNF films (controls), plasma-treated CNF films functionalized at (B, F) 1.0 cm, (C) 1.2 cm, (D) 1.5 cm and (E) 3.0 cm away from the entrance of the reactor. Magnification: ×1000. 54

Figure 3.3 Infrared (IR) spectra of untreated CNF films and films treated by organosilicon plasma in a1, a2, a3, and a4 positions (i.e., 1 cm, ~1.2 cm, 1.5 cm, and 3 cm away from

the entrance of the reactor) between (A) 3600-800 cm^{-1} and (B) zoomed area from 2100 to 1200 cm^{-1} 57

Figure 3.4 Contour plot of the water contact angle values recorded across the surface area of the plasma-treated CNF films ($3 \times 3 \text{ cm}^2$). The top left corner of the plot ($y=0$) indicates the entrance of the DBD reactor and the bottom left corner ($y=3 \text{ cm}$), the exit of the reactor. The images of the water contact angle recorded at the position a1, a2, and a4 (*i.e.*, 1 cm, ~1.2 cm, and 3 cm away from the entrance of the reactor) are shown on the right of the contour plot. 61

Figure 3.5 SEM images of CNF films' surface after plasma functionalization in dynamic mode between the entrance and the exit of the reactor. (A) Position a1, 1 cm away from the reactor's entrance, (B) a3, 1.5 cm away, and (C) a4, 3 cm away. Magnification: $\times 500$. Inserts show the image of a water drop on the plasma-treated films' surface at positions a1, a3, and a4 with the respective measured contact angle values. 63

Figure 3.6 (A) Infrared spectra (FTIR-ATR) from 3600 to 800 cm^{-1} of the untreated CNF (green line), static mode area a1= 1cm (red line), and the layer treated at the dynamic mode (blue line) and (B) Deconvoluted Carbon 1s photoelectron spectrum of CNF films after organosilicon deposition by plasma in dynamic mode..... 64

Figure 3.7 SEM images of the organosilicon-coated CNF films' surface after (A) a second plasma layer using $\text{N}_2\text{O}/\text{N}_2$ and (B) a third plasma layer using TMCTS/ N_2 . Magnifications: (A) $\times 200$ and $\times 500$ (insert), (B) $\times 1000$ 67

Figure 3.8 Surface chemistry analysis of the organosilicon-coated (A) CNF films after deposition of a first layer with TMCTS/ N_2 , a second layer with $\text{N}_2\text{O}/\text{N}_2$, and a third layer

with TMCTS/N₂. Infrared spectra from 3600 to 800 cm⁻¹, and XPS photoelectroncarbon C_{1s} spectra of the (B) second layer and the (C) third layer. 70

Figure 3.9 Dynamic water contact angle analysis of the CNF films after 0, 3 and 10 seconds of contact with the water drop. (*left column*) Untreated CNF films' surface, CNF films after (*middle column*) two plasma layers (TMCTS/N₂ and N₂O/N₂), and (*right column*) three plasma layers (TMCTS/N₂ - N₂O/N₂ - TMCTS/N₂). 71

Figure 3.10 Water vapor transmission rates (g/m²day) and water absorption (%) of the untreated CNF films, and films functionalized by one (TMCTS/N₂), two (layer 1 + N₂O/N₂)..... 73

Figure 4.1 HSQC cross-signals of lignin Wildtype, CRISPR OC5, CRISPR OKC, and CRISPR K3. On the right it is represented the respective structures of the spectra A) Benzaldehyde, B) 2-methoxybenzaldehyde; C) 2-6 dimethoxybenzaldehyde..... 92

Figure 4.2 Pulping yields, Carbohydrates to lignin ratio (C/L), relative chemical composition of the Kraft pulps (does not include extractives, ashes and Hexenuronic acids) from the CRISPR-edited and wildtype poplar trees. Note: Total hemicelluloses include: Xylose, Mannose, Galactose and Arabinose. 93

Figure 4.3 Specific energy consumption to produce LCNFs from wildtype and CRISPR poplar kraft pulps in kWh per kg of oven dried (OD) Kraft pulp as a function of (A) hemicellulose and (B) lignin contents of the Kraft pulps. Transmission Electron Microscopy images of LCNFs from (C) wildtype kraft pulps and CRISPR-edited poplars (D) OC5, (E) OKC and (F) K3 . C/L is the carbohydrate-to-lignin ratio of the pulps calculated from Figure 96

Figure 4.4 Scanning Electron Microscopy (SEM) images of the cross section of films made from (A) Wildtype, (B) CRISPR OC5, (C) CRISPR K3, and (D) CRISPR OKC LCNFs 99

Figure 4.5 Water vapor transmission rate values of wildtype and CRISPR LCNF films, and carbohydrates to lignin ratio (C/L). ^{a-b} Values that do not share a letter are statistically different from one another ($p > 0.05$ level, one sample t-test). 103

Figure 4.6 Water retention values of wildtype and CRISPR Kraft pulps as a function of (A) Hemicelluloses (B) Lignin..... 105

Figure 4.7 (A) ³¹P NMR spectra of OH groups in lignin of the wildtype and CRISPR OKC sample (B) Quantitative analysis of wildtype and CRISPR OKC. The y-axis indicates the amount of group (in mmol/g). The bar column represents the condensed phenolic OH (Con. Phenolic OH) shown in blue, total phenolic OH (Total PhOH) in orange, and total carboxylic OH (Total COOH) in green. 107

CHAPTER 1

1.1. Introduction

Polymers derived from fossil fuels have been largely utilized in the preservation of packaged food products (Han et al., 2018). However, conventional plastics used as food packaging materials have caused environmental pollution on land and sea (Mahardika et al., 2023). In 2021, ~6 million tons of plastic packaging were produced in the U.S.A, of which only 2.2 million tons of packaging were labelled as sustainable, and 13.3% out of these ended up being recycled. By 2025, the goal is to increase recycling rates to 50% and rethink packaging designs to include more recyclable and biobased materials in their compositions (U.S. Plastic Pact: 2021 Annual report). Particularly, multilayer packaging presents significant recycling challenges due to the complexity of separating its layers, complicating efforts to reduce environmental impact (Kaiser et al., 2018).

1.2. Multilayer Flexible Packaging for Food

Multilayer flexible packaging structures represent one of the most significant developments of packaging technology, and one of the most impacted categories by the end-of-life challenges, due to the difficulty of separating the layers for recycling (Bauer et al., 2021). These structures are produced by combining several types of plastics film materials or plastics and non-plastics materials, and therefore, have properties that cannot be found in one specific starting material (Fávaro et al., 2013a). Multilayer food packaging can consist of 3 to 7 different layers (Anukiruthika et al., 2020). Commonly used materials in multilayers flexible packaging include (i) polyethylene terephthalate (PET) which provides stability and protection against moisture and liquids such oil and grease; (ii) polyurethanes (PU) which promote the

adhesion between different layers and (iii) barrier layers such as aluminum foil, which serves as an oxygen and light barrier to maintain the nutritional value and flavors of the contents, or polyethylene (PE) and polypropylene (PP) for moisture protection (**Figure 1-1**) (Bauer et al., 2021; Kaiser et al., 2018). Although the flexible multilayer packaging offers benefits with respect to performance, the technology to separate these thin layers for proper recycling is not yet available (Bauer et al., 2021). For example, PE and PET are incompatible during mechanical recycling, which can degrade the quality of the recovered product. Another issue is that heterogeneous polymers, such as polyolefins, can get contaminated during thermochemical recycling by other polymers such as PET, polyamide (PA), and polycarbonate (PC), leading to their eventual disposal in landfills or incineration (Ügdüler et al., 2021).

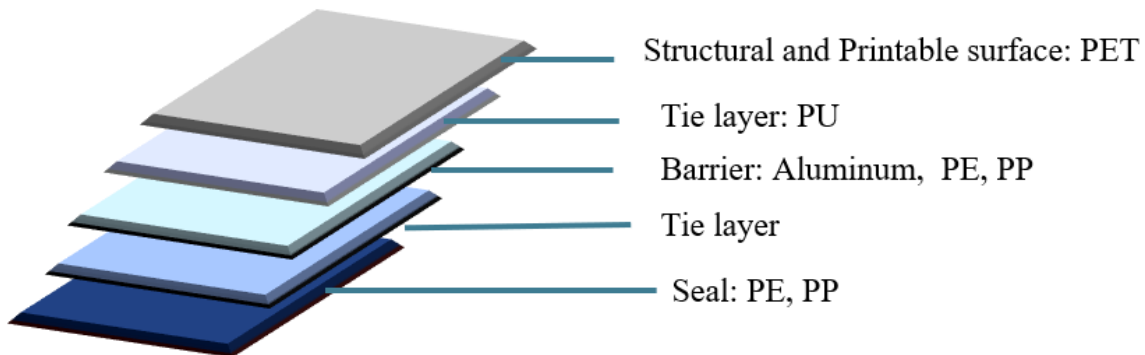


Figure 1.1 Example of multilayer film structure for packaging applications.

Several research efforts have been directed toward developing recyclable and/or biodegradable multilayer systems that can replace current petroleum-derived commercial substrates (Koppolu et al., 2019; Pasquier et al., 2022; Wang et al., 2022). Although there is an urge to replace fossil fuels-derived products with alternatives from renewable resources, food packaging must meet specific, and often strict, specifications to enable their contact with food products and safe preservation and extension of the food shelf life. Such specifications

include excellent barrier against light, moisture, oxygen, and grease, and mechanical strength performance (Butler & Morris, 2009). The requirements for food packaging vary with the type of food products to package; for instance, dry food, such as chips or crackers, are sensitive to moisture, hence the packaging needs to have low Water Vapor Transmission Rate (WVTR) values. Some of these required values are listed in Figure 1.2.

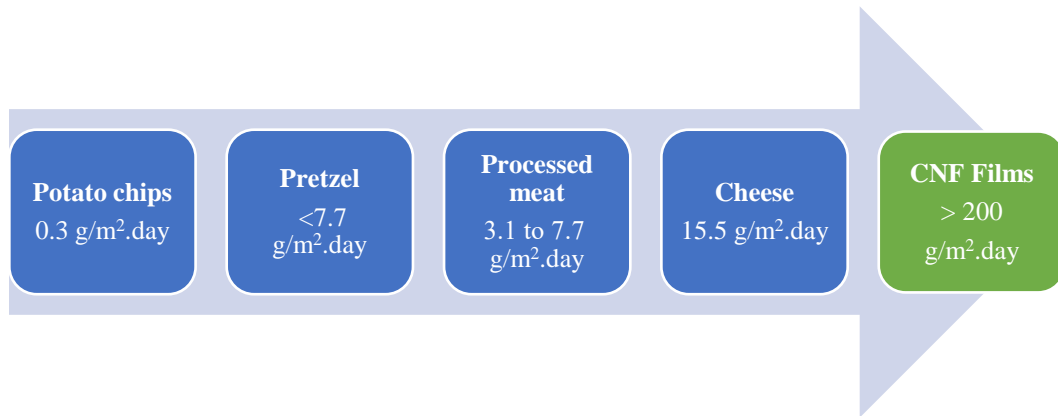


Figure 1.2. Examples of required WVTR values at 37.8°C, and 90% Relative Humidity (RH), for flexible multilayer packaging, and the current value for CNF films. (Adapted from Butler & Morris, 2009).

The primary goal of this work is to investigate the potential of wood pulp derived Cellulose Nanofibrils (CNFs) as a biobased alternative that can serve of single layer in multilayer packaging applications. The following section will introduce CNFs and highlight the main challenges, knowledge, and technical gaps pertaining to research on cellulose nanofibrils, that this research aims to address.

1.3. Exploring the Potential of Biomass at the Nanoscale

Plant biomass is primarily composed of cellulose (39-45%), hemicellulose (17-35%), and lignin (20-25%) (Solala et al., 2020). When unraveling the structure of the wood cellulosic

fibers, one observes an organized hierarchical cellulosic structure surrounded by a matrix of hemicelluloses and lignin. This structure results from the assembly of cellulose microfibrils, which are themselves composed of elementary fibrils. These fibrils, referred to as individualized CNFs, consist of each of the assembly of linear homopolysaccharides of β -1,4-linked anhydro-D-glucopyranose (**Figure 1.3**) (Benítez & Walther, 2017). CNFs can be extracted from lignocellulosic biomass dispersed in water that is defibrillated through high mechanical shear. CNFs can be described as long, flexible fibers, comprising of both crystalline and amorphous regions. According to TAPPI WI 3021, CNFs have a diameter in the range of 5-30 nm and an aspect ratio greater than 50 (meaning a length $>1 \mu\text{m}$).

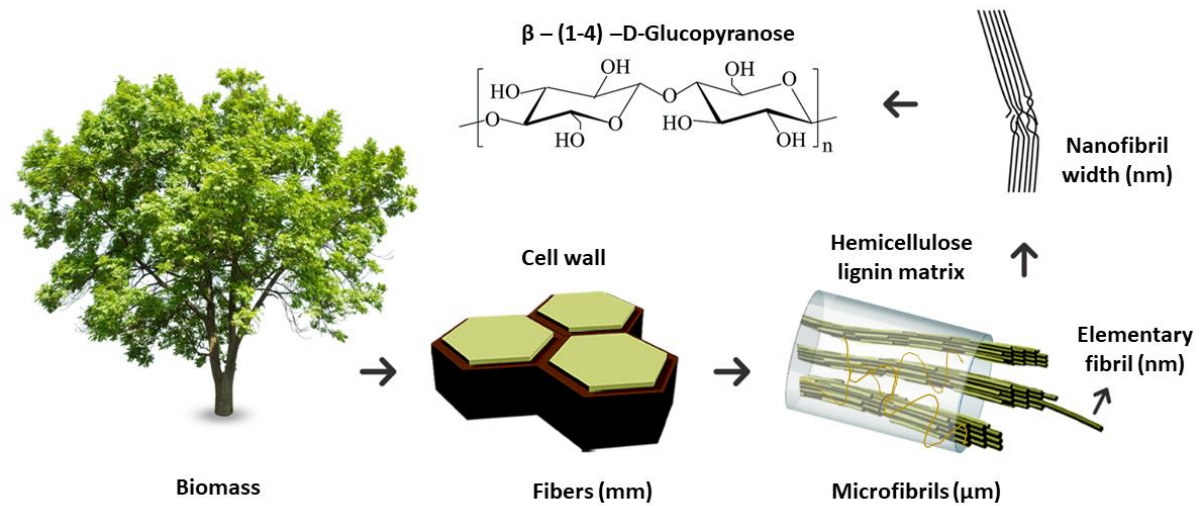


Figure 1.3 Illustration of the hierarchical structure of wood fibers in trees. (Adapted from Benitez & Walther, 2017).

1.4. The potential of CNF films for packaging

When the dispersed CNF suspension is dried, the cohesive forces between the nanofibrils form CNF films with competitive and attractive mechanical properties. For example, Polylactic Acid (PLA) films and PET exhibit a tensile strength of around 50 MPa

(Wu et al., 2023), whereas CNF films demonstrated a tensile strength exceeding 100 MPa (Mokhena et al., 2021a). Additionally, CNF films have great barrier properties against grease, and oxygen, making them a promising candidate for packaging applications (Solala et al., 2020). As in the multilayer systems, the CNF films have also been applied as a single layer in a synergistic combination with other materials, such as biobased-polyethylene layers (Vähä-Nissi et al., 2017), wax (Österberg et al., 2013; Pasquier et al., 2022), low density polyethylene (Vartiainen et al., 2018), chitosan and PLA (Vähä-Nissi et al., 2017).

Yet, after years of research in this field, CNF-based packaging substrates have still not reached the marketplace, despite the large-scale production and global availability of this material, estimated at 163 tons/day today (Djafari Petroudy et al., 2021). Multiple technological gaps limit the transfer of knowledge and technology from the lab to the industry. For instance, one can witness the extensive, broad range of CNF grades that are available/referred to in the literature (Nechporchuk et al., 2016) - all with distinct, non-readily comparable performance. This variety in CNF grades comes from (i) the numerous production routes (an infinite combination of enzymatic, chemical, or mechanical treatments is possible (Jonoobi et al., 2015)); (ii) biomass variability with respect to chemical composition and structural properties (Mokhena & John, 2020); (iii) the inherent hydrophilicity of CNF films that limits their use as packaging substrates (Ahankari et al., 2021; Tarrés et al., 2018), among others.

1.5. The limitation: The use of CNFs for packaging application and its susceptibility to water and moisture

Although CNF films are ideal candidates for oxygen and grease barriers and have excellent mechanical properties, they present poor resistance to water and humidity. For instance, untreated CNF films can have WVTR over 200 g/m². day and WCA ~ 40° (Pasquier et al., 2022). To address these challenges, especially for applications in food packaging, modifications of CNFs are being extensively explored in the literature, some of which are presented in **Table 1.1**.

The data presented in **Table 1.1** shows a range of modification strategies used in the development of packaging materials to enhance their barrier properties and hydrophobicity. For instance, the wax coating in a multilayer system notably reduced the WVTR to as low as 5 g/m² per day and achieving a WCA of 114°, creating a higher moisture and water barrier (Pasquier et al., 2022).

Table 1.1 Strategies to improve water vapor transmission rates and water contact angles of cellulosic materials

Strategy	WVTR g/m ² . day	WCA (°)	References
Acetylation	167	-	Li et al., 2019
Exfoliation and Acylation	101	120	Deng et al., 2016
Wax coating	40	110	Österberg et al., 2013
Wax coating - Multilayer system	5	114	Pasquier et al., 2022
PLA* -Multilayer system	50	-	Le Gars et al., 2020
PLA/ Paperboard	28	-	Koppolu et al., 2019
Rf** Plasma/ PLA/WPU***	55	89	Yang et al., 2024
Plasma	114	93	Babaei et al., 2023

*PLA: Polylactic acid, **Rf: Radio frequency, ***WPU waterborne polyurethane

Despite these improvements, the moisture barrier of CNF films remains insufficient to compete with that of commercial plastic and meet the requirements for food packaging (Rodionova et al., 2011). Specifically, packaging for products that require high moisture barrier, such as potato chips with WVTR values below 0.3 g/m².day (Butler & Morris, 2009). Furthermore, the chemical modification strategies designed to enhance the moisture barriers of CNFs often rely on the use of toxic chemicals or solvents such as N, N- Dimethylformamide (DMF) (Deng et al., 2016) or high temperatures, above 60 °C and require multiple reaction steps (Li et al., 2019), which can hinder their large-scale and cost-effective implementation. Additionally, certain chemical reactions are known to modify and potentially compromise the inherent properties of cellulose, including its crystallinity and strength (Henriksson et al., 2008; Jonoobi et al., 2010), and its biodegradability (Frank et al., 2018). While these contributions have highlighted the potential of modifications of CNFs to enable high barrier materials; studies on feasibility and processes with the potential to be scaling up are still needed.

To address these challenges, we explored the process-structure-performance relationships of CNFs and CNF films. Prior to any modifications, we aimed to investigate each step of the process—from initial production and processing conditions, through the bulk film's composition influenced by the chemical composition of the biomass, to the surface characteristics and post-treatment of CNFs (**Figure 1.4**). The main goal is to determine how these factors affect water and vapor barrier properties without compromising other properties of CNFs, utilizing the most viable sustainable solutions. This approach can potentially advance the use of CNF films as a single layer for packaging applications.

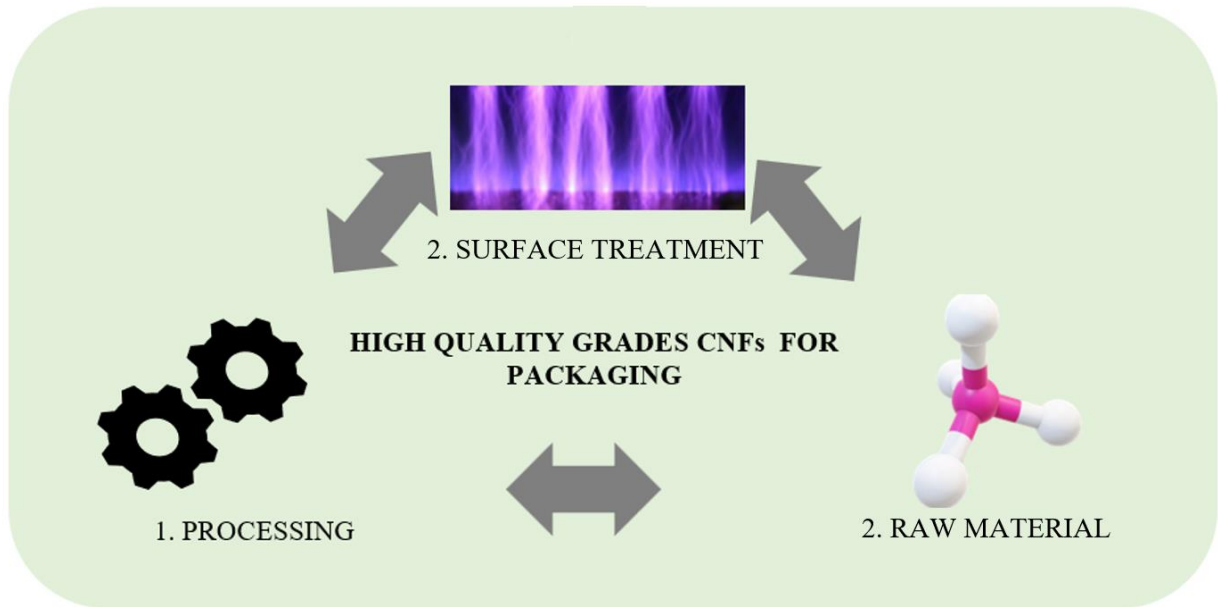


Figure 1.4 Schematic illustration of processing, raw materials, and surface treatment of CNFs.

1.6. Strategy one, the processing: Production routes of cellulose nanofibrils

CNFs can be prepared by different methods; each with its own advantages and limitations. Mechanical disintegration of biomass is the most common and pioneering treatment for CNF production, due to its simple processing operations, broad applicability to most types of biomasses, and ability to produce large quantities of materials (Noremylia et al., 2022a).

The shear forces applied to the pulp, usually dispersed in aqueous medium < 5wt.% (Nechporchuk et al., 2016), defibrillate the macro-scale cellulosic fibers and release their microfibrils and nano (or elementary) fibrils. Several mechanical extraction methods exist and can be done using e.g., a high-pressure homogenizer (HPH) (Li et al., 2012) or a microfluidizer (Wang et al., 2015). In the HPH (**Figure 1.5**) the pulp goes through a narrow space and the

homogenizing valve and an impact a ring at high pressure, creating intense shear and forces that break down the fibers into micro and nano fibrils. In contrast, a microfluidizer uses high pressure to push the material through microchannels, with specific geometries (Z or Y shape) where repetitive impact and shear forces to disrupt the fibers into finer fibrils (Nechporchuk et al., 2016).

The use of a grinder is another often used equipment that resembles the disk refiner used in the pulp and paper industry. In this process, a rotator disc applies cyclic shearing stress to the fiber slurry. Additionally, the fibers are affected by the compression forces between the static and rotator discs, as well as rolling friction. The resulting fibers may suffer from degradation and uneven distribution in width (Siró & Plackett, 2010).

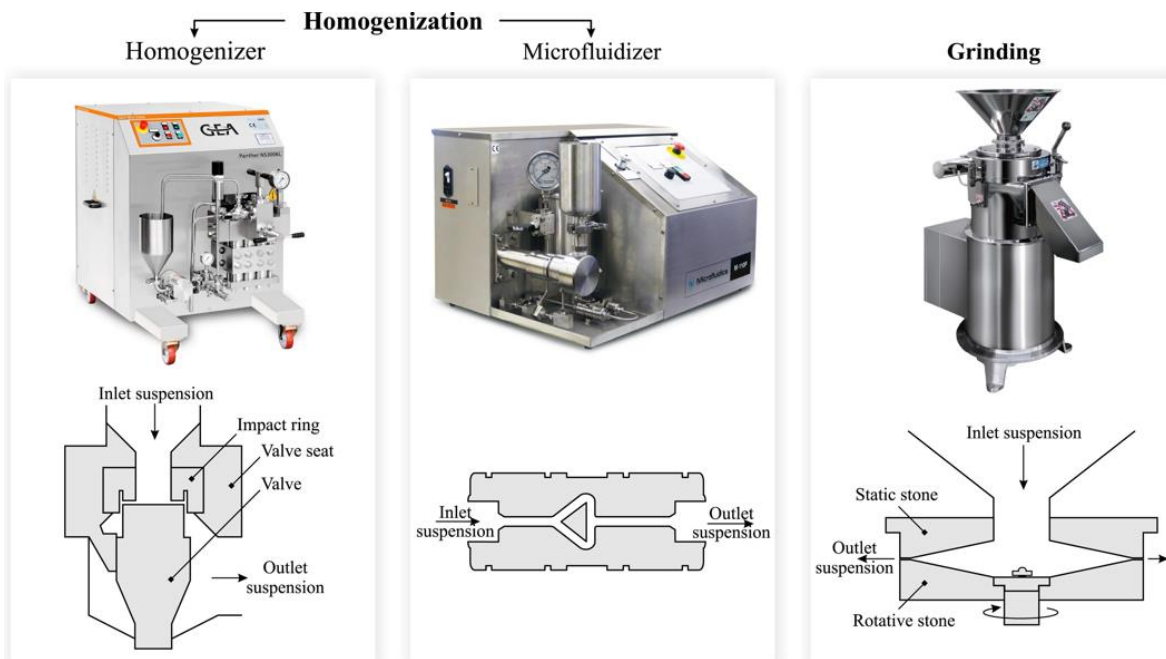


Figure 1.5 Conventional defibrillation methods of CNF: High-Pressure Homogenization, Microfluidization, and Grinding. (Reproduced from Nechporchuk et al. 2016, Copyright © 2016, Elsevier Ltd.)

The aqueous counter collision (ACC) is another, more recent method of preparing CNFs that has not been well explored in the literature yet. The research group of Professor Tetsuo Kondo in Japan is one of the pioneers and inventor of this technology (Ishikawa & Kondo, 2021; Kondo, 2022; Kondo et al., 2014; Kondo et al., 2008). There are different types of ACC geometry, one relies on the impingement of two high-speed jets of aqueous suspension inside a closed chamber. The raw material is expelled through a pair of opposing nozzles and collides against each other at a high pressure between 70-250 MPa (Kondo, Morita, Hayakawa, et al., 2008). Another chamber geometry of ACC is the ball-type chamber. In the ACC-ball type, suspensions of cellulose fibers are ejected at high pressure through a micrometer-wide nozzle and sent into the chamber for collision against a ceramic ball. The fibers are pulverized and defibrillated from the micro- to the nanoscale (**Figure 1.6**). The advantage of this chamber is the direct collision with the ceramic ball. Since most of the slurry will be in contact with the ball, defibrillation is expected to occur more effectively. Moreover, the chamber consists of inert technical ceramic and stainless steel, thus contamination of the slurry from particles of the system is minimal. Despite the potential of the ACC to individualize cellulosic fibers, the use of ACC ball-chamber type remains unexplored in the literature.

The CNF production process combines various operations. Adjusting process conditions and pretreatments yields different CNF grades. Refining, grinding, and homogenization are the main mechanical techniques for CNF production at scale. Although diverse equipment treatments produce varying CNF quality grades, the absence of standardized methods complicates the comparison and distinction of these grades (Pennells et al., 2022). Notably, companies such as Borregaard (Norway), Suzano and Klabin (Brazil), University of Maine (USA), and Nippon Paper and Oji Paper (Japan) produce a wide array of CNF grades

commercially. However, optimal processing conditions for specific CNF applications have not yet been established (Nechyporchuk et al., 2016).

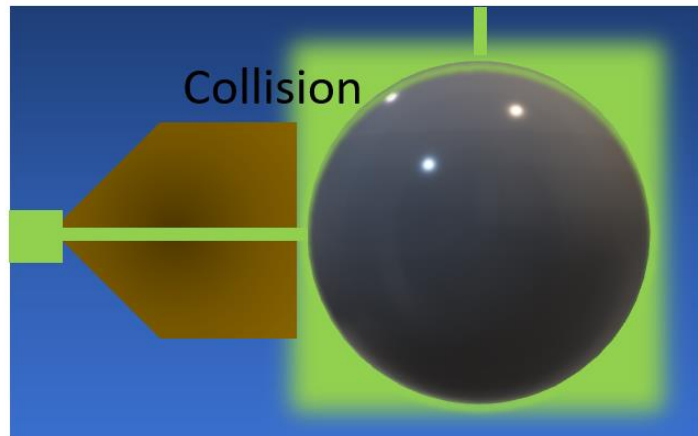


Figure 1.6 ACC ball-type chamber, in green color symbolizing the CNF suspension being injected into the chamber.

Previous studies indicate that CNFs perform optimally when they achieve a high degree of defibrillation or individualization. It is generally assumed that effective defibrillation requires substantial energy consumption, especially during high-shear treatment aimed at maximizing defibrillation (Karande et al., 2013). However, enhancing CNF defibrillation by increasing the pressure or number of passes during defibrillation significantly increases energy consumption (V. Kumar et al., 2014) and limits commercialization of CNFs due to costs increase (Djafari Petroudy et al., 2021). This energy demand can vary from below 500 to over 50000 KWh/ton depending on the treatment used (Ang et al., 2019a). To reduce the energy consumption, many studies involve the use of chemicals (Malucelli et al., 2019a) or enzymes (X. Liu et al., 2018) to process biomass in a more cost-effective way. However, the use of chemicals may modify the surface chemistry of cellulose and introduce potential toxicity to the CNFs (Osong et al., 2016), while the use of enzymes requires special treatment conditions and may have undesired environmental impacts (Vigneshwaran et al., 2015).

Hence, this research focuses solely on the use of mechanical treatments to produce CNFs, a method that presents challenges such as high energy requirements and the difficulty of achieving uniform CNF properties. We aim to understand how processing conditions impact CNF performance, aiming to minimize energy consumption and enhance the quality of CNFs for packaging applications. Achieving this understanding is crucial for the commercialization of CNFs at reduced costs. The approach proposed in this work can be adapted to other mechanical treatments to produce high-performance tailored CNF grades with optimized processing conditions.

1.7. Strategy two, the surface: post-treatment

Plasma, also referred to as the fourth state of matter, is an ionized gas consisting of charged species, excited atoms and molecules, and high-energy photons (Sasai et al., 2011). Differently from hot plasmas, which operate at temperatures above 10,000 K (Mendonça & Terças, 2013), cold plasma uses low temperatures, typically below 313 K and can be used at atmospheric pressure (Laroussi, 2020). Cold plasmas are generated through electrical discharge, which involves the ionization of a neutral gas using a strong electric field and are ideal for treating materials that are sensitive to degradation at high temperatures, such as CNFs (Lichtenstein & Lavoine, 2017). Corona treatment, for instance, is a type of cold plasma commonly used in the packaging industry to improve the printability and wettability of the surface, and in turn, the adhesion between layers of different compositions (Tendero et al., 2006). It is worth mentioning that the range of chemical surface modification enabled by corona treatment remains limited, as this treatment depends on atmospheric air ionization only (Laroussi, 2020).

Dielectric Barrier Discharge (DBD) plasma is created by electrical discharge between two electrodes, separated by an insulating (dielectric) material (He et al., 2022) (**Figure 1-7**). It can be used with different types of gases, such as helium (Profili et al., 2020) and nitrogen (Maechler et al., 2011), or precursors for thin layer's deposition (Asadollahi et al., 2019). Thus, DBD plasmas can be an ideal tool to tailor surfaces. Furthermore, the advanced DBD plasma technology can be easily integrated with other roll-to-roll coating steps, unlike other plasma technologies such as low atmospheric plasma. This facilitates the high-volume processing of advanced functional coatings for applications in the field of packaging (Cvelbar et al., 2019).

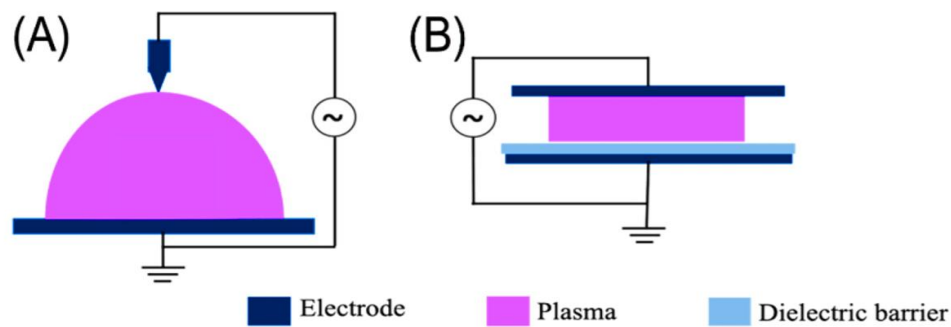


Figure 1.7. (A) Corona plasma (B) DBD plasma – Adapted from Laroussi (2020)

Atmospheric cold plasma has been used for treatment of cellulose derivatives for years, enabling the enhancement of water barrier properties (Profili et al., 2023), and moisture barrier (Khakalo et al., 2020a). This strategy has also been applied to CNFs. Although significant improvements after plasma treatment, the high moisture barrier properties for food packaging, was not yet achieved (Babaei et al., 2023; Khakalo et al., 2020a). Therefore, a systematic study is required to understand the plasma-induced deposition mechanism on CNF films.

In this work, the use of plasma deposition for functionalizing the surface of materials is used as a solution to endow the substrates with advanced barrier performance. Plasma treatment can modify the surface properties of substrates without compromising their bulk performance (Martinu et al., 1999). Moreover, functionalization by plasma does not necessarily require the use of toxic chemicals, solvents, or water (Fazeli et al., 2019). Given these advantages, this work explores the use of plasma as a surface modification strategy. The ability to tune surface wettability in a sustainable way and the potential for large-scale application highlight its practical benefits (Profili et al., 2020).

1.8. Strategy three, the bulk: Influence of biomass chemical composition on the production and properties of CNFs

Besides the effects of processing conditions and equipment type on CNF properties, literature also highlights the significance of the biomass type, pulping process, and the chemical composition of the pulps (Solala et al., 2020). Before producing the CNFs, the biomass undergoes multiple treatments (Nechyporchuk et al., 2016). Initially, the biomass is subjected to chemical or mechanical pulping, followed by a mechanical pretreatment to disintegrate the fibers. Subsequently, the material is processed through high shear treatment, as illustrated in **Figure 1.8**.

The main goal of chemical pulping is to separate the fibers from the lignin that binds them together and/or to facilitate the dispersion of these fibers in water (Davidsdottir, 2013). Kraft pulping is one of the most used processes in industry, it focuses on the efficient separation of fibers through chemical treatments with sodium hydroxide and sodium sulfite at high

temperatures (Solala et al., 2020). The resulting pulp chemistry is very different from the native biomass, this factors not only influence the performance of the resulting CNFs but also affect the processing conditions (Albornoz-Palma et al., 2023b; Ferrer et al., 2012; Rojo et al., 2015).

CNFs can be also produced from unbleached cellulose from Kraft pulps with different lignin contents. The presence of lignin in this type of pulp can expand the CNFs potential for diverse applications because it can promote the interaction with other components (Kumar et al., 2023), can bring antibacterial activity, and UV resistance (X. Zhang et al., 2023). Furthermore, the use of unbleached pulp is a promising material for packaging applications, because of the avoidance of bleaching agents, which could result in less consumption of chemicals and a more sustainable approach.

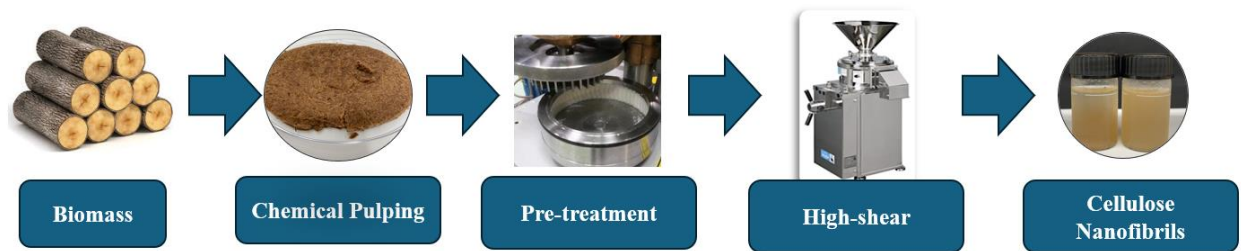


Figure 1.8 The multiple treatment steps from biomass to CNFs.

Hemicelluloses are important components of biomass, they are amorphous heteropolysaccharides of lower molecular weight than cellulose and often contain side chains. Hemicelluloses can function as a binder between cellulose and lignin (Solala et al., 2020). In hardwood, such as aspen, oak, and maple, the dominant hemicelluloses are glucuronoxylan and glucomannan; they usually represent around 15–30% and 2–5%, respectively, of the pulp composition (Pu et al., 2008; Trache et al., 2020). The role of hemicelluloses in CNF production and properties has been intensively investigated in the literature, and it is well-

established that hemicelluloses are beneficial for facilitating the biomass defibrillation and enhancing the mechanical properties of fiber-based materials. Two main reasons have been proposed: (i) Hemicelluloses are hydrogen bonded to cellulose; thus, they can act as a physical barrier between cellulose microfibrils, preventing microfibrils aggregation. (ii) The carboxylic groups from the glucuronic acid in hemicelluloses provide electrostatic repulsions between the fibers, preventing their aggregation (Chaker et al., 2013).

Lignin is a complex biomolecule that is responsible for the strength and rigidity of trees (Jiang et al., 2020). It is composed of polyphenolic phenylpropane units, which comprise three different monolignols: p-coumaryl alcohol, coniferyl alcohol, and sinapyl alcohol. These monolignols combine through oxidative coupling to form a highly branched, three-dimensional polymer. In native lignin, Syringil (S) and Guaiacyl (G) units are connected by ether and carbon-carbon bonds. However, during the pulping process, the native lignin undergoes an oxidative process that significantly alters its chemical structure (Cheremisinoff & Rosenfeld, 2010). The lignin in the pulp after oxidation is called residual lignin.

Recent studies have demonstrated that residual lignin plays a contradictory role in defibrillation. Lignin can inhibit defibrillation by tightly binding with carbohydrates and maintaining the rigid structure of lignocellulose, which complicates the individualization of CNF thus requiring prolonged processing times (Rojo et al., 2015; Solala et al., 2012). Conversely, the appropriate choice of lignin can enhance the fibrillation process by reducing energy consumption, improving CNF yield, and helping produce thinner, more uniform fibrils (Albornoz-Palma et al., 2023c).

The influence of lignin on the barrier properties of LCNF films has also been a subject of investigation. Spence et al. (2011) showed that an increase in lignin content in CNF films

led to worsening their moisture barrier, despite an increase in water repellency. This is a result of partial hydrophobization by lignin that appears to disrupt the film structure, resulting in a bulkier and more porous film. Conversely, it has been reported that the amount of lignin does not linearly correlate with the effectiveness of the moisture barrier. Factors contributing to lower WVTR include increased density of films (Rojo et al., 2015) and enhanced interactions between lignin and cellulose, which decrease water vapor permeation (Bian et al., 2018; Wang et al., 2019)

Multiple studies have highlighted the contradictory role of lignin in various contexts and with different contents; however, the influence of the chemistry of lignin in unbleached pulp and defibrillation process remains unexplored. Understanding how different lignin chemistries interact with CNFs during processing and how these interactions affect film performance appears to be an essential step for accelerating the use of CNFs in packaging materials.

1.9. Research Objectives

In this work, we focus on the development of high-quality grades of CNFs for packaging applications by studying the processing-structure properties of each stage of CNFs production. We hypothesize that to achieve high-quality grades and advance the use of CNFs as a packaging substrate, prior to any modification of CNFs it is required to further understand their process conditions, the bulk structure, and surface of CNFs and CNF films.

Objective 1: Decipher the relationships between processing conditions and properties of CNFs towards the identification of a high-quality grade for packaging application (Chapter 2).

Hypotheses:

- The structure and properties of CNFs are a function of the processing conditions. Different quality grades of CNFs can be produced for specific end-use applications.
- It is possible to optimize the mechanical CNFs production route for a target application. A low water vapor permeability and high mechanical performance can simultaneously be achieved through optimized processing conditions of biomass to produce a CNF grade for packaging application.

Objective 2: Enhance the water and moisture barrier of CNFs films by chemical surface modification using cold atmospheric pressure plasma (Chapter 3).

Hypotheses:

- The moisture barrier properties of CNFs films can be lowered by surface chemical modification only without impacting the mechanical properties of the films.
- It is possible to tune surface chemistry of CNFs films by plasma and tailor their surface properties by changing plasma gas composition.

Objective 3: Evaluate how variations in biomass chemical composition impact the processing, structure, and performance of LCNFs films (Chapter 4).

Hypotheses:

- Proper selection and tuning of biomass chemical composition can advance the production of LCNFs films with desired properties for packaging application, i.e., high mechanical and barrier performance.
- Variations in the chemical composition of biomass are the main driving force for the effective defibrillation of lignocellulosic fibers and the production of LCNFs with tailored properties.

CHAPTER 2: Tailoring Cellulose Nanofibrils Films for Improved Performance through Optimization of Aqueous Counter Collision Processing Conditions

2.1. Abstract

Cellulose nanofibrils (CNF) are typically extracted from lignocellulosic biomass by high-shear mechanical treatment and are increasingly being addressed for use in diverse applications such as packaging. Challenges remain in their successful commercialization and market integration, and this is due to the variability in process conditions and classification of the different quality grades of CNFs for upscale applications. In this work, we processed CNFs via aqueous counter collision and designed the optimal processing conditions via the design of experiment. We evaluated CNF batches pre-treated with two different energy consumptions and relate their film's performance for tensile index (TI) and water vapor permeability (WVP) with their respective structures. Interestingly, the optimal processing conditions for mechanical and water barrier performance of CNFs were found to be in different extremes, and the WVP is driven by surface phenomena. The CNF processed at a high number of passes and pressure damaged the nanofibrils and decreased tensile index values. Meanwhile, the well-compacted structure and O-H availability led to lower values of WVP. The desirable mechanical and barrier responses were merged to find optimal processing conditions. The highest values for tensile index, and lowest water vapor barrier were at 3 passes, 220 MPa, and a suspension concentration of 0.1 wt.%. The quadratic model for optimization gave predicted tensile index values of 68 Nm/g and water vapor barrier permeability of $0.10 \times 10^{-10} \text{ g/m}^2 \cdot \text{s.Pa}$.

Keywords: cellulose nanofibrils, aqueous counter collision, design of experiments, water vapor permeability, tensile strength, packaging

2.2. Introduction

Cellulose nanofibrils (CNFs) are nanosized cellulosic materials that were first introduced by Turbak et al. (Turbak et al., 1983) and Herrick et al. (Herrick et al., 1984) in the 1980s. Wood-based CNFs are typically composed of elementary fibrils of 3-4 nm in width (M. Chen et al., 2021) and their aggregates (widths <100 nm). Their width therefore ranges from 3 to 100 nm, and their length often exceeds one (1) micrometer. CNFs are thus commonly defined as cellulose nanomaterials with an aspect ratio greater than 10 (PD ISO / TS 21346: 2021).

CNFs can be extracted from lignocellulosic biomass by high-shear mechanical treatment (Nechyporchuk et al., 2016). This later is often preceded by either another mechanical pretreatment of lesser intensity, a chemical (W. Chen et al., 2011; Malucelli et al., 2019b) or an enzymatic (Rossi et al., 2021) modification that primarily aims to facilitate the fibrillation of macroscale fibers, ultimately reducing the overall mechanical energy consumption involved into CNF production (Nechyporchuk et al., 2016). Chemical pretreatments can also be used to alter the surface chemistry of cellulose for *e.g.*, further functionalization (Sehaqui et al., 2017).

There are yet benefits in producing CNFs through solely a mechanical pathway. For instance, the costs of CNF production may be minimized compared to the cost of a combined chemical/enzymatic and mechanical route. The level of expertise required for CNF production may be lesser than the expertise needed to conduct a chemical or an enzymatic pretreatment step. The surface chemistry of CNFs remains unaltered after mechanical shearing, and such a route additionally offers the possibility of keeping intact the chemical composition of the biomass (*e.g.*, cellulose, hemicelluloses, and lignin content) used for CNF production. Finally,

the large-scale production of CNFs may be facilitated and can benefit from existing pulp processing equipment (Kandhola et al., 2022).

Mechanically produced CNFs are now globally available at commercial scales (Mokhena & John, 2020) to meet the increasing demands for this material (a CAGR of 22.7% has been forecast for 2022-2028) (Future Markets Inc., 2018, Markets and Markets, 2022). Opportunities in CNF end-products and applications are indeed multiple as shown by their exploitation in a diverse range of applications, spanning from biomedical (Panchal et al., 2019), electronics (Jung et al., 2015), building insulation (Zhao et al., 2021), to art restoration (Baglioni et al., 2021), paintings and coatings (Camargos et al., 2022) and packaging (Ahankari et al., 2021). This latter application is a rapidly growing field because CNFs have shown great potential to replace petroleum-derived plastics. Films made of CNFs can exhibit excellent mechanical (Meng & Wang, 2019) and barrier properties, especially against gas (air and oxygen (J. Wang et al., 2018)), oil and grease (Tayeb et al., 2020), which can make these colloids a promising sustainable alternative to petroleum-derived packaging (Schaidler et al., 2017).

Despite the increasing research and development interest in CNFs and CNF-based products, challenges remain for their successful commercialization and market integration (Moon et al., 2017; Pennells et al., 2022). Among them, one can list the high energy demand of the high-shear mechanical production route (Nadeem et al., 2022) and the low resistance of CNFs to moisture and water (J. Wang et al., 2018). Because of the diversity and variety in CNF production routes and the absence of user's guidelines and standards, end-users are unable to diligently select and chose the grade that will meet their specifications.

Through different strategies, several studies have directed their efforts into addressing this challenge. Some have focused on understanding the relationships between biomass structure, chemistry, and CNF properties (Amini et al., 2020; Hu et al., 2015; Jonasson et al., 2021; Pennells et al., 2022; Trovagunta et al., 2021; J. Wang et al., 2018). Others have investigated CNF production routes to not only lower the overall production costs, but also maximize the performance of the end-products (Håkansson, 2021; Kim et al., 2021; Kriechbaum et al., 2018). We can also report studies that discussed and compared the environmental impacts of different CNF production routes (Arvidsson et al., 2015)— an important factor for the implementation and end-use application of CNFs. Finally, a few review papers have provided comprehensive overviews on where the research community stands on its fundamental understanding of the structure-properties-processing relationships of CNFs (Djafari Petroudy et al., 2021; Isogai, 2020; Q. Meng & Wang, 2019a; Mokhena et al., 2021b; Nagarajan et al., 2021).

Herein, we propose an additional, yet novel contribution to the field that aims to expand our understanding of the processing-properties relationships of CNF materials produced by aqueous counter collision (ACC). With the aim of producing an aqueous suspension that can serve of foundation in the development of sustainable barrier packaging, we looked at optimizing the mechanical production route of CNFs for maximizing the mechanical performance of resulting films while minimizing their water vapor transmission rate. We hypothesized that like wood pulps, different grades of CNFs can be produced for specific end-use applications. In this study, we combined design of experiments and surface response methodology to identify, optimize and ultimately predict the set of processing parameters that

will result in high-performance CNF films (*i.e.*, films of high tensile strength and low water vapor permeance— two properties optimization required for food packaging application).

2.3. Materials and Method

2.3.1. Materials

Never-dried bleached softwood Kraft pulp (NBSK) was provided by WestRock (Covington, VA, USA). The pulp was washed with deionized water to remove impurities. The solids content of the pulp after washing was 30 wt%. The cellulose, hemicellulose and lignin content of the pulp was determined according to the NREL TP-510-42618 (). Calcium Chloride Anhydrous (CaCl_2) was purchased from Sigma-Aldrich (USA) and used for water vapor permeability testing.

2.3.2. Methods

Production of Cellulose Nanofibrils (CNFs)

The NBSK pulp was prepared at a consistency of 10 wt% and refined at 5000 revolutions using a PFI mill refiner (The Norwegian pulp and paper institute, Norway) according to the TAPPI 248 method (TAPPI T248 sp-00 2008). The refined pulp was then set at 1.7 wt% and further processed through a Masuko supermasscolloider grinder (MKCA6-5J®, Sangyo, Japan), used herein as a mechanical pretreatment. The rotation speed set at 1200 rpm was kept constant, while the gap clearance was varied between 50 and 200 μm (Trovagunta et al., 2021) to produce two batches of CMFs at two distinct energy consumptions, namely 0.81 kWh/kg (herein referred to as low energy, EC_{low} -CMFs) and 3.61 kWh/kg (high energy EC_{high} -CMFs).

The CMF suspensions were finally subjected to a high-shear treatment, namely an aqueous counter collision (ACC, Starburst, Sugino Machine Co., Ltd, Japan) equipped with a ceramic ball, to produce aqueous suspensions of CNFs. The number of passes through the ACC, the jet pressure, and the concentration of the CMF suspensions were varied to maximize the CNF quality and film performance. A series of parameters were defined using a design of experiments, as described below.

Design of Experiment

A three-factor Box-Behnken Design (BBD) with three center runs (0, 0, 0) was generated with JMP Pro 16 statistical analysis software (SAS Institute, USA). The concentration of the CMF suspension (input) (wt%), the jet pressure of the ACC (MPa) and the number of passes through the ACC were selected as the three processing variables. The levels for each factor (-1, 0, +1) are listed in **Table 2.1**. The design matrix is shown in **Table 2.2**. Two measured responses (output variables) were selected to evaluate the fibrillation and quality of the produced CNFs, namely the tensile index (response 1) and the water vapor transmission rate (response 2) of films made of the ACC-produced CNFs.

Table 2.1 Factors and design levels for the BBD

Factors	Design Levels		
	-1	0	+1
Number of Passes	1	6	11
Jet Pressure (MPa)	120	170	220
CMF Concentration (wt%)	0.1	0.33	0.55

Table 2.2 Experimental design matrix for the BBD with the factors and respective design levels

Run Number	Number of Passes	Jet Pressure (MPa)	Concentration of CMF suspension (wt%)
1	6	120	0.1
2	1	170	0.1
3	11	170	0.1
4	6	220	0.1
5	1	120	0.33
6	11	120	0.33
7	6	170	0.33
8	6	170	0.33
9	6	170	0.33
10	1	220	0.33
11	11	220	0.33
12	6	120	0.55
13	1	170	0.55
14	11	170	0.55
15	6	220	0.55

Characterization of CNF suspension

Transmittance of CNF suspension: Homogenized CNF suspensions at 0.01 wt% were analyzed using a UV-vis spectrometer (Thermoscientific Inc., Genesys 50, US). Their transmittance value (%) at 500 nm was recorded. An average of three measurements is herein reported for discussion.

Structure, morphology, and dimensions of CNFs: Transmission Electron Microscopy studies of the CNF suspensions were performed using a JEOL JEM 1200EX II microscope with an accelerating voltage of 80 kV. The aqueous suspensions were diluted to 0.0025 wt% and dispersed using an ultrasound bath for 5 minutes. A drop of the dispersion was applied on a carbon -coated copper (Cu) grid and let dry overnight at room temperature (25 °C). The grids were then immersed in a staining solution of acetate of uranyl at 2wt% and the excess was removed prior to TEM analysis. The applied magnification was 200,000×.

Preparation of CNF films

CNF films were made by water evaporation of 0.1 wt% CNF suspensions poured in polystyrene Petri dishes of 8.5 cm in diameter. An average basis weight of ca. 10 g/m² was targeted for each film. The suspension evaporated at room temperature for approximately 4 days. Prior to characterization and testing, the films were kept at 23 °C and 50% relative humidity (RH) for at least 72 h.

Testing of CNF films

Structure of the films: Imaging of the cross-section of the films was performed using a Field Emission Scanning Electron Microscope (Verios 460 25 L, OR, US). The films were cut with a sharp razor blade and coated with a thin layer of gold (ca. 7 nm) prior to image analysis.

Tensile characterization of CNF films: The films were cut into strips 60 mm long and 15 mm wide using a razor blade and clamped to a Universal Testing machine equipped with a 0.5 kN load cell (Instron, USA) to let a 40 mm gap available for tensile strength testing. The experiments were conducted at 23 °C and 50 % RH at a constant rate of 2 mm/min. tensile index values were calculated with the maximum load before rupture and normalized by their respective grammages. Triplicates or more were performed for each treatment. An ANOVA analysis was conducted at a confidence level of 0.05 to report statistically different values.

Density: The average thickness of the CNF films was measured using a L&W micrometer 51 according to Tappi 411. The length and width were measured with a digital caliper to calculate the area.

Water vapor barrier of CNF films: The water vapor permeability (WVP) and water vapor transmission rate (WVTR) of the CNF films were measured at 23 °C and 50 % RH

according to the ASTM E96 standard. Sealed aluminum cups (Model 68-3000 EZ-Cup, Vapometer, USA) were filled with 5g of anhydrous CaCl₂ desiccant. CNF films of 8 cm in diameter were clamped between the cup base (filled with the desiccant) and its lid, so that the edges of the films were tightly sealed. A film area of 0.003318 m² was kept accessible for water vapor diffusion. The films were kept at controlled temperature and humidity for 8 hours. The gain in mass of the films was measured every hour using a lab-scale balance of +/- 0.001 g in precision. The experiments were conducted in duplicate.

The WVTR was measured from the slope of the curve of the gain in mass (g) as a function of time (s) (Jannatyha et al., 2020), and calculated as follows (Equation 2):

$$WVTR \left(\frac{g}{m^2s} \right) = \frac{Mass\ gain\ (g/s)}{Surface\ Area\ of\ the\ film\ (m^2)}$$

Water vapor permeability (WVP) was calculated by multiplying the WVTR value by the thickness of the film, in μm, and dividing by the saturated pressure of water vapor (in Pa) at 50%RH (Equation 3).

$$WVP \left(\frac{g}{Pa * s * m} \right) = \frac{Thickness * WVTR}{Saturated\ Pressure}$$

Surface accessibility of cellulose fibrils studied by hydrogen-deuterium exchange:

Samples were stored at controlled humidity and temperature (23 °C and 50 % RH) for three days. Afterward, 0.05 grams of D₂O were added to the CNF films, and the samples remained with D₂O for absorption additional two days. ATR-FTIR analysis was conducted after two and seven days using a Perkin Elmer Lambda XLS ATR instrument (USA). All the spectra were obtained by 32 scans at a 4 cm⁻¹ resolution and normalized at 1030 cm⁻¹.

2.4. Results and Discussion

2.4.1. Design of Experiments

The aqueous counter collision (ACC) can process pre-treated suspensions of fibers through a micrometer-wide nozzle, at high pressure and velocity. In the production of nanofibrils, the number of pulverizing passes and the collision pressure are critical factors that determine the quality and properties of the resulting material. The number of passes refers to the time it takes for all the suspension to pass through the machine, while the collision pressure has a significant impact on the final product (Kondo et al., 2014). Previous studies have investigated the use of the ACC using biomass sources from 0.2 to 0.5 wt%, collision pressures that vary from 100 to 200MPa and passes from 5 to 50 (Tsalagkas et al., 2020; Utsunomiya et al., 2022; Van Hai et al., 2018; Zhai et al., 2018). These studies were aimed to analyze different mechanical pre and post treatments of CNFs to evaluate CNF performances based on the improvement of mechanical performance, fibrils morphology, size, and crystallinity of CNFs (Tsalagkas et al., 2020; Van Hai et al., 2018; Zhai et al., 2018)

In this study, we kept the nozzle diameter constant, at 100 μm , and varied the following parameters: the number of passes (1 to 11), the concentration of the pre-treated fiber suspensions (0.1 to 0.55 wt%), and the collision pressure (120 to 220 MPa). In this case the chosen design (BBD) allows all the factors mentioned before to work within the limits of the equipment.

Tensile strength is one of the key mechanical properties that is used to evaluate the performance of CNFs. By comparing the tensile strength of the nanofibrils produced under different defibrillation conditions is possible to assess the efficiency of the defibrillation process and optimize the CNF production (Spence, Venditti, Rojas, Habibi, et al., 2011).

Another important property to be considered for improvement for food packaging applications is the water vapor barrier. CNF films can have their water barrier improved by the addition of filler or hydrophobic coatings (Spence, Venditti, Rojas, Pawlak, et al., 2011), in this work, we aim to optimize the mechanical route for the lower values of water barrier and provide the option for reduction of fillers addition or fewer post-treatments.

2.4.2. Fiber Morphology

Analyzing fibrils morphology is essential in understanding the mechanical properties of CNFs. Structural characteristics such as fiber diameter and degree of fibrillation strongly influence mechanical strength (Karande et al., 2013). In Figure 2.1 TEM images of fibrils processed under different conditions are shown (A) – Mild process at 120 MPa, 1 pass and 0.55 wt%, (B) medium process 170 MPa, 6 passes and 0.33 wt% and (C) harsh process 11 Passes, 120 MPa and 0.55 wt%.

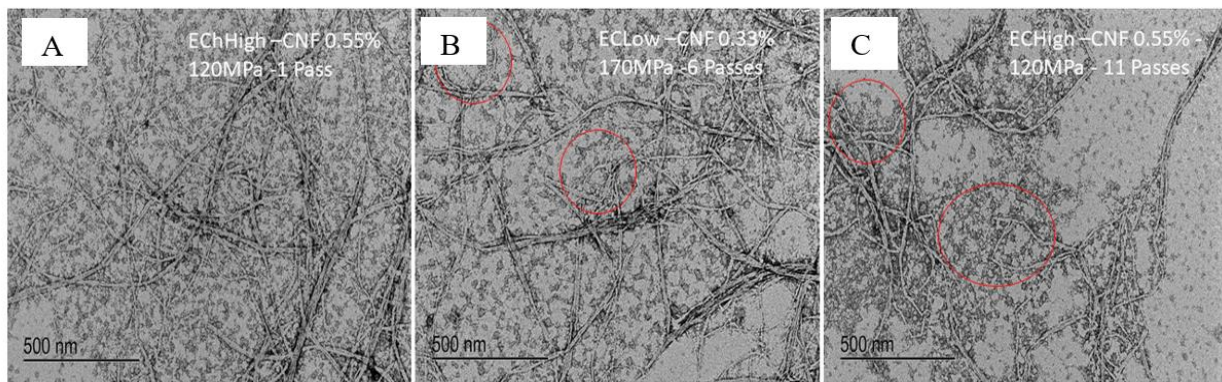


Figure 2.1 TEM of CNF processed under different conditions showing the increased defects when the number of passes is increased from 1 (left) to 6 (middle) and 11(right)

Figure 2.1 B and C illustrated that at a high number of passes fibrils kinks and curls were observed. The collision against the ceramic balls in the ACC is possibly the factor

affecting defibrillation that is causing this damage when processing conditions are harsh. This effect was observed by Spence et al. 2011 during a similar process with microfluidization. The increase in pressure or number of passes in their study dropped the toughness and tensile index values of their composites. Hence, it is expected that the fibrils morphology and appearance of kinks at harsh processing conditions also affect the films' mechanical performance in this work.

2.4.3. Tensile Index of CNF Films

Films made from the grinder-processed fibers (i.e., CMF suspensions obtained at low and high energy consumptions) exhibited an average tensile index (TI) of 31 ± 2 and 66 ± 9 Nm/g for the EC_{Low}-CMF and EC_{High}-CMF, respectively (SI – Table 2). After processing the CMF through the ACC, it is expected an increase in TI due to enhancement in specific bond strength and relative bonded area by increasing the surface area for hydrogen bonding (Page, 1969). Nonetheless, to maximize the network performance it is important to note that the presence of defects such as kinks may adversely affect the increase in tensile strength (Lindström et al., 2016).

After processing cellulose microfibrils (CMF) through the aqueous counter collision (ACC), the resulting tensile index demonstrated a significant increase in the EC_{Low}-CNF, while minimal or no improvement in mechanical performance was observed for the EC_{High}-CNF (Figure 2.2).

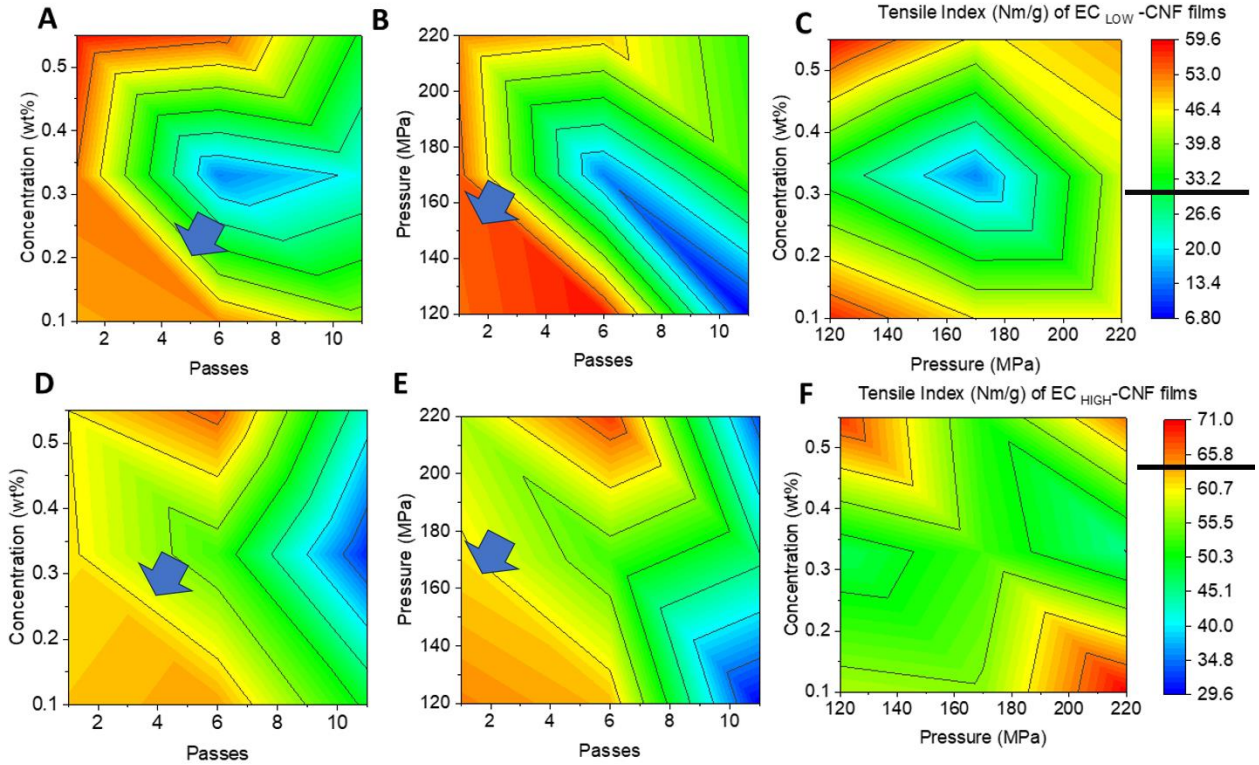


Figure 2.2 Average tensile index of EC_{Low}-CNFs, A: combination of concentration and passes; B: Pressure and passes, C: concentration and pressure. Tensile index of EC_{High}-CNFs, D: concentration and passes, E: Pressure and passes, F: concentration and pressure.

The increase in tensile index observed for the EC_{Low}-CNFs (Figure 2.2 a, b, and c) can be due to the increase in their apparent aspect ratio, which in turn, would be responsible for an improved bonding between the CNFs (Ang et al., 2019). An increase in density from 0.4 g/cm³ up to 0.8 g/cm³ is observed after submitting EC_{Low}-CMF to the ACC. This density increase can be attributed to better network interconnectivity (Kulachenko et al., 2012). Moreover, in terms of processing conditions density increase was mostly influenced by the increase in the number of passes (**Table 2-3**).

Density is an important parameter to evaluate tensile strength, however, other features such as fibril defects as observed in TEM images (**Figure 2.1**) should be considered. This

defects can cause discontinuities in load distribution and drop the tensile index, as observed in previous work (Zeng et al, 2012). In Figures 2-2a and b the highest values of tensile index (58 ± 5 , 50 ± 9 , 53 ± 2 , and $52 \pm \text{Nm/g}$) were found in processing conditions where passes were 1, 3, and 6. This information suggests that values of tensile for CNF are being influenced by parameters other than only network performance (Taylor et al., 2020).

Further processing through the ACC did not result in an overall increase in the tensile index of EC_{High}-CNF films. The films remained with plateaued tensile values in the average of $62 \pm 5 \text{ Nm/g}$ when the number of passes was 1 and 6, while pressure and concentration are not of great influence in the results within this range of passes (**Figure 2.2 d and e**). We assume that the evolution of tensile properties has reached its saturation and further fibrillation does not improve the properties, this is supported by research conducted by Lindström, 2017. Finally, there is a substantial drop of tensile $33 \pm 7 \text{ Nm/g}$ when the number of passes is 11 and the pressure is 220 MPa, this behavior is also evidenced for EC_{Low}-CNF (**Figure 2.2b**).

In this study, it is referred to a high-quality grade CNF to a consistent and homogeneous material with desirable properties, such as high mechanical strength and good moisture barrier performance. Furthermore, the material must be obtained in controlled and optimized process conditions that result in CNF film with few defects.

2.4.4. Water Vapor Permeability (WVP)

CNF films are known to have higher water vapor permeability values than commercially available petroleum-derived films. For instance, this value can be up to 17 times higher compared to polyethylene (PE) (Steven & Hotchkiss, 2002). To meet the food packaging requirements for the WVP barrier, most applications require values low values, for instance, the low-density polyethylene films have WVP values ranging $6.97 \times 10^{-12} \pm 7.74 \times$

$10^{-13}(\text{g}/\text{m}\cdot\text{s}\cdot\text{Pa})$ (Cazón et al., 2022). It is important to acknowledge that simply by adjusting the mechanical process it is not possible to achieve low WVP values that can be competitive with the products already in the market. To meet the requirements for food packaging, it would be necessary to lower the CNF film vapor barrier by about 200- fold (Pasquier et al., 2022). Within the scope of this research, efforts were made to reduce this gap and minimize the use and intensity of chemical post-treatments by solely optimizing the processing conditions of the high-shear mechanical route.

It is expected that the adsorption of moisture phenomenon in CNF films increases with the increase in the surface area and exposure of hydrophilic sites and increases the surface tension. During the diffusion process, the increase in tightness or crystallinity of the films can restrict the path of water molecules lowering the overall water vapor permeability (Wang et al., 2018). However, the impact on the overall process of CNF films is still unclear.

The high-shear treatment of CMFs using the ACC led to an overall reduction by ca. 20% in the WVP values of the CNF films, and this, regardless of the CMF batch (i.e., processed at low or high energy). Moreover, the overall moisture barrier performance was observed in EC_{High}-CNF systems with a substantial decrease in WVP of 39% compared to EC_{low}-CNF. To classify different quality grades of CNFs, and promote fewer post-treatments for hydrophobicity increase, it was investigated the EC_{High}-CNF because it presented the lowest moisture barrier results (**Figure 2.3**).

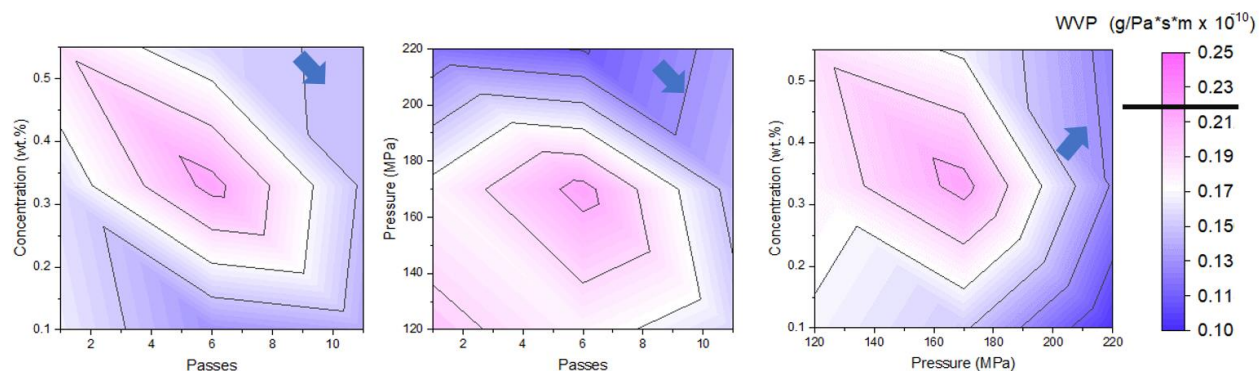


Figure 2.3 Variation in water vapor permeability values of ECHigh-CNF films as a function of the processing conditions, A) concentration x number of passes, B) Jet pressure x number of passes, C) Concentration x Jet pressure.

In **Figure 2.3a** and **b** it is observed a trend where the lowest values for WVP were found at a high number of passes (11 and 6) and pressure of 220 MPa. These values were between $0.10 \pm 0.01 \times 10^{-10}$ (g/m·s·Pa) and $0.15 \pm 0.01 \times 10^{-10}$ (g/m·s·Pa). The harsh processing conditions previously mentioned resulted in the formation of nanofibrils with an increased surface area, and denser film structures owing to the ability of the CNFs to entangle in a tighter network with densities averaging around 1.3 ± 0.2 (g/cm³) for samples processed at 6 and 11 passes (#1,#3,#4,#11,#15) meanwhile for 1 pass (#2, #5, #13) the average density value slightly drops to 1.0 ± 0.1 (g/cm³) as observed in Table 2.4.1.

Table 2.3 WVP, standard deviations, and density of CNF films processed in the ACC.

<i>Sample</i>	<i>WVP (g/Pa*s*m.10⁻¹⁰)</i>	<i>Density (g/cm³)</i>
#1	0.173	1.2 ± 0.3
#2	0.170	0.9 ± 0.1
#3	0.147	1.2 ± 0.1
#4	0.103	1.5 ± 0.2
#5	0.200	1 ± 0.2
#6	0.163	1 ± 0.2
#7	0.203	1 ± 0.2
#8	0.215	1 ± 0.2

Table 2.3 (continued)

#9	0.237	1 ± 0.2
#10	0.127	1.2 ± 0.2
#11	0.144	1.5 ± 0.2
#12	0.190	1.1 ± 0.1
#13	0.191	1.2 ± 0.3
#14	0.153	1.1 ± 0.1
#15	0.132	1.6 ± 0.2

Density increase might be one contributing to slowing the diffusion throughout the film and reducing the WVP (Aulin et al.2009). Notwithstanding, amongst the densely configured samples that evidenced lower WVP values, considerable changes are imminent. Sample #4 (6p, 220MPa, 0.1 wt.%) presented 0.10×10^{-10} , #11 (11p, 220MPa, 0.33wt%): 0.144×10^{-10} , and #15 (6p, 220MPa, 0.55wt%): 0.132×10^{-10} (g/m·s·Pa). This suggests that intra and inter molecular bonds, and O-H availability on the CNFs surface that bond with water vapor (i.e., rate of sorption and desorption) are influencing the results of WVP.

2.4.5. The CNF Surface study via D₂O

The availability of hydrogen bonds in the process of moisture uptake can be evaluated by Fourier Transform Infrared Spectroscopy (FT-IR) in tandem with deuterium exchange D₂O (Solhi et al., 2023). During this process, a broad band near 2500 cm^{-1} appears due to O-D stretching and OH stretching ($3600\text{--}3000 \text{ cm}^{-1}$) reduces, indicating the substitution of

hydrogen with deuterium. **Figure 2.4** reveals the initial infrared spectra of CNF films #04, #11 and #15, and after 48 h and 1 week of exposure to D₂O.

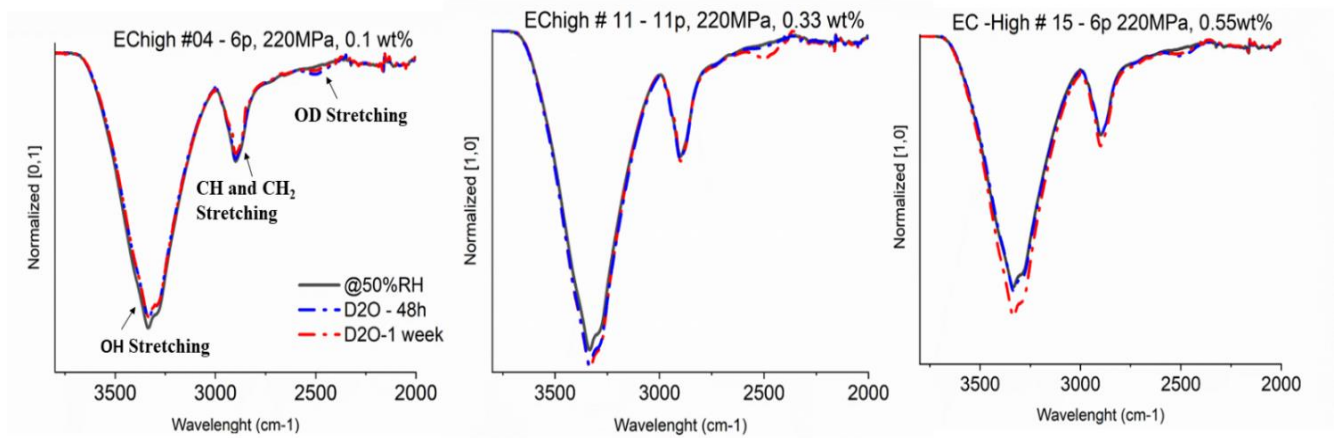


Figure 2.4 FT-IR spectra of CNF films sample #4 (6p, 220MPa, 0.1 wt.%), #11 (11p, 220MPa, 0.33wt%) and #15 (6p, 220MPa) exposed to D₂O for 48h and one week.

In figure 2.4 The CNF film EC-High #4 the exposure to D₂O resulted in a reduction in both the width and height of the O-H band at 3600-3000 cm⁻¹, observed at 48 hours and further at one week. The addition of deuterated water to the film induced a hydrogen-to-deuterium exchange in the moisture-accessible OH groups of Sample EC-High #4 within the first few hours, leaving no absorption sites for moisture from the air available. This suggests that water sorption in the films behaves like surface diffusion phenomena. In this phenomenon, molecules are adsorbed on the surface of the film and then jump to the next adsorption site (Bedane et al., 2016) . This behavior is usually attributed to the extensive surface area and minimal porosity of the film surface (Bedane et al., 2016). This might explain the reduced WVP for EC-High #4 to 0.10×10^{-10} g/m·s·Pa.

In contrast, samples EC-High #11 and EC-High #15 show a slight enlargement of the band between 3600-3000 cm⁻¹, indicating that moisture is being absorbed in the first hours of exposure to deuterium, with the exchange either not occurring (EC-High #15) or occurring

simultaneously with air moisture absorption (EC-High #11). This suggests that O-H availability is still high, and a different diffusion process is happening. This delay in deuterium exchange might indicate that the films' morphology influenced by the rigorous processing conditions are leading to higher WVP (Table 2.3) compared to EC-High #4 and requires further investigation.

Combined optimization of the tensile strength and water vapor permeability performance of CNF films require a balance of the ACC processing conditions. Mild processing conditions were found to be necessary to achieve the highest tensile index (up to 6 passes, pressure in the range of 120-170MPa and 0.55wt%), while harsher processing conditions were needed to reduce WVP from the pretreated films $0.210 \text{ g/Pa.s.m} \times 10^{-10}$ (EC-high-CMF) to approximately $0.130 \text{ g/Pa.s.m} \times 10^{-10}$ (EC-high-CNF). Further investigation of the interplay between the three independent factors (pressure, concentration, and pressure) is necessary to understand the trends and their impacts on the responses and the processing conditions for producing quality grades of CNF for packaging application.

2.4.6. Predictive Model and Optimization

Combined optimization of the tensile strength and water vapor permeability performance of CNF films require a balance of the ACC processing conditions. In this research, it was combined the results obtained from EC-high-CNF. The model generated by secondary least squares fit merges the averages of minimum values of WVP and maximum tensile index (**Figure 2.5**).

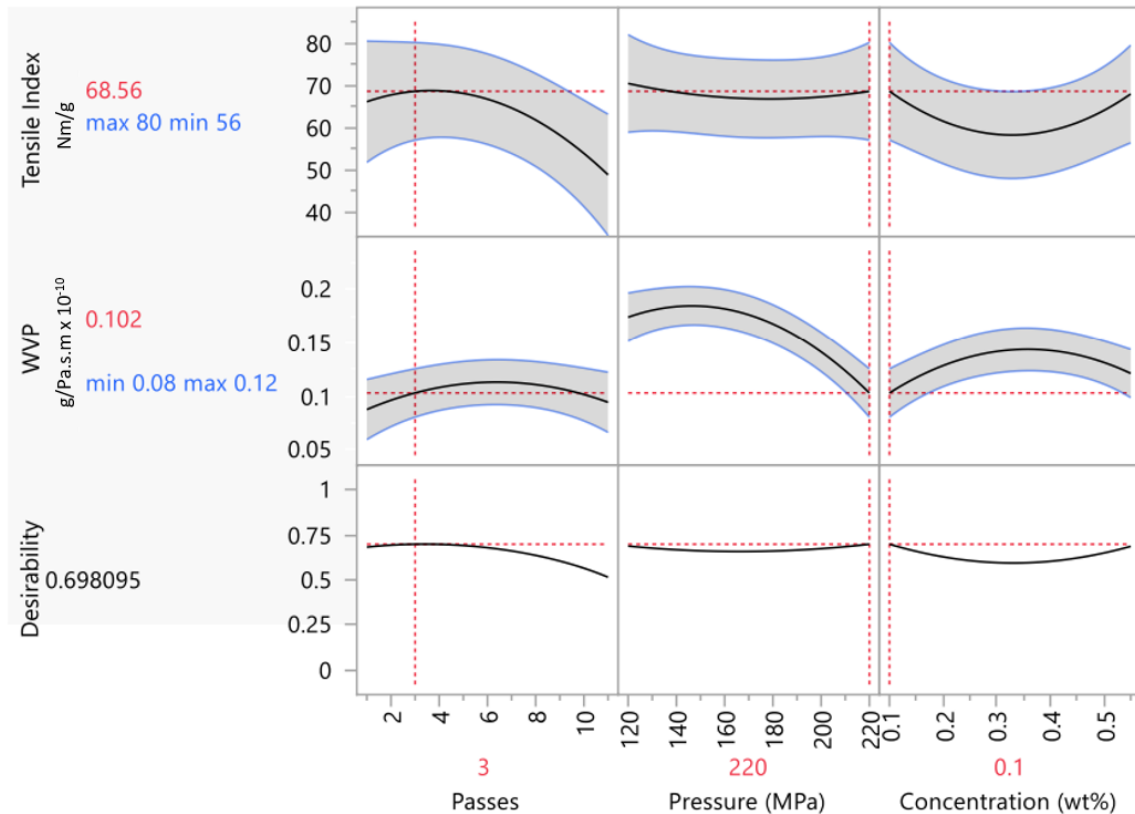


Figure 2.45 Predictive graph and maximum desirability to optimize processing conditions of EC-high-CNF. Red dotted lines mark the points of maximum tensile index and minimum WVP.

To create the predictive model coefficients with p -value < 0.05 were considered while those with p -value > 0.05 were deleted. The tensile index predicted values presented a coefficient of determination R^2 0.86, p -value 0.01 when compared to the experimental data. Meanwhile, predicted values for WVP demonstrated an R^2 of 0.94 and a p -value of 0.001. These results are close to the experimental data and indicate a good prediction of both models (Vera et al., 2023). The high p -values for the lack-of-fit test (tensile index: 0.39 and WVP: 0.85) are larger than the level of significance (0.05). This means that the lack of fit is not significant for both models at the 5% significance level, indicating that the second-degree polynomials have a good fit for the experimental data for the selected EC-high-CNF properties

(Dong et al., 2016). Finally, the optimized conditions with maximized desirability of 69% were found at 3 passes, the jet pressure of 220 MPa, and concentration of 0.1 wt%.

2.4.7. Response Surface Methodology (RSM)

The RSM generated by the model of predicted formulas is illustrated in **Figure 2.6**. The response surface model was implemented to maximize tensile index values and minimize WVP. The response surface for tensile index was plotted in function number of passes and concentration, while the RSM for WVP illustrates influences of pressure and concentration.

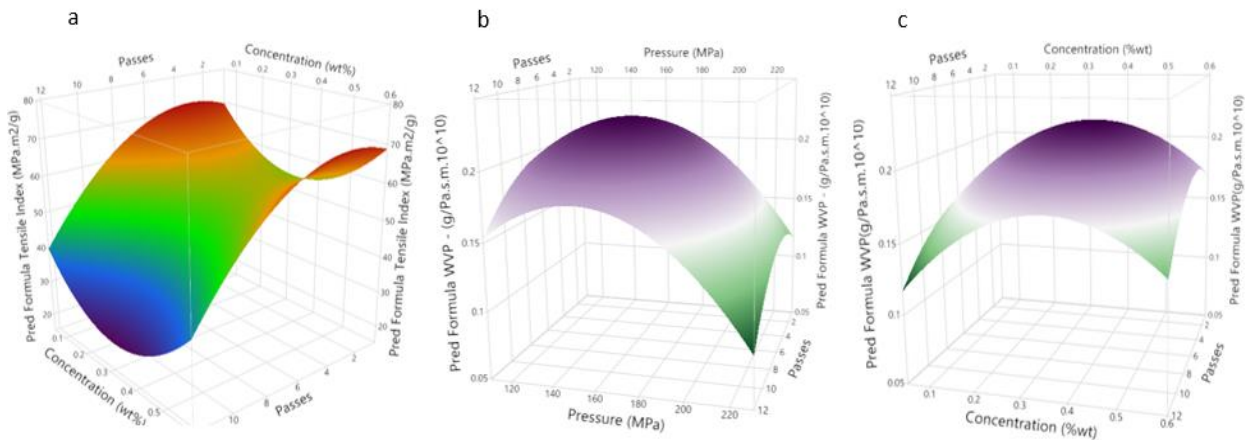


Figure 2.6 a) Predictive response surface of the tensile index - EC-CNF_{High} in the function of concentration wt.% and passes; b) WVP in the function of pressure (MPa) and passes c) and passes and concentration wt.%

The RSM plot indicates the tensile index values are responsive to the number of passes and concentration. As observed in **Fig. 2.6a**, when the number of passes increases the values for tensile index decrease below 30 Nm/g, in accordance with the results obtained experimentally. On the other hand, for the range of concentration between 0.3 and 0.1 wt% or higher than 0.55 wt.% and passes up to 6 the highest values of tensile were observed, these values are predicted to reach values above 60 Nm/g. These trends agree with the experimental

data. Low values of WVP are predicted in pressures above 200 MPa (**Fig. 2.6b**), concentration below 0.2 or over 0.4wt%, and passes over 6 (Figure **2.6c**).

The collected experimental data for this optimization (3 passes – 220MPa and 0.1 wt.%) resulted in values of 67 ± 8 MPa.m²/g and 0.16×10^{-10} MPa.m²/g. Although the WVP value is the lowest within the experimental design. The least squares model did not fit well with the predictive model for the WVP. Since the WVP response is related to different types of phenomena within the collected experimental data as outlined in section 2.4.3, other models that could incorporate more detailed information, such as machine learning would be necessary for a more accurate prediction.

2.5. Conclusions

CNF films can be tailored for specific applications by optimizing processing conditions, resulting in films with varying mechanical strength and vapor barrier properties. The introduction of two initial grades from grinder-processed fibers (CMFs) highlighted performance differences, mainly in mechanical strength and vapor permeability. When these different grades of were subjected to the Aqueous Counter Collision, the CNF films showed that optimal tensile strength is achieved under mild processing conditions, whereas harsh processing conditions were necessary to significantly reduce the water vapor permeability of the films.

Specifically, when evaluating films derived from grinder-processed fibers, different tensile index values were observed; 31 ± 2 Nm/g for EC_{Low}-CMF and 66 ± 9 Nm/g for EC_{High}-CMFs. The ACC processing of cellulose microfibrils (CMF) enhanced to higher tensile index values for EC_{Low}-CNF. Conversely, E-high-CNF demonstrated negligible enhancements in mechanical performance. Optimal tensile strength, notably for both EC_{Low}-CMF and EC_{High}-

CMFs, is achieved under milder processing conditions: up to 6 passes, pressures between 120-170MPa, and 0.55 wt%. Furthermore, ACC's treatment resulted in a reduction of around 20% in the WVP of the CNF films. This outcome was consistent irrespective of the energy profile of the CMF batch. Additionally, a more aggressive processing regime was required to diminish further the WVP from initial values of $0.210 \text{ g/Pa.s.m} \times 10^{-10}$ (EC-high-CMF) to approximately $0.130 \text{ g/Pa.s.m} \times 10^{-10}$ (EC-high-CNF).

The experimental conditions were fitted into a predictive model. The least squares predictive model efficiently fit the experimental data for mechanical strength, however further studies are necessary on the diffusion mechanism for the CNF films.

CHAPTER 3: Tuning the Surface Chemistry and Properties of Cellulose Nanofibril (CNF) Films by Dielectric Barrier Discharge (DBD) Plasma for Packaging Applications

3.1. Abstract

Films made of cellulose nanofibrils (CNFs) have shown promise as sustainable alternatives to petroleum-derived plastic packaging owing to their high barrier against gas and grease, high strength-to-flexibility ratio, tunable transparency, and inherent biodegradability. The hygroscopic nature of cellulose remains a challenge for their direct use as food-packaging films. In this work, we exploit the potential of dielectric barrier discharge (DBD) plasma to tune and tailor the surface physicochemical properties of CNF films with the goal of improving their barrier properties against water and moisture. Two strategies were investigated to modify the surface properties of CNF films: (i) the deposition of organosilicon fragments in static mode using 2,4,6,8-tetramethylcyclotetrasiloxane (TMCTS) as precursor, and (ii) the formation of multilayers of different surface chemistries by tuning the plasma carrier gas and organosilicon fragments' chemistry. Strategy (i) enabled the identification of process parameters for the uniform deposition of hydrophobic TMCTS fragments on the CNF films' surface. Strategy (ii) built on strategy (i) with the creation of a multilayer structure made of tailored hydrophilic, and hydrophobic layers. This structure considerably reduced the water absorption of the films by decreasing the presence of defects, offering an enhanced protection compared to the untreated CNF films. This study shows that by optimizing the plasma gas composition, time, and application mode (*i.e.*, static vs. dynamic mode) for controlled coating of chemical moieties, CNF films with tunable water and vapor barrier properties can be designed to meet the broad range in barrier requirements of food packaging. Hence, plasma

offers a sustainable and scalable approach to tailor the performance of CNF films and advance their application in the packaging industry.

KEYWORDS: cellulose nanofibrils, CNFs, dielectric barrier discharge, plasma, barrier properties, organosilicon coating.

3.2. Introduction

Global and concerted efforts towards the development of sustainable alternatives to petroleum-based plastics have been driven by the increasing demand for low-cost, environmentally safe, and non-toxic packaging materials. Petroleum-derived plastic packaging face end-of-life challenges due to their inherent non-biodegradability and their very low recycling rates. Out of the ~6 million tons of plastic packaging being produced in 2021, 36% were labelled as reusable, recyclable or compostable. Yet, only 13.3% out of these 2.2 million of packaging labelled as “sustainable” ended up being recycled (U.S. Plastic Pact: 2021 Annual report, 2021).

Multilayer packaging such as flexible packaging is the most impacted category by these end-of-life challenges. Multilayer packaging substrates are manufactured through the smart association of different plastic films (*e.g.*, polyethylene (PE)) and non-plastic materials (*e.g.*, aluminum foil) to create unique properties that cannot be achieved by a single material (Fávaro et al., 2013b). For instance, PE is commonly utilized for its moisture and gas barrier capabilities, while aluminum is privileged for its protection against light, ultraviolet radiation, and overall ability to extend the shelf-life of the food product. Other examples can include the

use of low-density polyethylene (LDPE) and linear low-density polyethylene (LLDPE) for their role as sealing agents, binding layers, and structural layers (Bauer et al., 2021).

Although the manufacturing process of multilayer packaging offers immense benefits with respect to weight-to-performance and performance-to-cost ratios, we are not yet equipped to separate these thin layers of materials for the proper recycling of flexible packaging (Bauer et al., 2021). One solution to address this challenge lies in the replacement of the non-recyclable/non-biodegradable layers with sustainable alternatives, without compromising the overall package's functionality.

Cellulose nanofibrils (CNFs) represent a unique solution for multilayer packaging design and manufacturing (Pasquier et al., 2022b). Films made of CNFs have shown promise as sustainable packaging because they come from renewable resources, exhibit excellent mechanical properties (Q. Meng & Wang, 2019b), and high barrier properties against oxygen and grease (Fotie et al., 2020; Tarrés et al., 2018). Despite these advantages, the use of CNF films in the packaging industry is slowed down because of their inherent sensitivity to moisture and water. Specifically, non-modified CNF films exhibit a much higher water vapor transmission rate (WVTR), commonly exceeding $200 \text{ g/m}^2\cdot\text{day}$ at 50% relative humidity (RH) (Pasquier et al., 2022b), than the commercial plastic substrates they aim to replace, such as PE films with a WVTR of $16.5 \text{ g/m}^2\cdot\text{day}$ at 100% RH (Steven & Hotchkiss, 2002b).

Several strategies have been explored to improve the WVTR of CNF films and involve, among others, the grafting of aromatic polymers like polystyrene (Cheng et al., 2018), esterification of cellulose using anhydrides of different carbon chain lengths (Sehaqui et al., 2014), acetylation of cellulose by *e.g.*, N,N-dimethylacetamide (W. Li et al., 2019), and silylation (Andresen et al., 2006). These strategies have been quite effective in lowering the

water vapor permeability and water uptake of CNF films. For instance, acetylation of CNFs (degree of substitution, DS, of 0.19) resulted in an 80% decrease of the films' water uptake and reduced the films' WVTR at 50% RH from 234 g/m².day (unmodified films) to 167 g/m².day (acetylated films) (W. Li et al., 2019). Such considerable improvements yet remained insufficient to compete with commercial plastic films (Rodionova et al., 2011). Other promising strategies that resulted in even lower WVTR values (Poothanari & Leterrier, 2024; W. Wang et al., 2021), while promising, usually involve the use of toxic chemicals, solvents, or high temperatures, or require multiple reaction steps. Certain chemical reactions were also reported to alter, and potentially impair the inherent properties of cellulose such as crystallinity and strength (Henriksson et al., 2008; Jonoobi et al., 2010), and its biodegradability (Frank et al., 2018). Hence, there is a need for more sustainable and efficient approaches to tailor the surface chemistry of CNF films without altering their bulk properties.

The use of sustainable processing for the functionalization of materials' surface has hence become more attractive for addressing water and moisture sensitivity of lignocellulosic biomass, as these so-called green technologies are seen as more eco-friendly and, in some cases, more time and energy efficient than chemical modification approaches. For instance, dielectric barrier discharge (DBD) plasma can be used to modify the surface properties of lignocellulosic substrates without compromising their bulk performance. Functionalization by plasma does not necessarily require the use of toxic chemicals, solvents, or water (Fazeli et al., 2019) and can be conducted under atmospheric pressure and at low temperature conditions (Kakkar et al., 2020). In addition, plasma is a highly versatile and scalable technique that can be used for finetuning the surface chemistry of substrates by proper selection of the plasma gas

and adapted to roll-to-roll manufacturing of *e.g.*, flexible packaging (Maechler et al., 2011; Profili et al., 2020b).

Previous research has reported successful use of DBD plasma to tailor the wettability of cellulosic surfaces. Coplanar diffusive DBD plasma combined with atmospheric air and nitrogen gases was used to increase the moisture absorption and wettability of newspapers for improved printability (Tóth et al., 2007). The treatment successfully led to a decrease in the water contact angle (WCA) from 134° (untreated substrate) to 49° after plasma treatment, indicative of significant surface oxidation. In contrast, the treatment of chlorine-free bleached softwood pulp with DBD air plasma was found to decrease the wettability of the pulp by enhanced surface roughness. Additionally, this treatment improved the wet strength of the pulp by facilitating the crosslinking of cellulose fibers (Wielen et al., 2006).

In addition to varying the gas composition and plasma geometry to generate different types of surface functionalization, plasma can be used for the deposition of thin molecular layers. For instance, hydrophobization of paper substrates (WCA>120°) was achieved through the deposition and plasma-induced polymerization of butyl acrylate (BA) and 2-ethylhexyl acrylate (2-EHA) monomers onto the cellulose fibers (Song et al., 2013). The deposition of plasma-induced organosilicon fragments onto the surface of lignocellulosic substrates has especially received considerable attention because of its versatility in surface energy modification, durability, stability in different environments, and ability to endow substrates with effective surface barrier properties (Theelen et al., 2012). WCA values higher than 120° were achieved after successive and multiple DBD plasma treatments of a Kraft paper using 2,4,6,8-tetramethylcyclotetrasiloxane (TMCTS) as the organosilicon precursor and helium as the carrier gas (Profili et al., 2020b). The resulted ~1- μ m-thick TMCTS coating was, however,

reported to delaminate in the presence of water, indicating poor adhesion between the multiple coated layers of hydrophobic TMCTS fragments.

One approach to enhance adhesion between layers of organosilicon consists in tuning the surface chemistry of the coating by altering the gas composition that reacts with the organosilicon precursor (J. Zhang et al., 2004). The incorporation of oxidizing gases such as oxygen (O₂), air, and nitrous oxide (N₂O) in the plasma gas line can eliminate the hydrophobic, organic portion (*e.g.*, methyl groups) of the organosilicon coating to enhance the hydrophilicity of the treated surface, such as polycarbonate (Maechler et al., 2011).

Significant progress has been made on plasma-induced deposition of organosilicon fragments onto cellulosic substrates (Babaei et al., 2020, 2023; Profili et al., 2020b, 2023), but there is still a need for deciphering the plasma-induced deposition mechanism onto CNF films (Khakalo et al., 2020b; Vartiainen & Malm, 2016). Because CNF films usually exhibit a lower porosity, a more entangled structure, and a higher surface area with more accessible functional groups than their macroscale counterparts (Henriksson et al., 2008; Osong et al., 2016), their interaction with plasma may differ from what has been observed with wood fibers, textiles, and paper substrates.

In this study, we investigated the deposition of organosilicon by DBD plasma onto the surface of CNF films and the effects of such a treatment on the water and moisture barrier properties of the films. TMCTS was used as the organosilicon precursor and different plasma deposition modes and carrier gases were explored to understand the fragmentation process of TMCTS by plasma and its coating distribution and impact on the CNF films' surface properties. This study proposes a scalable approach for finetuning the performance of CNF films and enabling their utilization in multilayer packaging.

3.3. Experimental Section

3.3.1. Materials

Never-dried Northern Bleached Softwood Kraft (NBSK) pulp was provided by WestRock (Covington, VA, USA) and used as received. 1,3,5,7-tetramethylcyclotetrasiloxane (TMCTS, $O_4Si_4(CH_3)_4H_4$, NMR grade, purity ≥ 99.5 vol%) and anhydrous calcium chloride ($CaCl_2$) (powder, $\geq 97\%$) were purchased from Sigma-Aldrich and used as received.

3.3.2. Production of Cellulose Nanofibril (CNF) and CNF Films

A 10 wt% NBSK pulp was refined using a PFI mill refiner (the Norwegian Pulp and Paper Institute, Norway) at 5000 rpm according to the T248 sp-00, (2000) standard. The refined pulp was passed through a Masuko supermasscolloider grinder (MKCA6-5J®, Sangyo, Japan) at a consistency of 1.7 wt% using a rotation speed of 1200 rpm with varying gap clearance and number of passes, to reach a total energy consumption of 3.61 kWh/kg of dry pulp. The produced suspension was then further processed through an aqueous counter collision (ACC Starburst, Sugino Machine Co., Ltd, Japan) at a jet pressure of 220 MPa, for three passes, to produce an aqueous suspension of CNFs at 0.1 wt%.

Self-standing films of CNFs were produced by water evaporation of a 0.1 wt% aqueous CNF suspension poured into polystyrene Petri dishes of 8.5 mm in diameter. An average film grammage of 10 g/m^2 was targeted. After complete drying at ambient conditions, the films were conditioned at 23 °C and 50% relative humidity (RH) for at least 72 h prior to testing.

3.3.3. Dielectric Barrier Discharge (DBD) Plasma Treatment

The DBD reactor was built with two parallel plate electrodes: the upper plate was a 0.64-mm-thick alumina sheet coated with conductive paint ($3.5 \times 3.0 \text{ cm}^2$), and the bottom one was a stainless-steel plate ($13 \times 9 \text{ cm}^2$) (Figure 1). Plasma was generated by the application of

a sinusoidal voltage with a peak-to-peak amplitude of 18 kV and a frequency of 3 kHz. The discharge was applied with a 1-mm gap between the electrodes and the CNF film. The system operated with two gas lines: one for nitrogen, N₂ (carrier gas at 3 L/min), and another for nitrous oxide, N₂O, (2 mL/min). The flow rates were monitored using a Bronkhorst™ controller (USA).

The CNF films were treated by plasma in static and dynamic modes using 1,3,5,7-tetramethylcyclotetrasiloxane (TMCTS) as the siloxane precursor. In static mode, the bottom plate and CNF films to be treated were kept fixed (**Figure 3.1**). The plasma treatment time was set at 10 min. 15 ppm of TMCTS was suspended in nitrogen gas and introduced in the reactor at 3 L/min. In dynamic mode, the bottom plate was moved back and forth at a speed of 35 cm/min for continuous deposition of TMCTS using N₂ gas, for a total amount of time of 30 min (1st layer). A second treatment with N₂O (oxidizing gas) and N₂ gas was used to produce a 2nd layer. This second treatment was carried out for one (1) min without the presence of TMCTS. A 3rd layer was finally conducted atop the 2nd layer using the same treatment conditions as the 1st layer (TMCTS precursor, N₂ gas and 30 min treatment time). The CNF films were treated in triplicates for each treatment.

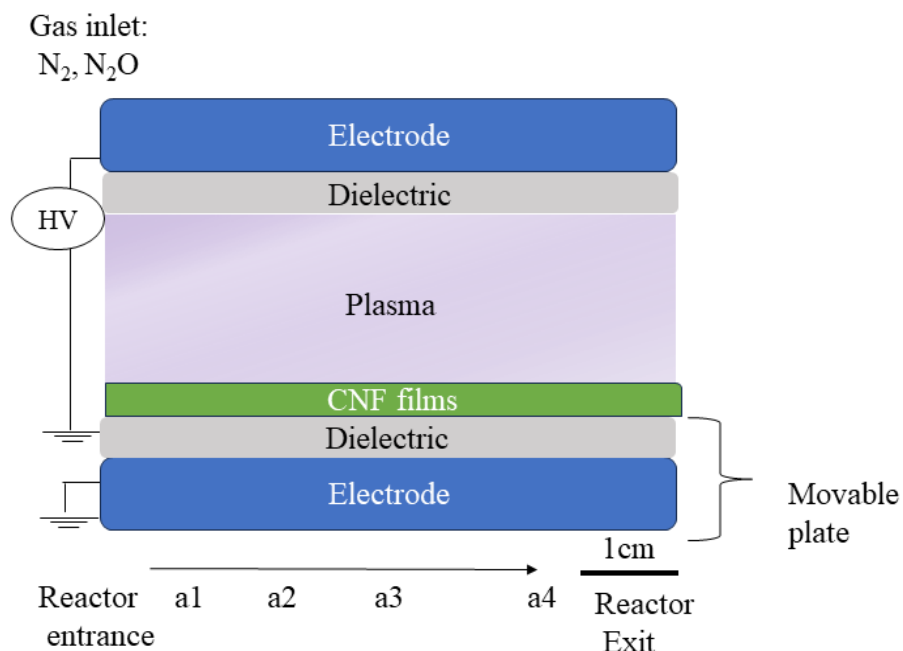


Figure 3.1 Schematic of the side view of the DBD plasma reactor. The inlet gases used as precursor carriers were injected on the upper left, at the entrance of the reactor. The different sample areas of deposition were labelled a0, a1, a2, a3, and a4, corresponding to a distance of 1, ~1.2, 1.5, and 3 cm away from the reactor entrance, respectively.

3.3.4. Characterization of the TMCTS-plasma-induced coating

The plasma-treated CNF films and respective untreated controls were analyzed by Field-Emission Scanning Electron Microscopy (FE-SEM) using a FEI Quanta 250 microscope (Thermo-Fisher Scientific, USA). The acceleration voltage was 12.5 kV, and the working distance was 10 mm. The images were acquired at magnifications ranging from 500× to 1000×. Prior to FE-SEM analysis, the films were coated with a 10-nm-thick gold/palladium (Au/Pd) alloy layer. A minimum of 5 images were acquired per specimen, and the best acquisitions were used for discussion.

3.3.5. Attenuated Total Reflectance Fourier Transformed Infrared Spectroscopy (ATR-FTIR)

The surface chemistry of the plasma-treated films and controls was investigated using an FTIR spectrophotometer (Cary 660 FTIR, Agilent Technologies, Victoria) in ATR mode. Infrared spectra were recorded at room temperature at a resolution of 4 cm^{-1} using a 45° incident ATR accessory (1.5 mm^2 active sample area, Ge crystal with a depth of penetration of $0.170\text{ }\mu\text{m}$ at 3500 cm^{-1}). A total of 128 scans were conducted. For each specimen, 15 equally spaced points were analyzed between the entrance and the exit side of the plasma gas (i.e., between a1 and a4, Figure 1). Measurements were made in triplicates using the OriginPro[®] software (OriginLab[®] Corporation, Software version 9.9). The spectra were normalized to the IR signal of the Si-O-Si asymmetric stretching band at $1200\text{--}1000\text{ cm}^{-1}$.

3.3.6. Water Contact Angle (WCA)

The sessile drop method was applied to measure the water contact angle of the plasma-treated films and controls using a Video Contact Angle System (VCA-2500 XETM, AST products Inc., Billerica, MA, USA) equipped with a high-resolution CCD camera. The volume of the ultrapure water drops was kept at $1\text{ }\mu\text{L}$. Measurements were made at least in triplicates for each plasma treatment and the average water contact angle values were used for discussion.

3.3.7. X-ray Photoelectron Spectroscopy (XPS)

The surface composition of the plasma-treated CNF films and controls was analyzed using an X-ray Photoelectron Spectroscopy (PHI 5600-ci spectrometer, Physical Electronics, Chanhassen, MN, USA) operated under high vacuum ($<10^{-6}\text{ Pa}$). A standard Al X-ray source ($K\alpha$, $h\nu=1486.6\text{ eV}$) at 300W with a charge neutralizer was used to record survey spectra ($0\text{--}1400\text{ eV}$). Standard Mg X-ray source ($K\alpha$, $h\nu=1253.6\text{ eV}$) at 300W was used to collect high-

resolution spectra (HR XPS). Photoelectron detection was carried out at a take-off angle of 45° for a detection area of 0.5 mm². Surface charging effects were compensated for by correcting the C-C/C-H aliphatic carbon binding energy peak at 285.0 eV. Curve fitting of the C 1s and Si 2p was performed using the Gaussian-Lorentzian functions after Shirley-type background subtraction (CASAXPS Version 2.3.25). Nine replicates per plasma treatment were analyzed.

3.3.8. Atomic Force Microscopy (AFM)

AFM analysis was performed using an Asylum research atomic force microscope (Oxford instrument, USA) in tapping mode with an etched silicon tip (OTESPA, tip radius <10 nm). Surface topography was evaluated in triplicates for areas covering 50×50 μm². The AFM images were analyzed using Gwyddion v2.65 software and the surface roughness of the films was determined using the Roughness Average (R_a). R_a is calculated considering the deviation of all points roughness profile from a mean line over the evaluation length of the areas according to ISO 4287/1-1997 standard.

3.3.9. Water Vapor Transmission Rate (WVTR) and Water Uptake of CNF films

The WVTR of CNF films was measured at 23 °C and 50 % RH according to the ASTM E96 (2000) standard. Aluminum cups (68-3000 EZ-Cup, Vapometer, USA) were filled with 5 g of anhydrous CaCl₂. CNF films of 8 cm in diameter (for a tested surface area of 6.25 × 10⁻⁴ m²) were tightly sealed between the cup base and its lid. The increase of the film's mass over time was measured at regular time intervals using an analytical laboratory scale (± 0.0001 g) (Radwag AS-120.R2-PLUS, USA) until a constant change in mass was reached. The experiments were conducted in duplicates for each surface treatment condition, including control films.

The WVTR was calculated as follows:

$$WVTR \left(\frac{g}{m^2 day} \right) = \frac{final\ mass\ (g) - initial\ mass\ (g)}{surface\ area\ of\ the\ film\ (m^2) * (total\ number\ of\ days)}$$

The water uptake of the films was measured using an adapted Cobb test method (TAPPI 441 om-09 (2013)). A metal ring with a test area of 10 cm² was used for the measurements. The initial mass of the film was measured using an analytical laboratory scale (± 0.0001 g) (Radwag AS-120.R2-PLUS, USA). The film was tightly clamped between the metal ring and a solid, metallic surface to enable the pouring of 10 mL of distilled water for full contact with the 10 cm² area, without leaking. A contact time of 20 s was recorded, after which the film was pressed between two blotting papers and weighed again using the same balance. The tests were performed in triplicates and the average water uptake values are used for discussion. The water uptake was calculated as follows:

$$Water\ Uptake\ (\%) = \frac{final\ mass\ (g) - initial\ mass\ (g)}{initial\ mass(g)} \times 100$$

3.4. Results and Discussion

3.4.1. Influence of organosilicon plasma-induced deposition on CNF films' topography

The CNF films were first functionalized by plasma in static mode (*i.e.*, 10-min treatment per position, with fixed plates) to assess the growth dynamics of organosilicon deposition between the entrance and the exit of the plasma reactor. **Figure 3.2** shows the scanning electron microscopy (SEM) images of the films' surfaces before and after organosilicon deposition using TMCTS as the organosilicon precursor and nitrogen plasma (TMCTS/N₂). Four different areas of deposition located between the entrance and the exit of

the reactor (**Figure 3.4.1**) were analyzed, namely at 1 cm (a1, **Figures 3.2B and 3.2C**), 1.2 cm (a2, **Figure 3.2D**), 1.5 cm (a3, **Figure 3.2E**) and 3 cm (a4, **Figure 3.2F**) away from the entrance of the reactor. As the CNF films were functionalized further away from the introduction of the carrier gas and TMCTS precursor, their surface morphology changed significantly.

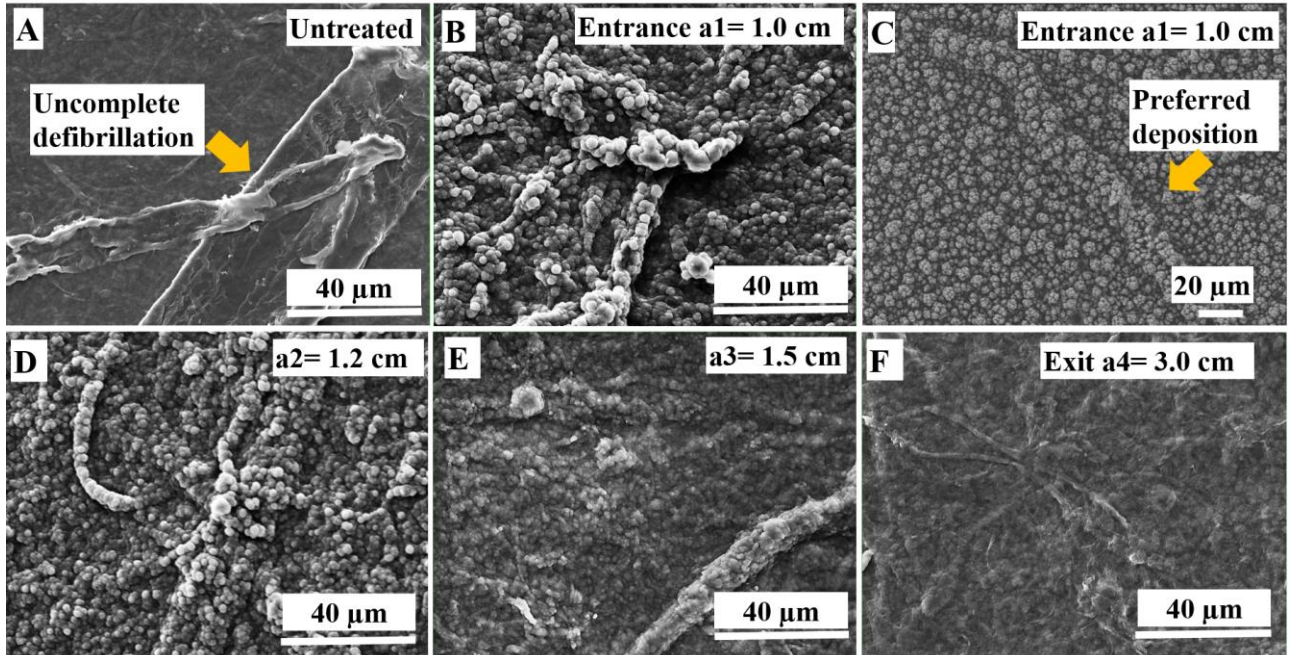


Figure 3.2 Scanning Electron Microscopy (SEM) images of CNF films' surface coated by organosilicon plasma in static mode. (A) Untreated CNF films (controls), plasma-treated CNF films functionalized at (B, F) 1.0 cm, (C) 1.2 cm, (D) 1.5 cm and (E) 3.0 cm away from the entrance of the reactor. Magnification: $\times 1000$.

Compared to the well-reported, tight entangled structure of cast, neat CNF films (**Figure 3.2A**) (Kim et al., 2021), the films that were treated closer to the entrance of the reactor (a1 and a2) demonstrated a rougher surface topography that was entirely covered by cauliflower-like spheres (**Figures 3.2B, C, and D**). Such observation was accentuated in the presence of non-fully processed fibers, whose morphology was revealed with the localized,

preferred assembly of TMCTS spheres along the fibers' length, as shown in **Figure 3.2C**. The observed increase in surface roughness was additionally confirmed by Atomic Force Microscopy (AFM) with the measurement of a roughness average (Ra) of 58 ± 8 nm for the control CNF film against 171 ± 8 nm for the plasma-treated films at the position a1 (**Table 3.4.1**). This phenomenon correlates with the growth mechanism of the coating, primarily driven by the localized nucleation of the reactive species on the regions exposed to higher fragment concentrations (i.e., closer to the middle of the electrode gap) or having specific features (e.g., fiber edges) that potentially enhance the electric field (Profili et al., 2020).

As we moved towards the exit of the reactor (a3 and a4 positions, **Figures 3.2D and E**), the surface morphology of the treated CNF films became less and less granular, yet remained rougher than the surface of the non-treated CNF films. These SEM observations were supported by the measurement of the films' roughness: the films in a4 position showed a roughness of 77 ± 8 nm, slightly higher than the neat films' roughness (**Table 3.1**).

Table 3.1 Average roughness (Ra) values of CNF films before and after plasma treatment at the position 1 cm (a1), 1.5 cm (a3) and 3 cm (a4) away from the reactor entrance. The average roughness values were measured by Atomic Force Microscopy.

	Untreated CNF films	a1	a3	a4
Ra (nm)	56 ± 9	171 ± 16	78 ± 4	76 ± 8

The non-uniform plasma discharge can result in uneven energy distribution across the reactor (Tyl et al., 2018), in turn leading to the generation of different organosilicon species as well as different concentrations of fragments throughout the reactor. For instance, Babaei et al. (2020) studied the transport phenomena of hexamethyldisiloxane (HMDSO) fragments in a glow-like discharge at atmospheric pressure (i.e., helium DBD plasma reactor) on Kraft paper (Babaei et al., 2020). Their findings indicated clear variations of coating morphology along the

gas flow lines which affected the water contact angle of the cellulosic substrate. These findings suggest that the observed changes in CNF films' morphology obtained in a homogeneous Townsend discharge (*i.e.*, N₂) remains similar to the ones previously observed with a glow-like discharge (*i.e.*, He) despite the different energies involved. Further studies are necessary to compare both physical regimes and confirm whether variations in energy distribution is a determinant factor in the observed changes in surface properties of the CNF films.

3.4.2. Influence of Plasma-Induced Fragmentation of TMCTS on CNF Films' Surface Properties

With the observed differences in the films' surface topography across the reactor's length, variations in the films' surface chemistry and chemical functional groups distribution were investigated to identify the plasma conditions that would enable enhanced barrier performance of the films.

Figure 3.3 shows the infrared spectra of CNF films before and after plasma functionalization at the different a1 to a4 positions.

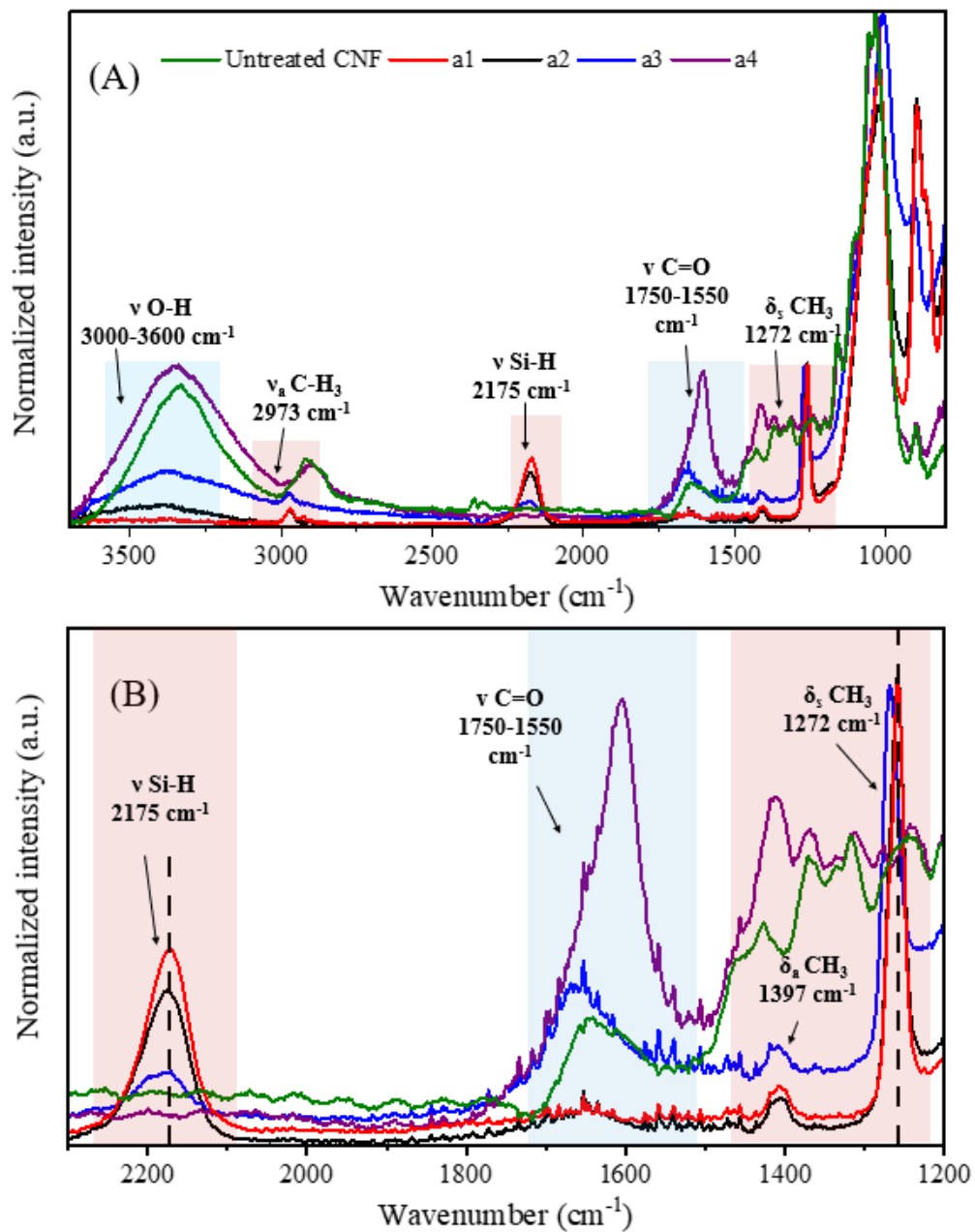


Figure 3.3 Infrared (IR) spectra of untreated CNF films and films treated by organosilicon plasma in a1, a2, a3, and a4 positions (i.e., 1 cm, ~1.2 cm, 1.5 cm, and 3 cm away from the entrance of the reactor) between (A) 3600-800 cm^{-1} and (B) zoomed area from 2100 to 1200 cm^{-1} .

Compared to the spectrum of the untreated CNF films, the spectrum of the films that were functionalized near to the entrance of the plasma reactor (i.e., positions a1 and a2, **Figure**

3.3) shows the absence of the O–H vibration signal in the 3000-3600 cm^{-1} range. Additionally, the appearance of new peaks at 2175 cm^{-1} assigned to Si-H stretching, and at 1272 cm^{-1} assigned to Si-CH₃ bending, indicates the deposition of an organosilicon layer onto the CNF films' surface (Ryan et al., 2014; Zhang et al., 2004) at the a1 and a2 positions. The thickness of the organosilicon layer is estimated to be higher than 0.17 μm when considering the depth of the IR analysis in this wavenumber range (3000-3600 cm^{-1}). For the films treated further away from the reactor's entrance (a3 and a4 positions), the intensity of the signal in the 3000-3600 cm^{-1} range gradually increased, suggesting the formation of silanol groups (Si-OH) or the decrease in thickness of the organosilicon coating. Silanol groups can be formed from the reaction of organosilicon fragments with water molecules from the air moisture (Joshi et al., 2006; Rodríguez Durán et al., 2020). The intensity of absorption of Si-H stretching observed at 2175 cm^{-1} (**Figure 3.3B**) is indicative of the degree of fragmentation of TMCTS (Zhang et al., 2004). Notably, higher absorption levels at 2175 cm^{-1} were recorded near to the reactor entrance (a1 and a2 , **Figure 3.3B**), suggesting the deposition of higher molecular weight fragments at the entrance of the plasma reactor than at its exit, which exhibited lower signal intensities to no detected signal (a3 and a4, **Figure 3.3B**). On the other hand, the absence of the Si-H stretching signal in the IR spectrum of CNF films treated in a4 can be assigned to a higher fragmentation intensity of TMCTS, suggesting that low molecular weight fragments are evidenced at the reactor exit.

Figure **3.3B** shows two additional prominent absorbances at 1272 cm^{-1} and 1397 cm^{-1} , which are characteristic of the symmetric and asymmetric bending of the organic part (-CH₃ groups) inherent to the TCMTS chemical structure (Barreca et al., 2007). The intensity of these two signals is similar for the films treated in positions a1 and a2, suggesting that the deposition

of non-fragmented TMCTS is more predominant at the entrance of the reactor than at its exit since a lower hydrocarbon content was observed in the a3 and a4 IR spectra (Figure 3.4.2B). These findings are supported by Zhang et al. (2004), who investigated the mechanism of fragmentation of organosilicon coatings in radiofrequency plasma across different discharge regions. Their studies revealed that at 5 and 10 cm downstream from the discharge region, i.e., away from the reactor's entrance, no hydrocarbons were detectable in the silicon dioxide films' IR spectra. Additionally, in our study, new absorption signals were found at positions a3 and a4 (**Figure 3.3B**) within the 1550-1750 cm^{-1} range, most likely arising from C=O stretching attributed to carbonyl-containing functionalities such as carboxyl (COOH), ester (COOR), or amide (CONH) groups (Reuter et al., 2012). Furthermore, this new peak might also indicate surface oxidation. The rise of polar groups such as silanol (Si-OH) and carbonyl functional groups (**Figure 3.3B**) will potentially increase the film wettability.

At this stage, we have shown that the polymerization process induced by DBD plasma changes the chemical nature of the thin coated organosilicon layer through different fragmentation, and these fragmentations are dependent on different energies applied to the system between the entrance and the exit of the reactor. The explanation of the obtained results with lower TMCTS fragmentation (i.e., higher hydrocarbon content) close to the reactor entrance can be related to the modification of the power discharge-to-fragment flow ratio (W/F), which varies as a function of the position in the plasma reactor. According to Petersen et al. (2011), a lower W/F ratio tends to generate organosilicon coating polydimethylsiloxane-like $[(\text{Si}(\text{CH}_3)_2\text{O})]$ structures, while a higher W/F ratio would reduce the organic portion of the precursor and favor the formation of silica-like (SiOx) structures (Petersen et al., 2011). Transitions to higher surface power values along the gas flow in the reactor have been observed

in similar systems with DBD and nitrogen-based discharges (Tyl et al., 2018). In the present case, we hypothesized that the W/F ratio exhibits lower values at the reactor entrance, which suggests that the gradient observed in the chemical structure of the CNF films throughout the reactor can be attributed to variations in plasma discharge, and more specifically to variations in reactor's power.

3.4.3. Wetting Behavior of Plasma-Treated CNF films

The introduction of new chemical functionalities on the surface of the CNF films through heterogeneous plasma deposition of organosilicon fragments with different chemistries is expected to endow the films' surface with different degrees of wettability. As highlighted in the literature, the wettability of plasma-treated surfaces depends on the degree of precursor's fragmentation (Asadollahi et al., 2019). **Figure 3.4** shows the contour plot of the water contact angle (WCA) values measured across the surface area of the plasma-treated films (from a0 to a4). The *x*-axis indicates the length of the reactor, while the *y*-axis represents the distance from the entrance to the exit of the reactor.

The WCA values varied significantly across the treated surface area: from 120° (a1 position, 1 cm away from the reactor's entrance) to ~34° at the reactor's exit (a4 position, 3 cm away from the reactor's entrance) (**Figure 3.4**). The predominance of organic content (-CH₃) near the entrance of the reactor, as indicated by the IR spectrum (**Figure 3.3B**), correlates with the hydrophobic nature of the films observed at a1. This same region also exhibited the highest roughness value ($R_a = 171 \pm 16$ nm, **Table 3.1**), which likely contributed to the increased hydrophobicity (Spori et al., 2008). In contrast, the increase in polar groups such as silanol (Si-OH) and carbonyl functional groups at the reactor's exit correlates with the observed decrease in WCA (**Figure 3.4B**).

The results obtained from the plasma-induced deposition of organosilicon in static mode suggest that one can potentially increase the films' overall hydrophobicity as well as their barrier properties using a dynamic deposition mode that serves to reproduce the hydrocarbon content of the areas closer to the reactor entrance, but throughout the films' surface.

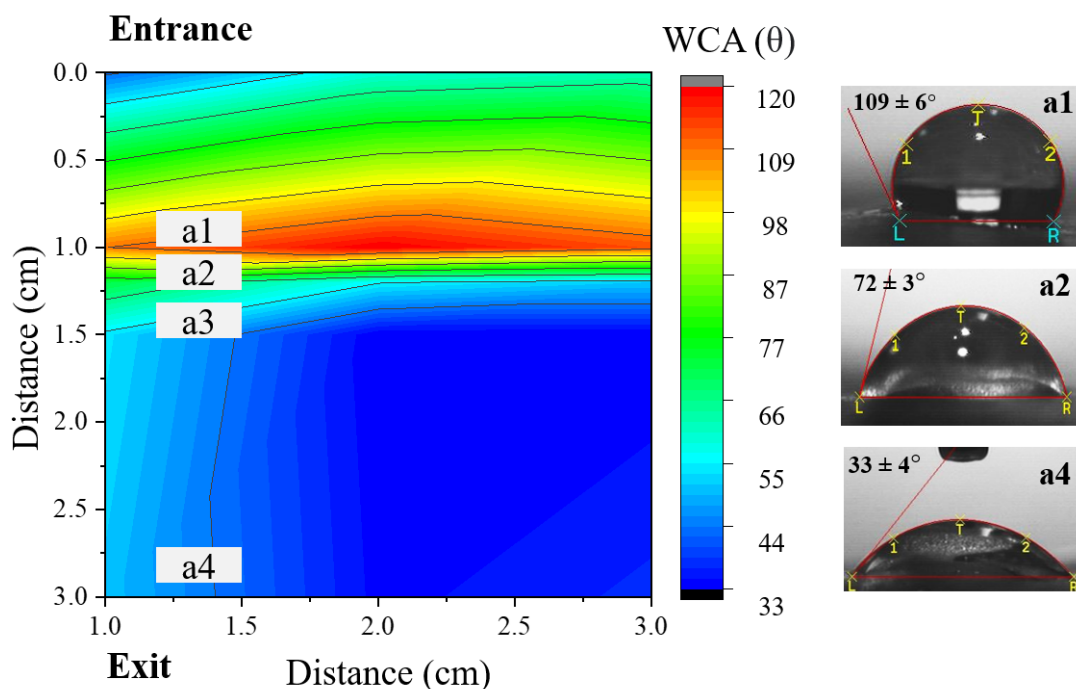


Figure 3.4 Contour plot of the water contact angle values recorded across the surface area of the plasma-treated CNF films ($3 \times 3 \text{ cm}^2$). The top left corner of the plot ($y=0$) indicates the entrance of the DBD reactor and the bottom left corner ($y=3 \text{ cm}$), the exit of the reactor. The images of the water contact angle recorded at the position a1, a2, and a4 (*i.e.*, 1 cm, $\sim 1.2 \text{ cm}$, and 3 cm away from the entrance of the reactor) are shown on the right of the contour plot.

3.4.4. Plasma-induced organosilicon deposition in dynamic mode

To enhance the coating homogeneity across the surface area of the films, plasma deposition of the organosilicon precursor was carried out in dynamic mode for 30 min. The parameters were adjusted to achieve the highest WCA value determined previously (*i.e.*, at the

position a1, 1 cm away from the entrance of the reactor). This new approach aims to enhance the water and moisture barrier properties of the CNF films, in addition to potentially facilitating large-scale industrial applications of DBD plasma for the functionalization of e.g., roll-to-roll manufactured CNF films. **Figure 3.5** shows the SEM images of the surface of the films after 30 min of plasma functionalization in dynamic mode, using TMCTS as the precursor and nitrogen as the carrier gas (TMCTS/N₂).

Irrespective of the treatment location (*i.e.*, a1, a3 or a4), a few macroscale fibers can still be identified on the films' surface after plasma functionalization, suggesting that in dynamic mode as well, the deposition of organosilicon fragments was carried out at a thickness >0.17 μm. Compared to the films treated in static mode, the surface of the CNF films functionalized in dynamic mode were all fully recovered with a uniform cauliflower-like texture, very similar to that of the films' surface treated in a1 position in static mode (see Figure 3.3). This uniform coverage was characterized by a high WCA value of 150° (± 2°) across all three positions between the entrance and the exit of the plasma reactor (Figure 6, Inserts). Compared to untreated CNF films, which exhibited a WCA of 44° (± 3°), the organosilicon-functionalized CNF films demonstrated a superhydrophobic surface. Traditional chemical approaches, such as silylation, have also enabled the creation of superhydrophobic surfaces. For instance, the reaction of TEMPO-oxidized CNFs with a polysiloxane resulted in a high WCA value of 159.6° (S. Chen et al., 2018). This method, however, involved multiple reaction steps and a total reaction time of 40 min to enable uniform silylation of the films' surface. In contrast, the functionalization by plasma enabled the uniform coverage of the films by organosilicon fragments, in one step, in 30 min.

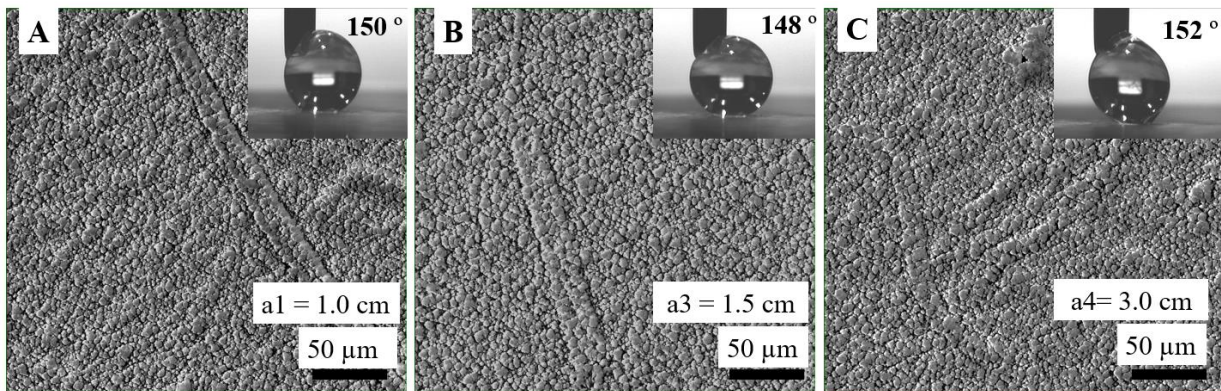


Figure 3.5 SEM images of CNF films' surface after plasma functionalization in dynamic mode between the entrance and the exit of the reactor. (A) Position a1, 1 cm away from the reactor's entrance, (B) a3, 1.5 cm away, and (C) a4, 3 cm away. Magnification: $\times 500$. Inserts show the image of a water drop on the plasma-treated films' surface at positions a1, a3, and a4 with the respective measured contact angle values.

3.4.5. Surface chemistry of CNF films functionalized in dynamic mode

FTIR and XPS analyses were conducted to provide insights into the surface chemistry of functionalized CNF films (with an IR penetration depth of $0.17 \mu\text{m}$ and XPS penetration depth 5 nm) and reveal the composition and chemical states of their topmost layer after plasma treatment in dynamic mode. Because the films' morphology (Figure 3.4) resembled the morphology of CNF films treated in a1, in static mode (Figure 3.1), we expected the surface chemistry of both systems to be similar.

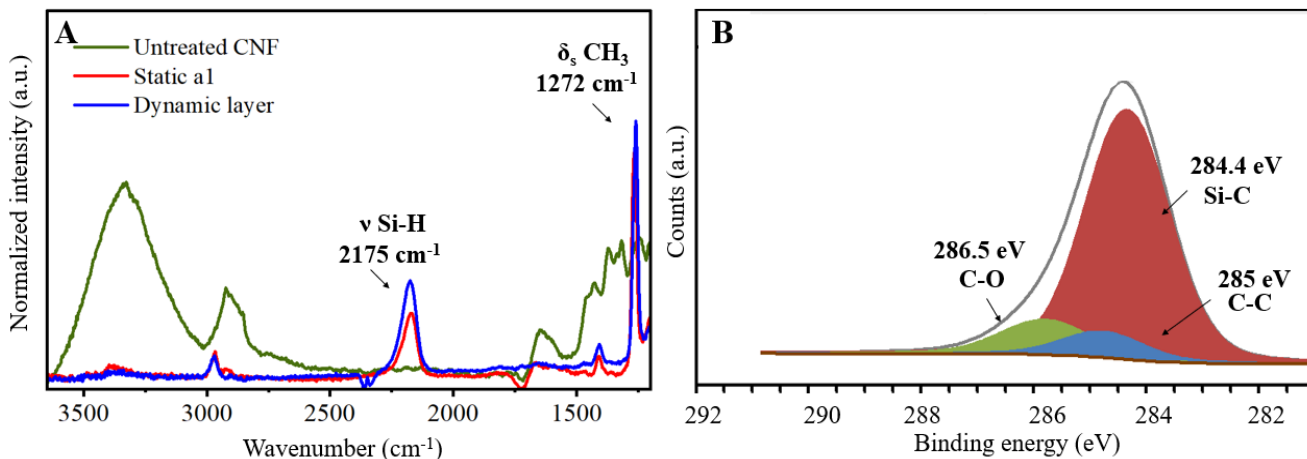


Figure 3.6 (A) Infrared spectra (FTIR-ATR) from 3600 to 800 cm⁻¹ of the untreated CNF (green line), static mode area a1= 1 cm (red line), and the layer treated at the dynamic mode (blue line) and (B) Deconvoluted Carbon 1s photoelectron spectrum of CNF films after organosilicon deposition by plasma in dynamic mode.

The IR spectrum of the CNF films functionalized in dynamic mode (“Dynamic layer” label, Figure 7A) shows predominant peaks that are characteristic of the organosilicon coating. Specifically, the Si-H and Si-CH₃ stretching at 2175 cm⁻¹ and 1272 cm⁻¹, respectively, can be observed. These bands also appear in the IR spectrum of the films treated in static mode, position a1 (**Figure 3.6A**). The absorbance of these two peaks is much higher after functionalization in dynamic mode than in static mode, indicating the deposition of a thicker layer of TMCTS fragments with a higher hydrocarbon content in dynamic mode. Such a difference can be explained by the extended plasma treatment time that was used in dynamic mode, *i.e.*, 30 min (vs. 10 min in static mode).

Accordingly, the deconvoluted areas of the C1s XPS spectrum were primarily attributed to the Si-C bonds at 284.4 eV (Figure 7B). The signals at 286.5 eV and 285 eV can be attributed to the C-O and C-C binding energies of cellulose, respectively, and represent 12.1% and 7.2% of the surface chemical composition of the films, respectively (Table 2).

These low percentage concentrations suggest that the films' surface was not entirely covered by the organosilicon fragments at the molecular level, contradicting our first conclusion drawn from the SEM observations. The presence of molecular defects in the organosilicon coating, yet, did not impact the development of a superhydrophobic films' surface.

Table 3.2 XPS percentage atomic concentrations of C1s components on the CNF films' surface after organosilicon deposition by plasma, in dynamic mode.

Element	Si-C	C-C	C-O
Binding energy (eV)	284.4	285	286.5
Atomic Concentration (%)	80.7	12.1	7.2

The analysis of the CNF films' surface morphology and chemistry after plasma treatment in dynamic mode confirms that the target conditions and performance (here, a high water contact angle value) identified in static mode can be reproduced in dynamic conditions with an extended plasma treatment time. Compared to the functionalization in static mode, the dynamic approach enabled a uniform deposition of organosilicon fragments on the surface of the CNF films, which in turn, resulted in a uniform hydrophobization of the films' surface. Such a result is expected to contribute to the moisture and water barrier performance of the CNF films; yet, the small coating cavities that were observed by XPS, may be large enough to facilitate moisture diffusion through the films and in turn, weaken the films' barrier performance.

Hence, we adopted a multi-layer approach to counteract the presence of molecular defects (or holes) in the single plasma-coated layer of organosilicon fragments. The stacking of multi-layers of different barrier performance is commonly exploited for the manufacturing of high-barrier flexible packaging substrates (Fahlteich et al., 2015). Thus, this strategy has been implemented to further develop the barrier performance of the CNF films.

3.4.6. Tuning the wettability of CNF films by multilayer plasma treatment

The wettability and surface chemistry of the CNF films treated in dynamic mode using TMCTS/N₂ plasma, were tuned by altering the composition of the plasma gas from TMCTS/N₂ to N₂O/N₂ in order to modify the nature of the functional groups of the coated organosilicon fragments. The use of nitrous oxide gas (N₂O) aims to oxidize TMCTS and remove the hydrophobic functional groups (such as -CH₃) from the coated fragments (Maechler et al., 2011). This second plasma treatment (or second layer) was applied on the surface of the already-plasma-treated CNF films (with TMCTS/N₂) to increase their wettability and prepare them for a third plasma treatment. This latter was then conducted using TMCTS/N₂ plasma (composition similar to that of the first layer) on the films' surface, right after the N₂O/N₂ plasma treatment. The second plasma treatment (*i.e.*, N₂O/N₂) served as an intermediate layer, aiming to improve the uniformity and coverage of the organosilicon coating onto the CNF films' surface. We hypothesized that such a thin, hydrophilic layer could also help prevent potential delamination of successive organosilicon layers, which was observed and reported by Profili et al. (2020). Figure 8 shows the SEM images of the CNF films' surface after 1 min of plasma functionalization in dynamic mode using the oxidizing gas mixture N₂O/N₂ (*i.e.*, second layer, Figure 3.6A) and after organosilicon coating using TMCTS/N₂ for 30 min (*i.e.*, third layer, Figure 3.7B).

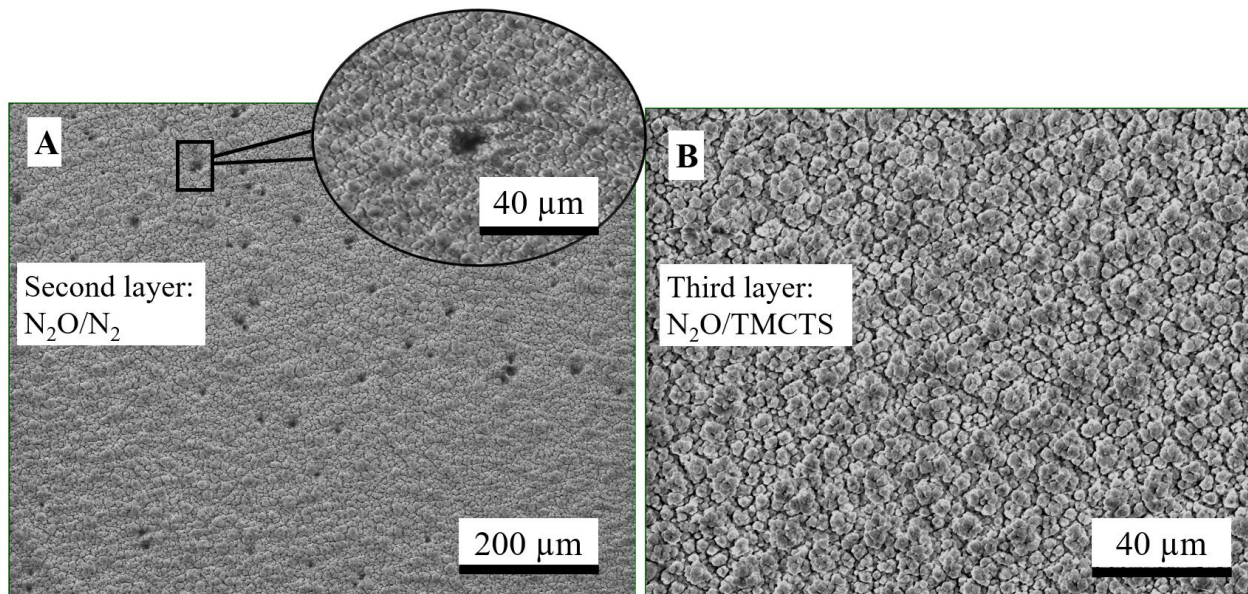


Figure 3.7 SEM images of the organosilicon-coated CNF films' surface after (A) a second plasma layer using N₂O/N₂ and (B) a third plasma layer using TMCTS/N₂. Magnifications: (A) ×200 and ×500 (insert), (B) ×1000.

The second plasma treatment induced apparent structural defects on the films' surface that can be related to physical etching (Figure 3.7A, Insert). This phenomenon can be attributed to changes in the physical regime of the discharge (Merche et al., 2012), potentially leading to instabilities such as those observed in a filamentary regime. Filamentary discharges are common when treating cellulosic substrates in DBD reactor at atmospheric pressure and have been observed in previous studies (Profili et al., 2020). As discussed in the literature, the presence of defects, such as variations in the films' topography or a wavy surface, can alter the physical regime (Rajasekaran et al., 2010). Interestingly, the deposition of the third plasma layer, using TMCTS/N₂, enabled the coverage of the defects induced by the N₂O/N₂ plasma treatment (Figure 3.7B). Similar to the first layer (Figure 3.4), the third one exhibited a cauliflower-like structure (Figure 3.6B), which can also be attributed to the uniform deposition of organosilicon fragments onto the films' surface.

The surface roughness of the three layers was also measured by AFM (Table 3). The first and third layers obtained by TMCTS/N₂ plasma, presented higher average roughness values than the second layer obtained by N₂O/N₂ plasma. The highest surface roughness of the third layer suggests the formation of TMCTS cluster in the plasma, which could result in powder inclusion during organosilicon deposition (Van Assche et al., 2014). Such a phenomenon may be due to the excessive plasma treatment time (here, 30 min).

Table 3.3 Average roughness (R_a) values of first TMCTS/N₂, second N₂O/N₂ and third plasma layer using TMCTS/N₂. The average roughness values were measured by Atomic Force Microscopy.

	First layer	Second layer	Third layer
Plasma treatment	TMCTS/N ₂	N ₂ O/N ₂	TMCTS/N ₂
R_a (nm)	225 ± 9	190 ± 52	245 ± 4

The surface chemistry of the CNF films after deposition of the second and the third layer by plasma also reveals clear distinctions. Figure 9A shows the characteristic peaks of the organosilicon coating at 2172 cm⁻¹ and 1262 cm⁻¹ assigned to Si-H stretching and Si-CH₃ bending, respectively, on the spectrum of the three plasma layers (Todd Ryan et al., 2014; J. Zhang et al., 2004). Despite the presence of the second plasma layer conducted with a mixture of oxidizing gases, the signals of the organosilicon fragments were still detectable by IR and exhibited similar intensities. This suggests that (i) the second plasma treatment did not affect the fragmentation of the organosilicon precursor within the depth of analysis (0.17 μm) and (ii) the oxidation process primarily affected the topmost nanometer layer of the films (Chang, 1983). In fact, the introduction of an oxidizing gas was expected to increase the oxidation

intensities of the films, which was confirmed by XPS analysis, showing a 70% increase in the O/C ratio of the CNF films treated with N_2O/N_2 (Table 4).

Compared to the IR spectrum of the first layer (Figure 3.8A), the spectra of the second and third layers also show an increase of the O-H stretching signal intensity ($3600-3000\text{ cm}^{-1}$) due to the interaction of the organosilicon coating with air moisture. Moreover, a weaker absorption signal in the $1550-1750\text{ cm}^{-1}$ range, most likely indicating the presence of carbonyl-containing functionalities, can also be observed on both IR spectra (Reuter et al., 2012). In the case of the second plasma treatment, XPS analysis confirmed the presence of amide ($N-C=O$) functional groups (signal at 289.2 eV, Figure 9B) on the surface of the CNF films treated by NO_2/N_2 plasma. This functional group was potentially introduced by the nitrogen from the oxidizing gas, as observed in previous studies (Reuter et al., 2012; Rodríguez Durán et al., 2020). In the case of the third layer, that was not treated with an oxidizing plasma gas, the presence of carbonyl-containing functionalities observed in the IR spectrum in the $1550-1750\text{ cm}^{-1}$ range, may be explained by the involuntary injection of oxygen in the gas phase by substrate outgassing (Levasseur et al., 2013), which can explain why the O/C ratio of the third layer was 30% higher than that of the first plasma layer (**Table 3.4**).

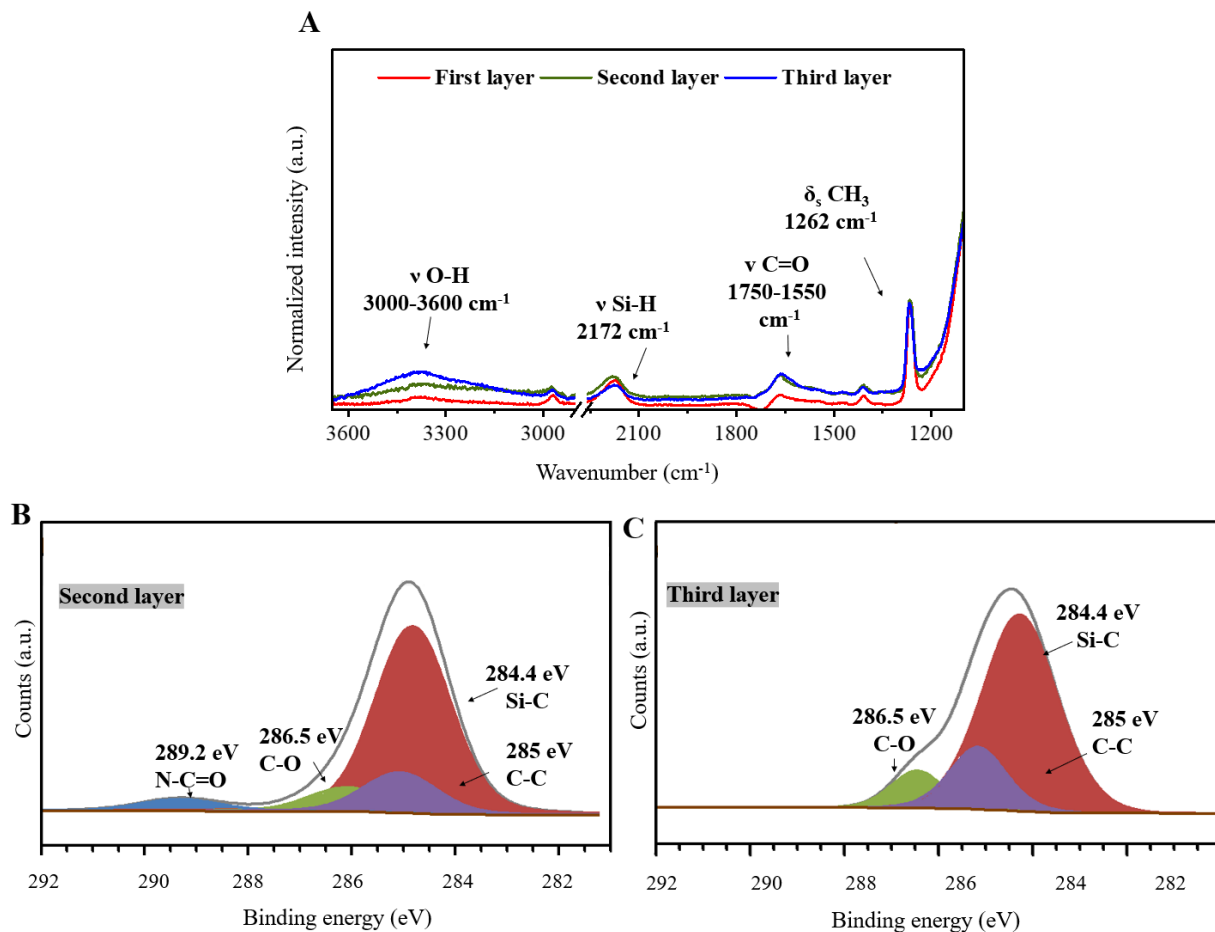


Figure 3.8 Surface chemistry analysis of the organosilicon-coated (A) CNF films after deposition of a first layer with TMCTS/N₂, a second layer with N₂O/N₂, and a third layer with TMCTS/N₂. Infrared spectra from 3600 to 800 cm⁻¹, and XPS photoelectroncarbon C_{1s} spectra of the (B) second layer and the (C) third layer.

Table 3.4 Averages and standard deviations of XPS screenings of a first layer with TMCTS/N₂, second layer with N₂O/N₂, and a third layer with TMCTS/N₂.

	Plasma treatment	Carbon (C) %	Oxygen (O) %	O/C
First layer	TMCTS/N ₂	26.56 ± 0.54	28.88 ± 0.30	1.0 ± 0
Second layer	N ₂ O/N ₂	20.58 ± 0.81	34.74 ± 0.39	1.7 ± 0.1
Third layer	TMCTS/N ₂	22.89 ± 0.82	30.42 ± 1.21	1.3 ± 0.1

The wettability of the CNF films after the second and third plasma treatment is shown **Figure 3.8** and evidences the clear difference in surface chemistry between the second and third plasma treatment.

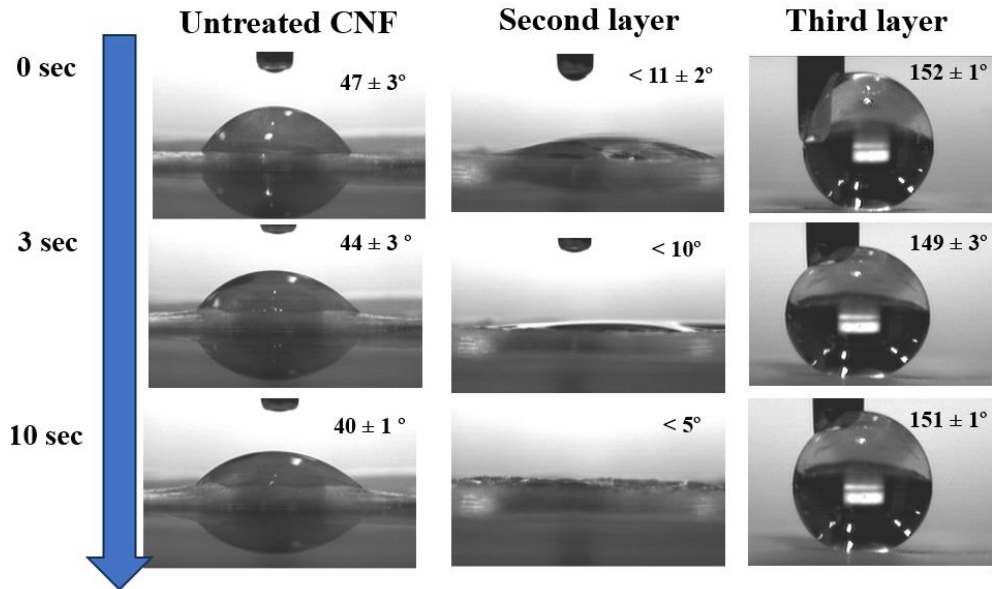


Figure 3.9 Dynamic water contact angle analysis of the CNF films after 0, 3 and 10 seconds of contact with the water drop. (*left column*) Untreated CNF films' surface, CNF films after (*middle column*) two plasma layers (TMCTS/N₂ and N₂O/N₂), and (*right column*) three plasma layers (TMCTS/N₂ - N₂O/N₂ - TMCTS/N₂).

The untreated CNF films had an initial WCA of $47 \pm 3^\circ$ that gradually decreased overtime until reaching $40 \pm 1^\circ$ after 10 seconds (Figure 10, left column). CNF films have a known hydrophilic nature due to the presence of hydroxyl groups that allow them to interact with considerable amounts of water (Solhi et al., 2023).

As observed in **Figure 3.9**, the TMCTS/N₂ plasma treatment also led to a superhydrophobic surface with a WCA $>150^\circ$ (**Figure 3.9**, right column). In contrast, the treatment of the films with N₂O/N₂ plasma decreased the WCA to an initial value of $11 \pm 2^\circ$

(**Figure 3.9**, middle column). Within 3 seconds, complete spreading and disappearance of the water droplet on the films' surface was observed. This second oxidizing plasma treatment effectively removed the hydrophobic functional groups of the previously deposited organosilicon coating, creating a hydrophilic layer on the top of the first hydrophobic layer, as previously shown by XPS (**Table 3.4**). These observations align with the literature, where treatments involving oxidizing gases such as N_2O have been shown to modify the surface chemistry of TMCTS, enhancing the hydrophilicity of the deposited fragments ($WCA < 5^\circ$) through the introduction of polar functional groups (Durán et al., 2020). The enhanced hydrophilicity of the CNF films' surface did not alter the effectiveness of the third plasma treatment using TMCTS/ N_2 . This latter reestablished the superhydrophobicity of the CNF films' surface, showing a stable WCA value of 150° .

Because the presence of a superhydrophobic surface does not necessarily endow the bulk material with high barrier performance against water and moisture (Wang et al., 2018), we tested the water vapor transmission rate (WVTR) and water absorption capacity (WA) of the CNF films, after a first, a second, and a third plasma treatment. The results are shown in **Figure 3.10**.

The second plasma treatment resulted in a drastic increase of the WVTR that exceeded the performance of the untreated CNF films. Such an increase in moisture transfer may be due to the combined effect of the increased hydrophilicity of the CNF films' surface and the introduction of structural defects in the films, that were observed Figure 8. Despite the increase in WVTR, the WA of the films remained low, demonstrating the effectiveness of the hydrophobic layers in mitigating water absorption into the cellulose substrate.

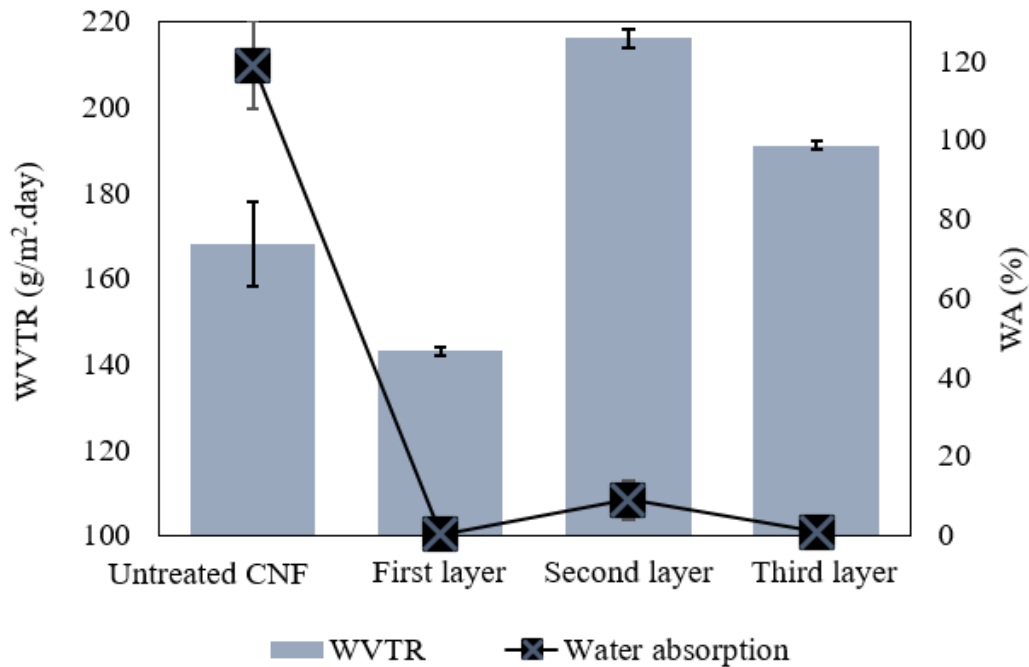


Figure 3.10 Water vapor transmission rates (g/m².day) and water absorption (%) of the untreated CNF films, and films functionalized by one (TMCTS/N₂), two (layer 1 + N₂O/N₂)

The treatment of the films with a third plasma layer (TMCTS/N₂) resulted in a WVTR of 180 g/m².day, which remained higher than the WVTR of the untreated CNF films. While the SEM observations suggested complete coverage of the defects induced by the second plasma treatment, nano- and sub-nano-sized pores may still be present in the films after plasma deposition of molecular fragments. The increased roughness of the third plasma layer may also have contributed to the higher WVTR values. As previously shown by Van Assche et al. (2014), a high surface roughness combined to the presence of defects can lead to more accessible pathways for moisture permeation. In contrast, the WA of the CNF films treated with three layers remained low, at 1%, demonstrating the effective water-resistant nature of

the coating and its ability to mitigate hydrophilicity and the action of capillary forces on water absorption.

Further studies will thus be necessary to optimize the plasma-induced multi-layer deposition of organosilicon fragments onto the CNF films to develop higher moisture barrier performance, since acting on the surface chemistry alone is not sufficient to meet moisture barrier requirements of food packaging.

3.5. Conclusions

This study investigates the potential of dielectric barrier discharge (DBD) plasma in tuning and tailoring the surface properties of CNF films for enhanced water and moisture barrier performance. Plasma deposition of an organosilicon precursor in static mode proved to be an effective approach to understand the preferential deposition and fragmentation process of the precursor onto the CNF films' surface between the entrance and the exit of the plasma reactor. Specifically, the static-mode approach served as a foundation to a more controlled plasma treatment, conducted in dynamic mode for scalability, that resulted in the formation of a uniform, porous superhydrophobic coating onto the entire CNF films' surface.

Through the dynamic mode approach, a multi-layer strategy was then implemented for the finetuning of the barrier properties of the CNF films. Successive hydrophobic and hydrophilic layers were applied onto the CNF films by varying the nature of the plasma gas. The introduction of an oxidizing gas increased considerably the wettability and hydrophilicity of the previously hydrophobized CNF films by plasma-induced organosilicon coating, but generated structural defects that were responsible for the marginal decrease in moisture transfer. However, this second hydrophilic layer enabled the deposition of another plasma-

induced organosilicon coating that exhibited a superhydrophobic surface and a very low (<1%) water absorption capability.

The ability to tailor surfaces through plasma treatment holds promise for enhancing the water barrier of CNF films through molecular coating of organosilicon fragments and for improving the films' wettability to serve *e.g.*, as an intermediate tie layer in a multilayer packaging system. Further research is still needed to understand how the creation of structural defects by plasma can be minimized to ultimately mitigate the effect of plasma on the moisture barrier performance of CNF films.

CHAPTER 4: Exploring the role of biomass' chemical composition in the production and properties of lignin-containing cellulose nanofibrils (LCNFs) through CRISPR multiplex-edited hardwood

4.1. Abstract

The potential of biomass as sustainable alternative to petroleum-based polymers has been largely explored, including the use of lignin-containing cellulose nanofibrils (LCNFs). This has been driven by their potential in applications such as in packaging, composites, or additives. Unlike cellulose nanofibrils (CNFs), which require intensive chemical treatments to remove lignin, the LCNFs can bypass these steps, reducing production costs and potentially the environmental impacts. Furthermore, the presence of lignin can provide unique properties to the LCNF, such as antioxidants properties and ultraviolet light (UV) resistance. Despite the potential of LCNFs, there is no clear elucidation on how the chemical composition of biomass, especially lignin, affects the LCNF process and properties. This study investigated the influence of the chemical composition of woody biomass on the mechanical defibrillation process and the properties of subsequent LCNF.

Different chemical compositions of CRISPR-Cas genome-edited poplar woods were evaluated with the goal to produce high-quality grades of LCNFs. The CRISPR biomass presented an increased amount of ether bonds that facilitated the lignin removal by Kraft pulping, moreover, the CRISPR biomass presented incorporation of aldehydes that are not found in the wildtype. Overall, the presence of a high hemicellulose contributed to lowering the energy consumption of the mechanical production route to 25% less when compared to the wildtype. The residual lignin from CRISPR biomass after pulping is more reactive, with a high

amount of carboxylic groups. This increased the Water Retention Values (WRV) and enhanced the defibrillation process, leading to complete defibrillation of LCNFs and superior mechanical performance of films (up to 50% better) compared to the wild type, while the moisture barrier was not affected. For the first time, we provide valuable insights into the proper selection of feedstock by CRISPR-edited biomass for CNF production. This approach can potentially overcome barriers to commercializing LCNF for advanced materials applications by using tailored biomass feedstock.

Keywords: CRISPR, genome-edited hardwoods, cellulose nanofibrils, lignin-containing nanocellulose; monolignol

4.2. Introduction

With the rapid development of nanotechnology and the increasing demand for sustainable and renewable products, the use of biomass has emerged as a potential feedstock to produce advanced nanomaterials (K. Liu et al., 2021). Lignin-containing cellulose nanofibrils (LCNFs) are flexible nanostructures derived from biomass with diameters in the nanometer scale and lengths that can reach several microns (Solala et al., 2020). LCNFs can be derived from the mechanical breakdown (defibrillation) of unbleached biomass pulp in water (Albornoz-Palma et al., 2020).

While most of the studies in literature report the use of bleached biomass to produce cellulose nanofibrils (CNFs) (Noremylia et al., 2022b), the use of unbleached pulp (i.e., containing residual lignin) offers a low-cost opportunity for nanomaterials production in addition to bringing new functionalities to the CNFs (Delgado-Aguilar et al., 2016; Osong et al., 2013). For instance, the presence of 2-3% of residual lignin from chemical pulping in the biomass has been suggested to improve the production yield and efficiency of the nanofibrils, hence lowering the overall cost of production compared to TEMPO oxidized-CNF (Delgado-Aguilar et al., 2016). Some studies suggest that residual lignin can potentialize defibrillation through radical scavenging (Solala et al., 2020) or as a viscosity control agent (Albornoz-Palma et al., 2023a). The presence of lignin has also shown promise in the development of advanced functional materials from CNFs, such as barrier films, emulsions and nanocomposites (Solala et al., 2020) owing to the addition of water barrier, UV-blocking, or antioxidant properties. For instance, LCNF films with lignin content higher than 4% have demonstrated excellent UV-blocking capabilities (Bian et al., 2021). Additionally, lignin's antioxidant properties add significant value to CNF-based materials, a study demonstrated that LCNF films exhibited

strong antioxidant activity, with up to 99% inhibition in the 2,2'-azino-bis(3-ethylbenzothiazoline-6-sulfonic acid (ABTS) (Rincón et al., 2023). Numerous studies have demonstrated that the presence of residual lignin significantly reduces the hydrophilicity of CNF, resulting in less polar LCNF, which decreases water absorption and permeability in nanopapers, especially when the lignin content exceeds 15% by weight (Najahi et al., 2023). Rojo et al. (2015) investigated LCNFs film properties with chemical delignification of Norway spruce resulting lignin contents ranging from 0 to 14%. The authors explained that lignin served as a natural adhesive, filling in the spaces among nanofibers, and leading to a smoother surface after hot-pressing. In terms of mechanical property, the tensile strength of these LCNF films with 4% of residual lignin was comparable to CNF, with values from 116 to 164 MPa; the researchers hypothesized that the presence of lignin had no negative impact on the strength (Rojo et al., 2015). In fact, some studies have reported even higher mechanical performance compared to neat CNF, after redistribution and hot-pressing of LCFN films (Jiang et al., 2020). Hence, there may be a misconception that presence of residual lignin in the films is going to overcome the properties of neat CNF films if no post treatment is applied.

However, the reported promising effects of lignin on the production and properties of LCNFs have not reached a consensus in the literature. The contradictory role of lignin has for instance been highlighted during pulp defibrillation for LCNF production. In addition to acting as a defibrillation facilitator, lignin can also act as a physical barrier (cementing effect) of pulp defibrillation, resulting in reduced LCNF yields and higher energy of production (Albornoz-Palma et al., 2020). Albornoz et al 2023 discovered that native lignin (> 25%), i.e., non-oxidized, in *Pinus radiata* hindered defibrillation during homogenization and produced larger and less flexible fibrils. The oxidized fibers with ~16% of lignin vs. ~10% lignin, produced

nanofibrils with diameters around 26 and 17 nm, respectively, while the non-oxidized let to diameter higher than 50 nm. Multiple studies also have highlighted that lignin would disrupt the hydrogen bonding among fibrils and decrease the performance of the films (Bian et al., 2018; Spence et al., 2010). For instance, fibers were chemically treated with acid maleic for lignin removal resulting in lignin contents ranging from 0.1 to 17.2%. The films with higher lignin content had specific Young's modulus of around 6 MN m/kg, while films with 3.9% and 0.1% of lignin had this value increased to around 9 and 11 MN m/kg, respectively (Bian et al., 2018). The influence of lignin on the barrier properties of LCNF films has also been a subject of investigation. Spence et al. (2011) obtained Water Vapor Transmission Rate (WVTR) values ranging between 220 to 460 g/m²·day containing different amounts residual lignin contents varying from 2.4% to 13.8%, respectively. These findings suggested that higher lignin content correlates with increased WVTR (Spence et al., 2010).

The variability in the performance of LCNFs can be attributed to differences in pulping chemistry (Albornoz-Palma et al., 2023b) and the origin and nature of the biomass (Jonasson et al., 2021), all of which affect the structure, chemistry, and functionality of lignin. Therefore, it is crucial to understand the role of biomass structure and composition in the production and performance of CNFs. One approach towards this goal is the use of genetic engineering to tune and tailor the chemical composition and structure of woody biomass. Peng et al 2023 produced Cellulose Nanocrystals (CNC) with of transgenic hybrid poplar by overexpressing the *Arabidopsis* gibberellin 20-oxidase1, an enzyme that acts in the biosynthesis of gibberellin (GA), an important hormone controlling plant growth and development. The engineered biomass led to thinner CNC with larger crystals (up to 100%) compared to the wildtype and increased mechanical performance when used as paper reinforcement (Peng et al., 2023).

Another approach explored the alignment of the fibrils into the cell wall of aspen trees, this was engineered by the reduced expression of cellulose synthase interactive 1 (CSII). The resulting CNF produced by genetic modification exhibited approximately 200% less water uptake, attributed to lower carboxylic content in the transgenic trees, and reduced tensile strength due to changes in the apparent nanofibril aspect ratio and surface accessibility, while demonstrating higher stiffness (5.6 GPa for the transgenic versus 4.6 GPa for the wildtype) (Jonasson et al., 2022).

In this work, we propose the use of CRISPR-edited poplar trees to understand how variations in biomass chemical composition influence the production and performance of LCNFs. Unlike previous studies that targeted a single gene, our approach utilizes multiplex CRISPR editing to simultaneously modify multiple genes. Specifically, the trees in our study were edited to target monolignol biosynthesis, enabling uniform genetic modifications within the same species (Sulis & Wang, 2020). The multiplex CRISPR approach in monolignol biosynthesis has the potential to significantly alter carbohydrate-to-lignin (C/L) ratios and lignin chemistry (i.e., syringyl/guaiacyl (S/G) ratios), with increases of up to 248% and 215%, respectively, without negatively impacting wood growth or strength. (Sulis et al., 2023). We selected four CRISPR-edited hardwood *P. trichocarpa*; all with a distinct carbohydrate-to-lignin ratio. Micro-kraft pulping was conducted on the wood species to extract the pulp and convert it to LCNFs. The influence of the biomass chemical composition on the production of LCNFs and their performance as self-standing films was investigated to shed light on the impact and importance of lignin's presence in the supply chain of cellulose nanofibrils

4.3. Experimental Section

4.3.1. Materials

For the chemical composition analysis of biomass and Kraft pulp sulfuric acid, 72% (w/w) Aqueous Solution (Ricca Chemical, USA) was used for hydrolysis and Calcium Carbonate CaCO_3 (Sigma-Aldrich, USA) was used for hydrolysate neutralization. The Enzymatic Hydrolysis utilized Cellulases (Cellic® CTec3) (Novozymes North America, Franklinton, NC, USA) and Hemicellulases (HTec3 NS 22244) (Novozymes) with activity of 190 FPU/g, and Sodium acetate (Spectrum, USA), Glacial acetic acid (Spectrum, USA) for the buffer solution at pH 5.0. Heteronuclear single quantum coherence (2D HSQC) nuclear magnetic resonance (NMR) spectroscopy Chloroform-d (Sigma-Aldrich), Pyridine-d (Sigma-Aldrich). For ^{31}P NMR spectroscopy it was used Chloroform-d (Sigma-Aldrich), Chromium (III) 2,4-pentanedionate (Alfa Aesar), Pyridine anhydrous (Sigma-Aldrich), 2-chloro-4,4,5,5-tetramethyl-1,3,2-dioxaphospholane, (TMDP) (Sigma-Aldrich), N-hydroxy-5-norbornene-2,3 dicarboxylic acid imide (NHND); 97% (Sigma-Aldrich).

4.3.2. Methods

4.3.3 Biomass feedstock: CRISPR Cas-edited and wildtype *P. trichocarpa* with a carbohydrate-to-lignin ratio (C/L) of (a) 2.9 (62.8% carbohydrates, 22.1% lignin), (b) CRISPR K3 with a C/L ratio of 2.8 (56.5% carbohydrates, 20.2% lignin), (c) CRISPR OKC with a C/L ratio of 2.8 (61.7% carbohydrates, 22.2% lignin), and (d) CRISPR OC5 with a C/L ratio of 4.3 (65.7% carbohydrates, 15.3% lignin) are analyzed in this work. The genetic modification of the lines target genes consisted in the loss-of-function edits in both alleles of PtrCAD1 gene, and loss-of-function edits in one allele of PtrC3H3 and PtrAldOMT2 genes in CRISPR K3.

While CRISPR OC5 had the loss-of-function edits in both alleles of: PtrPAL2, PtrPAL4, and PtrPAL5 genes. CRISPR OKC: Loss-of-function edits in both alleles of PtrCAD1 gene, and wildtype (control) None.

4.3.4. Micro Kraft pulping: The wood feedstock was converted into Kraft wood pulps using a Parr reactor Series 4700 with a volume of 45 mL. Debarked stems of transgenic and wildtype *P. trichocarpa* were cut into ~1.5 cm length and ~3 mm diameter, and for each pulping experiment, 4 g of oven-dried (O.D) wood chips was mixed with a Kraft pulping liquor, containing sodium hydroxide (NaOH) and sodium sulfide (Na₂S) at a liquid-to-solid ratio of 4:1. The active alkali utilized in this process had 16% with sulfidity of 25%. The pulping was performed at 165 °C for 2 h with vigorous manual shaking of the pressure vessel every 20 min. The pulp was removed from the pressure vessel and washed with distilled water at room temperature. The pulped wood was then disintegrated using a laboratory blender, filtered and thoroughly washed with distilled water.

4.4.5. Chemical composition analysis of biomass and pulps (Wet chemistry): The chemical composition of the four poplar woods before and after Kraft pulping, was determined by Klason lignin and High-Performance Liquid Chromatography (HPLC). Carbohydrates and lignin contents were quantified according to the Technical Report NREL/TP-510-42618- 2012 named “Determination of structural carbohydrates and lignin in biomass. In summary, the wood chips/pulp were digested in 72% sulfuric acid, and then diluted to solubilize and hydrolyze the carbohydrates. The chips/pulp were then filtered using Gooch Crucibles 30mm (KIMAX[®], USA) and the remaining insoluble residue, representing the acid-insoluble lignin

(AISL), was dried at 105°C in a vacuum oven (Symphony, VWR, YSA) and weighed using analytical balance (MS 104S, Mettler Toledo, Switzerland). The amount of acid-soluble lignin (ASL) from the pulp was estimated by UV-vis spectroscopy (Genesys 50, Thermo Fisher, USA), at a wavelength of 205 nm. After neutralization of the hydrolysate with CaO₃, the carbohydrates were quantified by (HPLC Agilent 1200, Agilent Technologies, USA) and reported as Glucose, and the sum of Galactose, Xylose, and Mannose as hemicelluloses.

4.4.6. Chemical analysis of biomass by 2D HSQC NMR: The chemical structure of the wood and its interunit linkages was analyzed by 2D HSQC NMR spectroscopy. The wood, extractive-free, was finely ground into 40-60 mesh particles using a Wiley mill (Thomas Scientific, USA) and subsequently freeze-dried at a pressure of 0.020 mbar for three (3) days (Labconco, USA). The resulting dry material was placed into a 5-mm NMR tube with 500 µL of a DMSO-d₆/Pyridine-d₅ mixture in a 4:1 (v/v) ratio. The wood particle suspensions were sonicated using an ultrasonic bath for 6 h, until formation of a uniform gel. The acquisition of the 2D HSQC spectra was carried out using a 700 MHz Avance NEO magnet system (Bruker, USA), equipped with a 5-mm Temperature Controlled Imaging (TCI) cryogenically cooled probe, using a pulse sequence hsqcetgpsisp.2. The spectra collection included 2,048 points along the F2 axis and 512 points along the F1 axis, with acquisition times set to 125 ms and 6.6 ms respectively, a delay time of 1 second, and a total of 32 scans. Spectra processing was performed using the Topspin software version 4.1.1. The S (syringyl), G (guaiacyl), and H (hydroxyphenyl) units were quantified by integration of the areas, to the sum of S, G, and H units equals to 100%. The quantification of interunit linkages was determined by integrating

the contours of the C α /H α signals, with the results expressed as the total sum of the levels of β -O-4', β -5', β - β ', and β -1' linkages (Balakshin et al., 2003; Sulis et al., 2023).

4.4.7 Determination of hydroxyl groups in Kraft pulps:

4.4.7.1. Lignin isolation in transgenic and wildtype kraft wood pulps for ^{31}P NMR spectroscopy: An enzymatic hydrolysis was conducted on the kraft wood pulps to isolate the lignin from the carbohydrates for lignin derivatization and quantification of chemical functionalities, but prior to LCNF production. A stock solution was prepared using an acetic acid/ sodium acetate buffer and a mix of enzymes. The total solids content of the stock solution was 5 wt.%, composed of cellulases (Cellic® CTec3) and hemicellulases (HTec3 NS 22244) in a ratio of 9:1 (g/g) (Otoupal et al., 2022). One gram of pulp was then diluted in 2.4 mL enzymatic stock, the volume was completed with the buffer solution until 40 mL. The hydrolysis was performed at 50 °C for 72 h in an incubator shaker (New Brunswick Scientific, USA), under continuous stirring at 150 rpm. After the enzymatic hydrolysis, the solution was washed with the buffer solution filtered in a fine crucible to collect the solids for further analysis.

4.4.7.2. Quantitative ^{31}P NMR spectroscopy: The lignin isolated by enzymatic hydrolysis of the wood kraft pulps was dissolved in a solvent mixture composed of pyridine/ CDCl_3 (1.6:1). ^{31}P -NMR analysis was conducted to determine the hydroxyl content following the reported methods by Argyropoulos, 1995; Meng et al., 2019. The prepared lignin solution was then placed into a 5-mm NMR tube, sealed and agitated manually prior to the NMR analysis. The spectra were acquired using an NMR spectrometer with a Quad probe (Bruker 500 MHz, USA). The

relaxation delay was set to 12 seconds and 10000 scans were acquired to ensure a high signal-to-noise ratio.

4.4.8. Determination of Kraft pulp Water Retention Value (WRV): The WRV of the Kraft Pulps was evaluated according to the TAPPI (UM 256, 1991) method. The pulp was diluted in water at 0.1 wt. % in a falcon tube, then it was filtered using crucible KIMAX 30 mm. The pulp was submitted with a centrifugal force of 900 rcf (3000 rpm) for 30 min (EPPERNDORF 5702, USA). The pulp is then air dried for 6 days. WRV was calculated using the formula: (weight after centrifuging (g) - O.D weight/ O.D weight (g). The tests were performed in triplicates.

4.4.9. Production of LCNF from the transgenic and wildtype poplar kraft pulps: An aqueous counter collision (ACC) (Sugino Machine Co., Ltd., Japan) equipped with a ball chamber and a 100- μ m nozzle was used to convert 0.36 wt% kraft pulps into LCNF suspensions. A pressure of 200 MPa was used to process the pulps through 7 successive passes. The mechanical energy per pass was measured using an energy meter Polaris 2500 - DAE P253-200-S KIT connected to the ACC. The energy consumption used for the production of LCNFs was calculated and reported in kWh per oven-dried mass (grams) of wood pulp.

4.4.10. Morphology of LCNF: Transmission electron microscopy (TEM) of the LCNF suspensions was conducted using a JEOL JEM 2100-Plus microscope (JEOL, USA). The LCNF was diluted to 0.0025wt% LCNF and dropped onto a Formvar/Carbon Cu grid. The excess liquid was wicked using a Whatman filter paper. The grids were then positively stained by using uranyl acetate at 2%. The images were taken at accelerating voltage of 80 kV and

× 20,000 magnification. A minimum of ten images were acquired for each LCNF grade, i.e., including the suspensions produced from the three CRISPR-edited and the wildtype poplar kraft pulps. The average widths of the LCNFs were estimated from the measurement of at least 80 fibrils on three different micrographs (per LCNF grade) using the software ImageJ. Analyses of variance (ANOVA) were conducted to compare results, at a threshold level of 0.05.

4.4.11. Preparation of LCNF films: The 0.1 wt.% LCNF suspensions were first dispersed using an Ultra Turrax (IKA® T-25, Germany) for 30 sec at 10000 rpm. The LCNF films were made by water evaporation of LCNF suspension poured in a polystyrene Petri dish of 8.5 cm in diameter. A film basis weight of 10 g/m² was targeted. The suspensions were dried at room temperature (25°C–30°C) under a fume hood, for approximately 4 days.

4.4.12. SEM- Cross section: Imaging of the cross-section of the films was conducted using a Field Emission –SEM (Verios 460, USA). Samples were cut with a razor blade and coated with a thin layer of gold (approx.7nm) prior to the cross-section analysis. The acceleration voltage was 2 kV, and the working distance was 6 mm. The images were acquired at magnifications ranging 2000×.

4.4. 13. Grammage: The grammage of the films were measured using a high precision balance and a micrometer (Lorentzen & Wettre, Stockholm, Sweden) area according to TAPPI 410 om -2008.

4.4.14. Density: The length and width were measured with a digital caliper to calculate the area. The density was calculated according to the following (Equation 1):

$$\text{Density} \left(\frac{g}{cm^3} \right) = \frac{\text{mass (g)}}{\text{film thickness (cm)} * \text{width (cm)} * \text{length (cm)}}$$

4.4.15. Mechanical performance of LCNF films in tensile mode: The films were cut into strips of 60 mm long and 15 mm wide using a razor blade. Each strip was clamped to a Universal Testing machine equipped with a 0.5 kN load cell (Instron, USA) for mechanical properties testing in tensile mode. A 40 mm gap was selected, and the tests were conducted at a constant rate of 2 mm/min. All the experiments were conducted at 23 °C and 50 % RH. At least 5 strips per specimen were tested to ensure reproducibility of the experiments. Tensile index values were calculated with the maximum load before rupture and normalized by their respective grammages. The Specific Young's modulus was determined by the slope from the initial elastic region (stress - strain curve) and divided by the density of the films.

4.4.16. Water vapor transmission rate (WVTR): The WVTR of the LCNF films was measured as reported in the ASTM E96 standard, at a controlled temperature of 23 °C and RH of 50%. In brief, each 8-cm in diameter film was sealed between the lid and the base of an aluminum cup (Model 68-3000 EZ-Cup, Vapometer, USA) containing 5 g of anhydrous CaCl₂ so as to keep a film's surface area of 0.003318 m² exposed to the environment for moisture transfer. Every hour, during a total of 8h, the change in mass was recorded using a high-precision laboratory balance. Each experiment was replicated in duplicates. The WVTR was calculated as follows (Equation 2):

$$WVTR \left(\frac{g}{m^2s} \right) = \frac{\Delta Mass (g)}{Surface Area of the film (m^2) * time (s)}$$

Water vapor permeability (WVP) was calculated multiplying the WVTR and the thickness of the film in μm and divided by the pressure (Equation 3). The pressure is the saturated pressure of water vapor (Pa) at the relative humidity of 50% RH.

$$WVP \left(\frac{g}{Pa * s * m} \right) = \frac{Thickness * WVTR}{Pressure}$$

ANOVA tests were conducted to WVTR and WVP to compare results, at a threshold level of 0.05.

4.5. Results and Discussion

4.5.1. Chemical structural alterations in transgenic poplars

Three CRISPR-edited and one wildtype juvenile poplar trees were selected as feedstocks for LCNF production. The multiplex CRISPR editing method targets the monolignol biosynthesis pathway (Sulis et al., 2023) tailoring lignin contents and its chemical structure. **Table 4.1** shows the chemical composition of the four wood specimens, prior to pulping. Differences in lignin's chemical structure between the four poplar trees were investigated by HSQC NMR and are also listed in Table 4.1.

Table 4.1 Main components of biomass (cellulose, hemicelluloses, and total lignin) and Lignin composition (%) for syringyl (S) and guaiacyl (G) units and interunit linkages of wildtype and CRISPR edited hardwoods (HW).

	Main components of biomass					Lignin Subunits *			Lignin interunit linkages*		
	Cellulose	Hemi-celluloses	Carbo-hydrates	Total lignin	C/L	Aromatic region ($\delta C/\delta H$ 150-90/8.0-6.0)			Aliphatic oxygenated side chain ($\delta C/\delta H$ 90-40/6.0-2.5)		
						S	G	S/G	A α	B α	C α
HW	(%)					S	G	S/G	A α	B α	C α
<i>Wildtype</i>	42.2	20.6	62.8	22	2.9	66.08	32.61	2.03	82.54	3.20	11.75
<i>CRISPR OC5</i>	46.5	19.2	65.7	15.2	4.8	72.95	24.78	2.94	86.61	2.44	9.33
<i>CRISPR OKC</i>	39.8	21.8	61.6	22.1	2.8	57.25	41.14	1.39	90.24	2.57	5.65
<i>CRISPR K3</i>	40.4	16.2	56.6	20.2	2.8	58.75	38.79	1.51	93.89	1.40	3.05

C/L: Carbohydrate to lignin ratio, where carbohydrates is the sum of cellulose and hemicelluloses

*%: percentage volume of total lignin

S: Syringil; G: Guaiacyl, A α : β -aryl ether (β -O-4); B α : phenylcoumaran (β -5); C α : resinol.

In this work, we selected three juvenile (6 months) CRISPR hardwoods with different carbohydrate-to-lignin ratios. Specifically, CRISPR OC5 exhibited the most pronounced changes with a higher cellulose content (46.5%) and lower lignin content (15.2%), resulting in a C/L ratio of 4.8 compared to the wildtype's 2.9. While CRISPR, OKC and K3, showed less pronounced changes, with both maintaining a C/L ratio of 2.8 similar to the wildtype, with slight variations in cellulose, and CRISPR K3 presenting the lowest hemicellulose content (Table 1). Compared to mature *Populus trichocarpa* hardwoods that have a typical composition of 24.6% lignin and carbohydrates 75.4% (Cao et al., 2012) the juvenile poplar trees presented lower lignin and carbohydrate content that yet align with reported ratios for chemical compositions for poplar trees of 2.5 to 7 years old (Krutul et al., 2019).

Regarding the lignin structure, our findings showed varied S/G ratios and β -O-4 contents across wildtype and CRISPR-modified poplar biomasses. CRISPR OC5 exhibits a higher S/G ratio of 2.94 with 86.61% of β -O-4 linkages, the values are similar to for other transgenic poplar that used similar editing (J. P. Wang et al., 2018). However, CRISPR OKC and K3, presented lower S/G ratios of 1.39 and 1.51 respectively, demonstrated unexpectedly high β -O-4 contents of 90.24% and 93.89%. Previous studies indicated that a higher (S/G) ratio typically correlates and the increased β -O-4 (Santos et al., 2012). However, such correlations were not observed for the three studied CRISPR biomasses. Furthermore, in **Figure 4.1** the presence of 2-methoxybenzaldehyde peaks at \sim 188 ppm for CRISPR OKC and K3 is observed, whereas these peaks are not present in the Wildtype and CRISPR OC5. The genetic modification might have led to accumulation of aldehydes that could copolymerize with normal lignin monomers, as observed in previous research (Ralph et al., 1997).

Understanding the origin of the aldehyde is beyond the scope of this work but is crucial for future research, as it may be affected by Kraft pulping and subsequently alter the chemical composition of the pulps. With such differences in chemical composition, we expect to produce LCNFs with distinct properties. Ultimately, analyzing the pulping step is crucial, as kraft pulping is known to primarily act on the lignin (Adler, 1977).

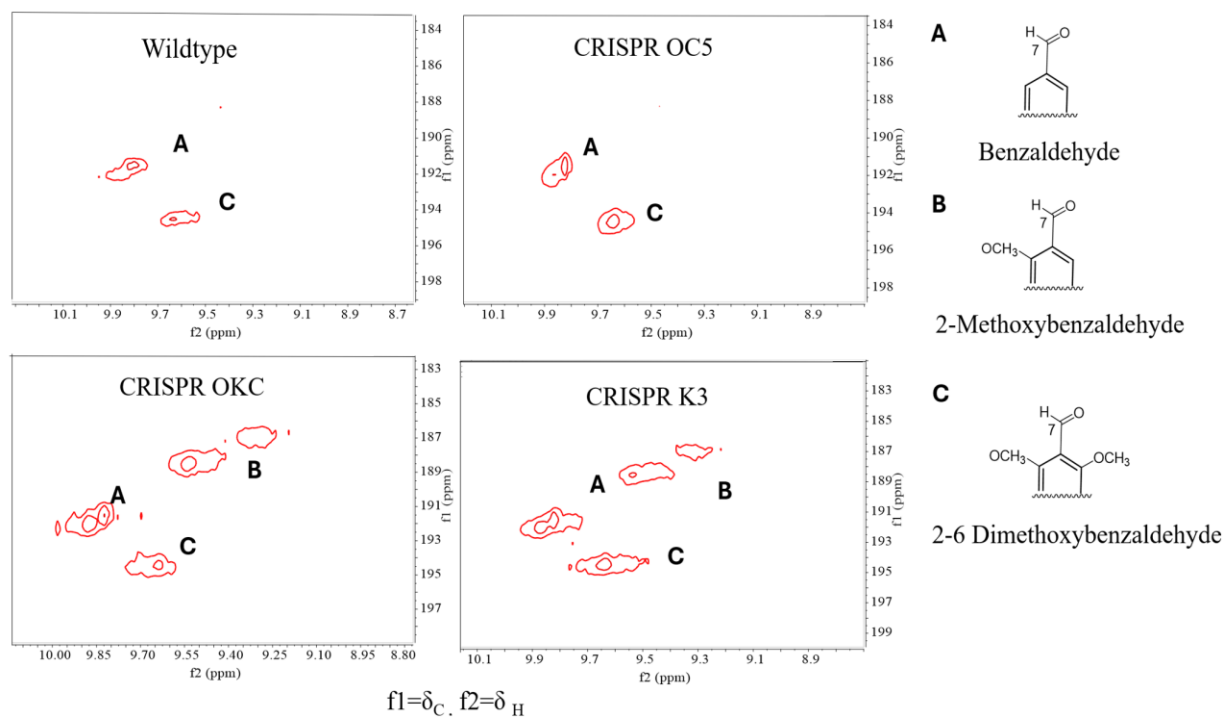


Figure 4.1 HSQC cross-signals of lignin Wildtype, CRISPR OC5, CRISPR OKC, and CRISPR K3. On the right it is represented the respective structures of the spectra A) Benzaldehyde, B) 2-methoxybenzaldehyde; C) 2-6 dimethoxybenzaldehyde.

4.5.2. Kraft pulping

The Kraft pulping process is the most dominant lignocellulose pulping process in the pulp and paper industry (Ahmad & Pant, 2018). The composition of biomass is subjected to significant changes during Kraft pulping. Parameters that influence the reactivity of lignin during pulping include the type and number of functional groups of syringyl and guaiacyl, the nature of lignin's linkages, molecular weight, and degree of polymerization (Santos et al., 2012). In this work, Kraft pulping of the four selected hardwoods was conducted using similar industrial conditions, with a liquid-to-pulp ratio of 4:1, active alkali 16% and sulfidity of 25%. **Figure 4.2.** presents the relative chemical composition of the Kraft pulps, C/L and their respective yields.

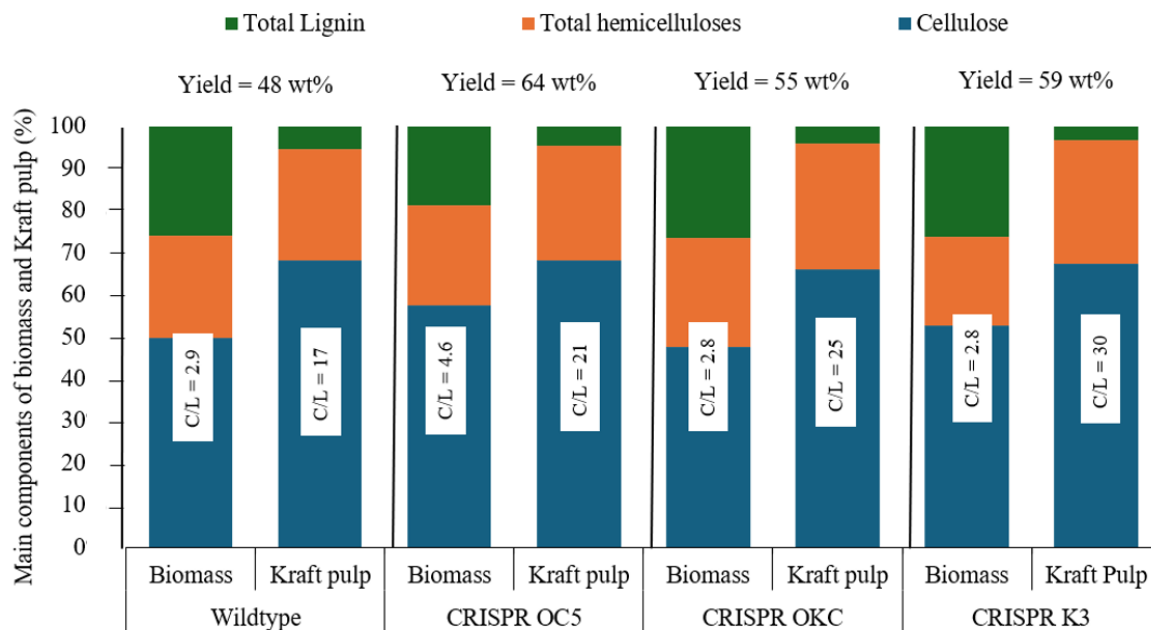


Figure 4.2 Pulping yields, Carbohydrates to lignin ratio (C/L), relative chemical composition of the Kraft pulps (does not include extractives, ashes and Hexenuronic acids) from the CRISPR-edited and wildtype poplar trees. Note: Total hemicelluloses include: Xylose, Mannose, Galactose and Arabinose.

Kraft pulping of the wildtype poplars led to a pulping yield of ca. 48%, which aligns with the reported values in the literature (Ribeiro et al., 2019). Typically, Kraft pulping yields are expected to range from 45 to 55% for poplar hardwoods (Labosky et al., 1983). Interestingly, much higher pulping yields (>55%) were obtained for the three CRISPR trees, demonstrating the effectiveness of the multiplex CRISPR editing approach. The increase in yields, and in turn the removal of lignin with resulting higher C/L ratios was notably significant for the CRISPR K3 and OKC hardwoods and may be explained by the higher number of ether linkages found in their respective lignin (above 90 % for CRISPR OKC and K3, vs. 82.56% for wildtype, **Table 4.1**) and the reduced amount of recalcitrant interunit linkages (below 3% for CRISPR OKC and K3 vs. 11.75% for wildtype, **Table 4.1**).

The amount of lignin in the wildtype Kraft pulp (4.5%), falls within the range of Kraft pulping of hardwood under similar conditions, which expects around 4% residual lignin content after pulping. (Ribeiro et al., 2019) CRISPR OC5 with 4% of residual lignin also follows this trend. However, lower amount of residual lignin is found for CRISPR OKC (3.3%) and K3 (2.7%) This might also be a reflection of the predominant amount of ether linkage in those samples. During the Kraft chemical pulping ether β -O-4 bonds are the most susceptible to cleavage, making them a primary focus of this type of pulping process. In contrast, carbon-carbon bonds, particularly the 5–5 biphenyl bonds involving the C-5 aromatic position, and resinol substructures with C–C bonds are resistant to alkaline process (Figure 4) (Adler, 1977). Moreover, during this process the concentration of carbohydrates, specifically cellulose, is preserved, while hemicelluloses are partially degraded (Gierer, 1980).

Overall, the enhanced performance is attributed to structural modifications in the lignin of CRISPR trees, including higher ether linkage content and lower recalcitrant interunit linkages, making their lignin more susceptible to cleavage during the pulping process. These modifications result in higher yields and lower kappa numbers, demonstrating the effectiveness of the CRISPR approach in improving pulping efficiency.

4.5.3 Impact of Chemical Composition on Lignin-Containing Cellulose Nanofibrils (LCNFs) from Wildtype and CRISPR-Edited Kraft Pulps

The four Kraft pulps were submitted to a high shear treatment using an aqueous counter collision (ACC) connected to a power meter to measure the energy consumption upon processing and production of LCNFs. In general, effective fibrillation and individualization of the biomass is characterized by LCNFs of small diameters and high aspect ratios. In turn, high

aspect ratio LCNFs are expected to result in self-standing films of higher mechanical performance than films made of low aspect ratio LCNFs (Karande et al., 2013). However, to achieve effective fibrillation and individualized LCNFs, a considerable amount of mechanical energy is commonly required if no chemical, mechanical or enzymatic pre-treatment is applied to the pulp prior to the high shear mechanical treatment (Malucelli et al., 2019) (X. Liu et al., 2018) . In this study, no pretreatments were carried out as we aimed to understand how variations in biomass chemical composition influence its processing into LCNFs. More specifically, we aimed to decipher the role of residual lignin in the defibrillation of pulp fibers to shed light on the previously discussed controversy. **Figure 4.3** represents the specific energy consumption to produce LCNFs from wildtype and CRISPR poplar Kraft pulps in kWh per kg of oven dried (OD) pulp in function of lignin and hemicellulose, and their respective fibrils morphology.

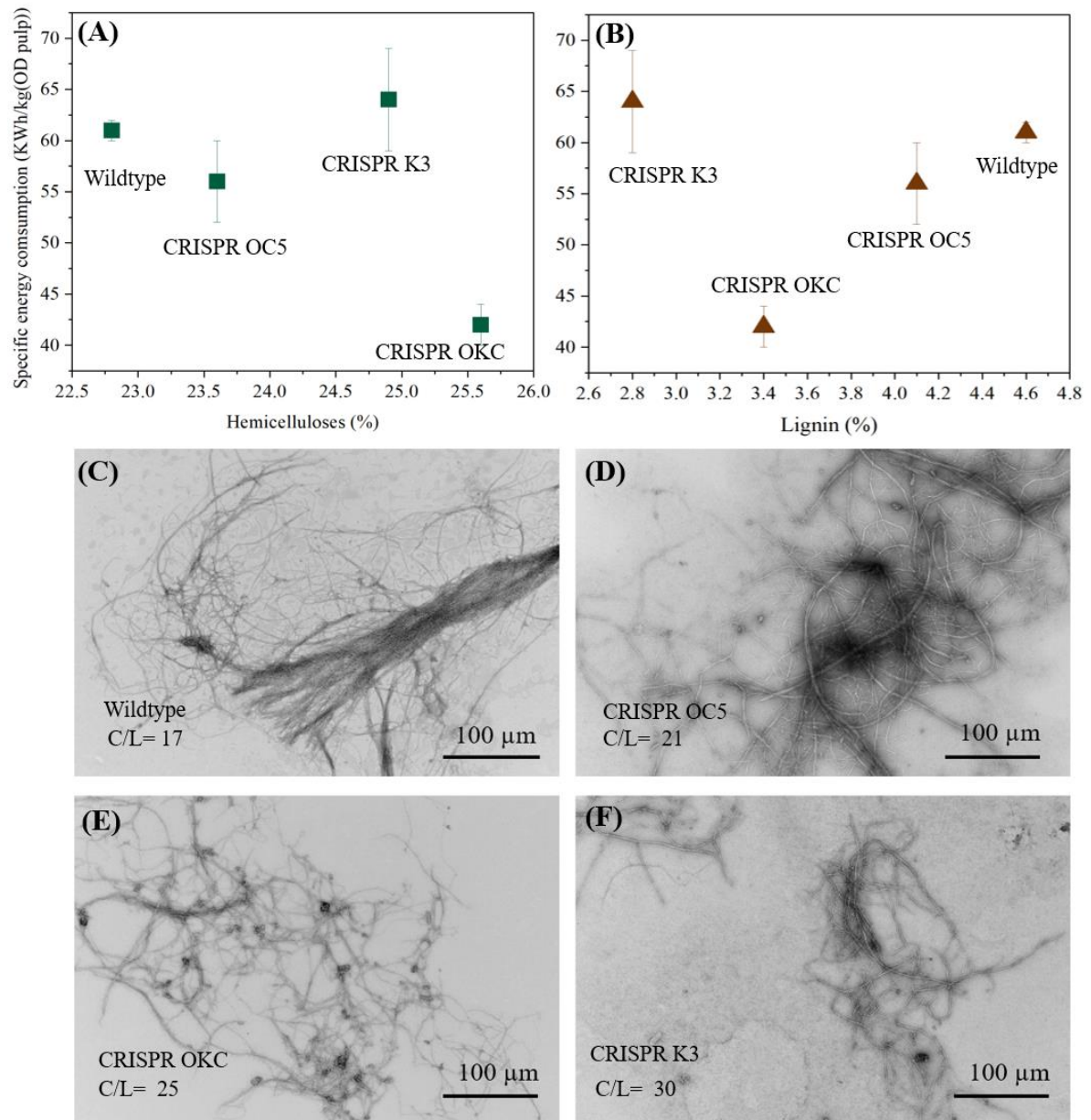


Figure 4.3 Specific energy consumption to produce LCNFs from wildtype and CRISPR poplar kraft pulps in kWh per kg of oven dried (OD) Kraft pulp as a function of (A) hemicellulose and (B) lignin contents of the Kraft pulps. Transmission Electron Microscopy images of LCNFs from (C) wildtype kraft pulps and CRISPR-edited poplars (D) OC5, (E) OKC and (F) K3 . C/L is the carbohydrate-to-lignin ratio of the pulps calculated from Figure

Figure 4.3A and B show the mechanical energy needed to defibrillate each of the four Kraft pulps as a function of their chemical composition, specifically of the hemicelluloses and lignin contents. Overall, it is observed that specific energy consumption remains very similar for wildtype, CRISPR OC5, and K3, and within the presented range is independent of hemicelluloses and lignin contents. Especially, wildtype and CRISPR OCS pulps exhibit similar lignin and hemicelluloses contents and energy consumptions of 56 ± 4 and 61 ± 0 KWh/kg (OD pulp) respectively. In contrast, CRISPR OKC and CRISPR K3, despite having similar lignin and hemicellulose contents, show different energy demands of 63 ± 7 and 42 ± 2 KWh/kg (OD pulp) respectively. Notably, CRISPR OKC achieved an impressive energy saving of approximately 25% compared to the wildtype. Our results diverged from previous research, which suggests that a higher hemicellulose content in wood pulp leads to an increased CNF yield and a reduced energy consumption (Chaker et al., 2013; Malucelli et al., 2019). Hemicelluloses typically act as a protective colloid, shielding cellulose fibrils from and impeding the formation of irreversible hydrogen bonds between them (Djafari Petroudy et al., 2021). The presence of CRISPR OKC as an outlier may be attributed to differences in lignin content and structure, which could explain the observed divergence. Further investigation into the lignin content and its structural properties might provide insights into this anomaly.

Figure 4.3 (C-F) shows the TEM images of the produced LCNFs. Overall, pulps with higher C/L led thinner LCNFs (OKC and K3). Moreover, fibril clusters were observed in the wild type and OCS LCNFs, indicating potentially less effective or incomplete fibrillation compared to OKC and K3 fibers.

Effective fibrillation and individualization of the biomass generally result in LCNF with small diameters and high aspect ratios, and it is expected that higher energy consumption will produce LCNFs with thinner diameters. Both the wildtype and CRISPR OC5 LCNFs (**Fig 4.3 C and D**) exhibit a similar average fibril diameter of ~34 nm. The CRISPR OKC and K3 LCNFs show overall thinner fibrils of 16 ± 5 nm and 25 ± 7 nm in diameter, respectively (**Fig 4.3 E and F**). The higher residual lignin content (4.5-4.0%) in the wildtype and OC5 pulps may explain the larger fibril diameters as a higher content of lignin may have inhibited the individualization of fibrils (Spence et al., 2010). Similarly, the CRISPR OKC and K3 pulps of lower lignin content (3.4 and 2.7%, respectively) led to LCNFs of much smaller diameters. The study by Albornoz-Palma et al. (2023) supports these observations: the presence of 6.9% of residual lignin and 25.5% of hemicelluloses in their pulp led to LCNFs with greater fibril flexibility, higher specific surface area ($106 \text{ m}^2/\text{g}$), and smaller widths (25 nm) than LCNF with 8.5% of lignin and 25% of hemicelluloses with widths around 33 nm and specific surface area of $85 \text{ m}^2/\text{g}$ (Albornoz-Palma et al., 2023b).

While the lignin content in the pulp can explain the variations in LCNFs' diameters, it still does not explain the divergence in energy consumption between the CRISPR OKC and K3 specimens. Such a divergence in energy consumption also challenges a common paradigm in the field that presumes that a high energy consumption leads to more effective fibrils' individualization, and in turn, production of thin(ner) CNFs (Karande et al., 2013).

Hence, the results shown **Figure 4.3** strongly suggest that there is more to the role of lignin than its content in the pulp, to explain the production efficiency of LCNFs and their performance.

4.5.4. Performance of LCNF films

An indirect approach to assess the fibrillation and performance of LCNFs is the study of their films' properties (Spence et al., 2010). LCNF films were made by water evaporation with a target basis weight of 10 g/m². Their cross-sections are shown in **Figure 4.4**.

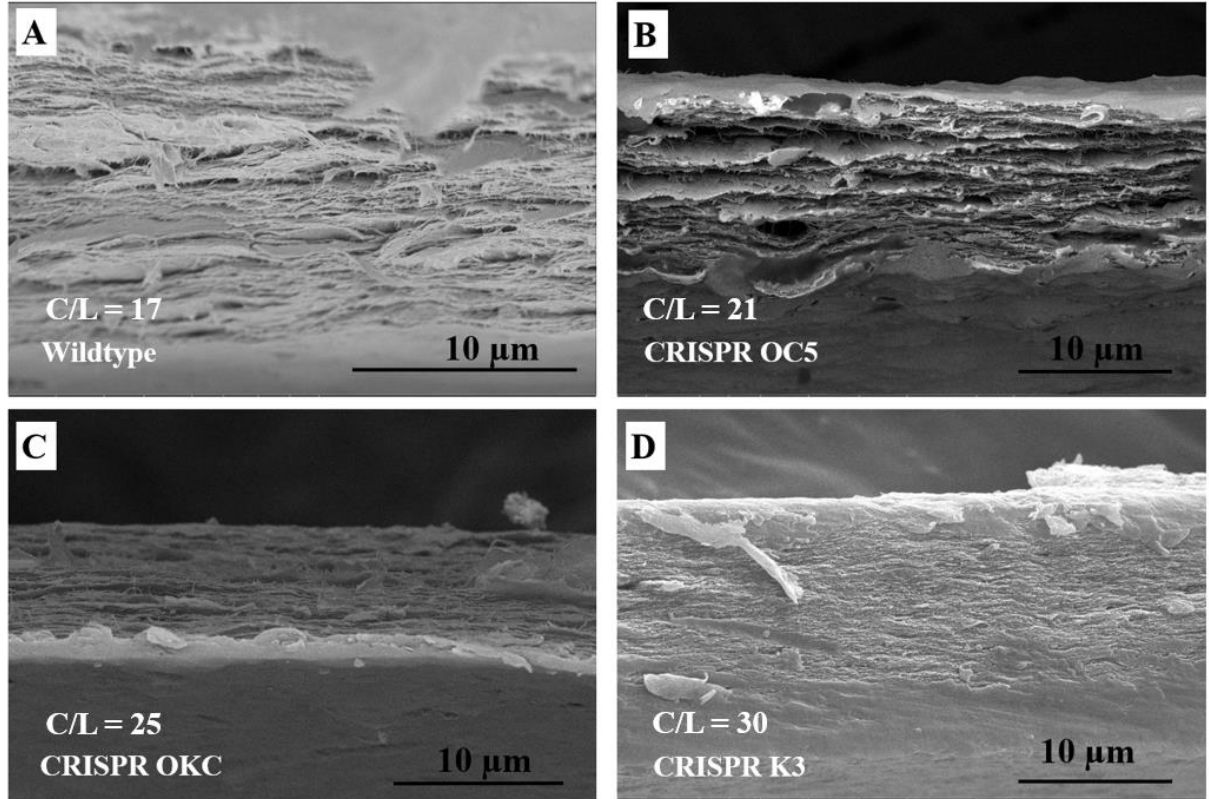


Figure 4.4 Scanning Electron Microscopy (SEM) images of the cross section of films made from (A) Wildtype, (B) CRISPR OC5, (C) CRISPR K3, and (D) CRISPR OKC LCNFs

The LCNF films' cross sections exhibit a layered structure, possible due to sample preparation. This morphology is commonly observed in CNF films produced by casting (Aulin et al., 2009; Hasan et al., 2021), and can be consequence of the random orientation distribution of the fibrils during the air-drying (Svagan et al., 2007).

However, the CRISPR K3 and CRISPR OKC films presented a more compact, denser structure, which was also reflected by their slightly higher density (**Table 4.2**). The increased density and compactness observed in CRISPR K3 and CRISPR OKC films may be attributed to a higher hemicellulose content. Previous research suggested that an increased amount of hemicelluloses (about 10%) contributed to a denser matrix by enhancing intermolecular bonding and diminishing pores and voids in films (Yu et al., 2019). Although the hemicellulose content in this research shows a small increase of approximately 3% between the wildtype and CRISPR OKC and K3, this increase, along with the higher C/L ratios, in turn reduced lignin, of 25 and 30 for CRISPR OKC and K3, respectively, compared to 17 and 21 for the wildtype and OC5, might be sufficient to enhance the cohesive forces between the fibrils.

Table 4.2 Structural and mechanical properties of LCNF films from wildtype and CRISPR-edited hardwoods

LCNF films	Density	Porosity	Specific Young's modulus	Tensile Index
	g/cm ³	(%)	MNm/ kg	Nm/g
Wildtype	0.8 ± 0.05 ^b	48 ± 3	6.5 ± 2	58 ± 8
CRISPR OC5	0.9 ± 0.09 ^{a,b}	35 ± 6	9.3 ± 1	55 ± 8
CRISPR OKC	1.1 ± 0.07 ^a	23 ± 5	12.5 ± 3	85 ± 9
CRISPR K3	1.0 ± 0.08 ^a	28 ± 5	11.8 ± 1	64 ± 9

^{a-b} Values that do not share a letter are statistically different from one another (p > 0.05

level, t-test)

Table 4.2 summarizes the main mechanical performance of the LCNF films, namely their specific Young's modulus and tensile index. Both the Young's modulus and tensile

strength values were normalized by the basis weight of the films for direct comparison of their performance.

All the CRISPR LCNF films perform better than the wildtype LCNF films. Specifically, the CRISPR OKC and K3 films show much higher Young's modulus and tensile strength than the two other specimens (i.e., the wildtype and CRISPR OC5 films). Once again, these two CRISPR specimens show similarities in performance and distinguish themselves strongly from the two other studied woods. The higher hemicellulose content in CRISPR OKC and K3 pulp, 25.7 and 24.9%, respectively, up to 3% higher compared to wildtype and 2% OC5, as well as the thinner diameters of the LCNFs can potentially explain the highest mechanical performance of the CRISPR OKC and K3 films (Chaker et al., 2013b). The juvenile trees in this work have these increase in mechanical performance potentialized (about 40%) by a small increment in the hemicellulose content but yet in agreement with literature that considered that addition of only 5% to the total hemicellulose content (22 vs. 27%) could promote adhesion between CNFs and contribute to the improvement of the films' mechanical strength in approximately 10% (Iwamoto et al., 2008).

In contrast, the wildtype and CRISPR OC5 films presented lower performance, because of their lower hemicellulose content (22.8 and 23.6%), higher lignin content (4.5 and 4.0%) compared to CRISPR OKC and K3, with 2.7 and 3.3 %, and larger fibrils diameters. This is in agreement with previous study, which has reported that a high lignin content from unbleached LCNF (3.9 %) can hinder hydrogen bonding between the CNFs, and in turn reduce the tensile strength about 27% of CNF films compared to bleached CNFs (< 0.5 % lignin) (Bian et al., 2018). Our results conclude that the mechanical performance is indeed promoted by a balance between the hemicelluloses and the lignin.

Overall, the mechanical performance of the wildtype and CRISPR LCNF films studied in this study remains lower than the performance reported in the literature. For instance, Spence et al 2010 measured a tensile index of Unbleached Kraft hardwood (UBHW) LCNF films with 2.4% of lignin, and Hemicelluloses around 20%. The LCNF films resulted in Tensile index higher than 100 Nm/g (Spence et al., 2010). While the impact of residual lignin and hemicelluloses on LCNF films' mechanical properties has been discussed and reported extensively in the literature, the concept of “high content for hardwood Kraft pulp” of lignin/hemicelluloses has yet to be defined.

The differences in the low values mechanical performance when compared to the literature, can be explained by the maturity level of the harvested trees, as we studied juvenile hardwood poplars of 6 months old. Juvenile woods are typically characterized by lower mechanical performance than mature woods (Adamopoulos et al., 2007). Studies have shown that mechanical properties improve greatly with age; for example, the modulus of elasticity in loblolly pine more than doubles from early juvenile wood (1 year) to late mature wood (12 years), along with improvements in fiber length and fibril angle, which are crucial for mechanical performance (Bendtsen & Senft, 1986). Moreover, the trees age likely contributes to the fact that every small improvement or damage can be more easily observed in the material, as it is not mature and thus not as strong.

The water vapor transmission rate (WVTR) also provides insights on how the chemical composition of biomass influences the performance of LCNFs films. Literature has demonstrated that the moisture barrier properties of LCNFs can be significantly affected by the degree of fibrillation (Nakagaito & Yano, 2004) and the chemical composition of the nanofibrils (Spence et al., 2010).

Figure 4.5 presents the water vapor transmission rate values of the wildtype and CRISPR LCNF films.

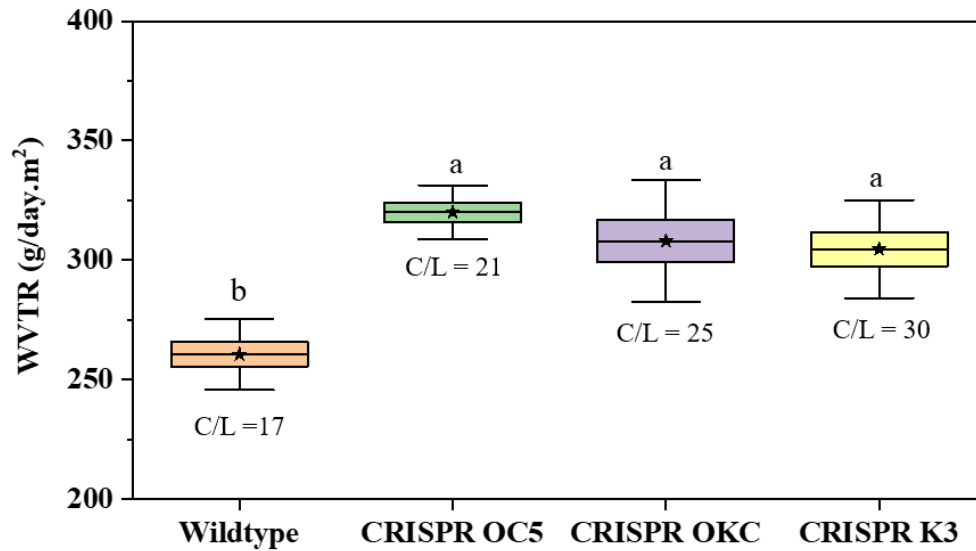


Figure 4.5 Water vapor transmission rate values of wildtype and CRISPR LCNF films, and carbohydrates to lignin ratio (C/L). ^{a-b} Values that do not share a letter are statistically different from one another ($p > 0.05$ level, one sample t-test).

In **Figure 4.5**, the LCNF wildtype film exhibited the lowest WVTR at approximately 260 g/m²·day, while the CRISPR films showed slightly higher values around 300 g/m²·day. These values are consistent with previous studies, which report WVTR values starting from 220 g/m²·day for LCNF produced from unbleached Kraft pulp hardwood with a similar chemical composition to this study (Spence et al., 2010). This suggests that the age of the trees does not affect the barrier performance as significantly as it affects the mechanical properties. Compared to the wildtype, all the CRISPR LCNF films, which had an increased C/L ratio, exhibited increased WVTR. Contrary to expectations that the increased lignin content would disrupt the film's network and facilitate vapor diffusion (Spence et al., 2010), this study did not observe such a direct correlation. Instead, it suggests that the increased carbohydrate content

in the CRISPR LCNF films, along with a higher degree of defibrillation, has led to an increased WVTR. This increased water affinity was also observed by Nakagaito and Yano (2004), who showed that the water retention of CNF increased with an increasing degree of fibrillation due to greater exposure of hydrophilic surface sites (Nakagaito & Yano, 2004).

Despite the variations in LCNF morphologies, film cross-sections, and pulp chemical compositions, these differences do not translate into significant variations in WVTR within the CRISPR LCNFs. This suggests that there is not a linear correlation between the chemical composition (C/L) and WVTR of CRISPR LCNF films. Moreover, contrary to the behavior observed to the mechanical properties, the WVTR of CRISPR OC5 is more similar to CRISPR OKC and K3 than to the wildtype. Factors contributing to the similar WVTR might include similarities in film density and porosity, as shown in **Table 4.2**. Although CRISPR OKC and K3 have higher C/L ratios compared to OC5, the leveling of WVTR could also be influenced by the enhanced interactions between lignin and cellulose, leading to a better inter-fibril interaction and reducing the vapor diffusion in the films, as observed in previous works. (Bian et al., 2018; W. Wang et al., 2019).

4.5.5. How to explain similarities between CRISPR OKC and K3?

The LCNFs and LCNF films from CRISPR OKC and K3 show strong similarities in morphologies, structure and overall performance; yet the CRISPR OKC LCNFs were produced with 25% less mechanical energy as the CRISPR K3 LCNFs. It is generally it is assumed that effective defibrillation demands a high energy, especially during high-shear treatment aimed at maximizing defibrillation (Karande et al., 2013), this limits commercialization of CNFs due to costs increase (Djafari Petroudy et al., 2021). Our results show a promising alternative to

overcome this barrier, since LCNFs with high mechanical performance were produced with lower energy .

Because of the nature of the multiplex CRISPR editing approach, it seems relevant to further understand the differences in lignin structure between the two CRISPR specimens as well as the interaction between lignin and carbohydrates in the pulps. We measured the water retention values (WRV) of the pulps as an indirect approach to understand how easy the defibrillation from Krat pulp to LCNF can occur. WRV indicates the extent to which fibers can swell in water. The swelling effects can alleviate the complex and resistant nature forces of the plant cell wall, thereby facilitating the nanofibrillation of lignocellulose fibers (Shen et al., 2023). The WRV of the pulps as a function of their lignin and hemicellulose content is plotted **Figure 4.6**.

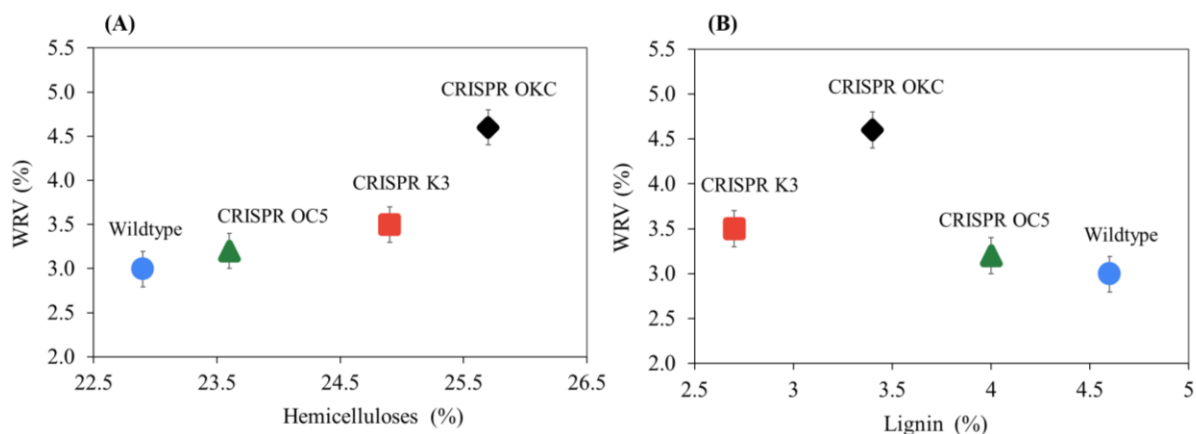


Figure 4.6 Water retention values of wildtype and CRISPR Kraft pulps as a function of (A) Hemicelluloses (B) Lignin

In **Figure 6A** an increase in the swelling is observed with the increase of hemicelluloses, which was more pronounced in the CRISPR variants. Hemicelluloses have been shown to inhibit the hornification effect and enhance the pulp's water retention values (Rebuzzi & Evtuguin, 2005). The presence of these polysaccharides in the pulp contributes to enhanced

fibrillation due to the carboxylic groups, which increase interfibrillar repulsive forces and consequently weaken the interfibrillar hydrogen bonds in water (Iwamoto et al., 2008).

The increased amount the amount of lignin led to lower WRV for wildtype, CRISPR OC5 and K3 (**Figure 4.6B**). A high amount of lignin can be considered a physical obstacle to the efficient production of LCNFs. This effect is due to hydrophobic networks which reduce fiber swelling (Lahtinen et al., 2014). However, CRISPR variants with similar lignin contents—such as OKC and K3—do not demonstrate a correlation with the WVR. Interestingly, while the chemical composition of these two samples is very similar, the CRISPR OKC resulted an expressively increase in WRV, and a significant reduction in energy consumption by 25%. This suggests variations in the chemical structure of residual lignin for CRISPR OKC may influenced the defibrillation efficiency. Jiang et al. (2018) suggested that residual lignin from chemically treated pulps could in fact increase the yield of LCNFs with smaller diameters, reduced polarity, and higher hydrophobicity. In this study, we hypothesize that higher oxidation levels, i.e. higher lignin removal after pulping, expose more the carbohydrates and increased its ability to swell. This, in turn, reduces the energy consumption for defibrillation. This effect would be potentialized by the newly generated chemical groups on lignin after Kraft pulp. To confirm this hypothesis, the residual lignin chemistry of CRISPR OKC and wildtype are studied.

Determination of pulp hydroxyl group of CRISPR OKC

After the biomass is submitted to Kraft Pulp, the pulp is enzymatic hydrolyzed for removal of carbohydrates and then the residual lignin is analyzed by ^{31}P NMR. The amount of hydroxyl groups (-OH), particularly phenolic-hydroxyls, along with the carboxylic groups

are the most important parameters in lignin because it is an indicator of lignin reactivity (Jardim et al., 2020) and can give insights into LCNF defibrillation. The carboxylic acid, aliphatic OH, phenolic OH content of the residual lignin is depicted in **Figure 8**. The quantification of the groups is plotted based on the condensed phenolic total phenolics and carboxylic groups.

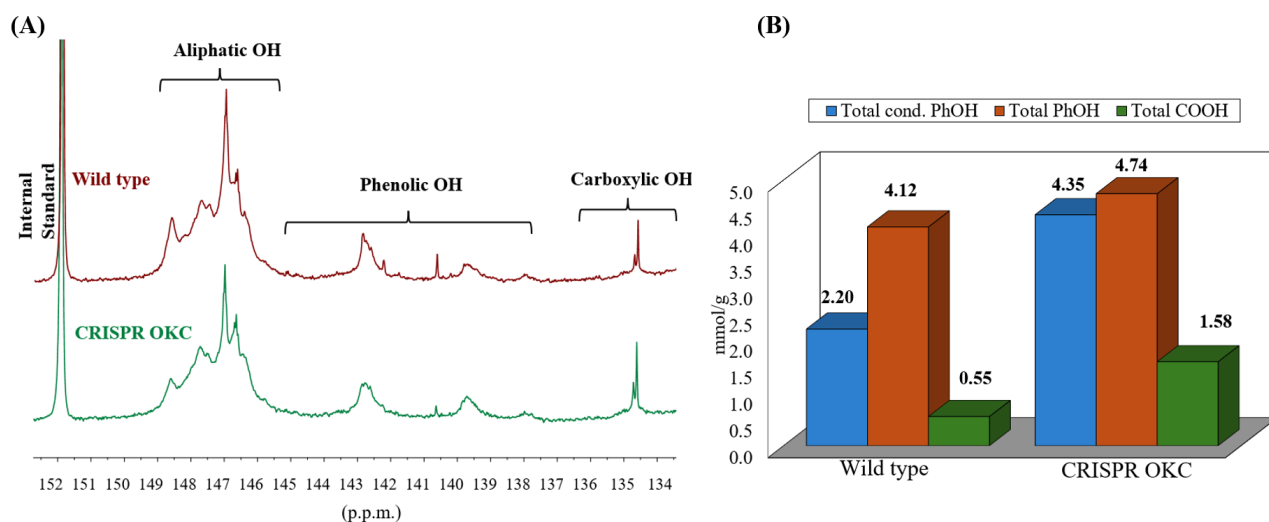


Figure 4.7 (A) ³¹P NMR spectra of OH groups in lignin of the wildtype and CRISPR OKC sample (B) Quantitative analysis of wildtype and CRISPR OKC. The y-axis indicates the amount of group (in mmol/g). The bar column represents the condensed phenolic OH (Con. Phenolic OH) shown in blue, total phenolic OH (Total PhOH) in orange, and total carboxylic OH (Total COOH) in green.

Figure 4.7A shows the typical lignin species, highlighted by the aliphatic OH, phenolic OH, and carboxylic OH groups. In **Figure 4.7B**, the data quantifies these groups according to the lignin derivatization method described in the the protocol outlined by Meng et al., 2019. The results highlight that the wildtype shows condensed phenolic OH at 2.20 mmol/g, total phenolic OH at 4.12 mmol/g, and total carboxylic OH at 0.55 mmol/g. Conversely, the CRISPR OKC variant exhibits significantly different values with increased condensed

phenolic OH at 4.35 mmol/g, total phenolic OH at 4.74 mmol/g, and total carboxylic OH at 1.58 mmol/g. These observations suggest that the increased concentrations of these groups in CRISPR OKC are related to more reactive and efficient lignin removal from the pulp, as previously described by Froass et al., (1996). This is corroborated by the reduced percentage of residual lignin given by the chemical composition analysis ($3.3 \pm 0.2\%$ in OKC versus $4.5 \pm 0.3\%$ in the wild type). Moreover, the pronounced amount of carboxyl groups, could be potentially incremented by chemical pulping reactions with newly aldehydes groups evidenced HSQC (**Figure 4.1**). This increase in carboxyl groups likely contributed to the increased swelling degree of fiber (Scallan & Grignon, 1979), as observed in **Figure 4.6**, and the associated decrease in energy consumption.

Conclusion

To produce highly defibrillated LCNFs, breaking the native lignin network structure is essential, typically requiring delignification before defibrillation. It is important to consider in this process the amount and chemical structure of the lignin. Chemical pulping results in the oxidation of lignin, which uncovers more cellulose and hemicellulose surfaces resulting in higher C/L ratios. This increased exposure introduces a higher number of total polar groups, thereby increasing the polarity of LCNF. Moreover, the newly generated carboxylic groups in CRISPR residual lignin further contributed to the pulp hydrophilicity, enhanced polarity and ease water retention in the fibrils, thereby improving fibril-solvent interactions and resulting in their swelling. The efficient defibrillation was observed by a reduction in energy compositions up to 25% and LCNF with smaller diameters compared to the wildtype. The resulting CRISPR LCNF films also presented a better mechanical performance compared to

the wildtype. The WVTR of CRISPR is not dependent on the chemical composition only and might have been favored by the enhanced interfibril interactions caused by the engineered trees.

Chapter 5. Conclusions and Future Work

In this work, we dedicated our efforts to exploring each step of cellulose nanofibril (CNF) production, from the influence of raw materials, processing conditions, and surface post-treatment to ease their technological transfer to the marketplace. We aimed to determine how these factors affect specifically water and water vapor barrier of CNF films without compromising other properties of CNFs.

Chapter 2 established that CNF films can be tailored for specific applications by optimizing processing conditions, yielding films with a diverse range of mechanical strength and water vapor barrier properties. CNF films demonstrated that the optimal tensile strength is achieved under mild processing conditions, while harsh processing conditions are required to further diminish the water vapor permeability of the films. We merged the experimental conditions and fitted them into a predictive model based on the process conditions. The least squares predictive model efficiently fits the experimental data for mechanical strength. However, the model did not work for water vapor permeability and the mechanisms in CNF films remain to be elucidated.

Chapter 3 demonstrated how Dielectric Barrier Discharge (DBD) plasma technology can be utilized to modify the surface properties of CNF films without affecting their bulk performance. The deposition of organosilicon precursors by DBD plasma resulted in the formation of a uniform, porous, superhydrophobic coating of organosilicon fragments on the surface of CNF films. With the addition of an oxidizing plasma gas, it was possible to alter the surface chemistry of the organosilicon coating and increase its hydrophilicity. Such approach, however, created surface defects, resulting in a decreased of the coating barrier

performance. A multilayer approach was suggested to offset observed defects in a single plasma layer and showed promise as an additional hydrophobic layer atop of the hydrophilic one, restored the superhydrophobicity of the coating and improved the water vapor barrier by partial coverage of the defects, and mitigated the capillary forces and hydrophilicity of the system. Further research is needed to understand how different physical regimes can affect coating density, porosity and uniformity, for improved moisture and gas barrier.

Chapter 4 explored for the first time the use of CRISPR-edited woods as feedstocks for the production of lignin-containing cellulose nanofibrils (LCNFs). The study is highlighted by CRISPR trees with higher yields and higher carbohydrates to lignin (C/L) ratio after chemical pulping. Moreover, CRISPR showed the presences of aldehydes that are not found in the wildtype. These changes in lignin structure and higher C/L also resulted in LCNFs with smaller diameters and in turn, in LCNF films with improved mechanical performance. More importantly, the higher mechanical performance was achieved with 25% less energy. The moisture barrier properties, however, were negatively compromised. Our results showed that CRISPR wood is a promising feedstock for energy efficient production of LCNFs but also for understanding at a deeper level the process-structure-performance relationships of CNFs. Hence, it is an approach to consider for advancing the commercialization of CNFs, and guiding end-users.

References

- Adamopoulos, S., Passialis, C., & Voulgaridis, E. (2007). *Strength properties of juvenile and mature wood in black locust (robinia pseudoacacia l.)*.
- Adler, E. (1977). Lignin Chemistry-Past, Present and Future. *Wood Sci. Technol.* , 11, 169–218.
- Ahankari, S. S., Subhedar, A. R., Bhadauria, S. S., & Dufresne, A. (2021). Nanocellulose in food packaging: A review. *Carbohydrate Polymers*, 255(August 2020), 117479. <https://doi.org/10.1016/j.carbpol.2020.117479>
- Ahmad, E., & Pant, K. K. (2018). Chapter 14 - Lignin Conversion: A Key to the Concept of Lignocellulosic Biomass-Based Integrated Biorefinery. In T. Bhaskar, A. Pandey, S. V. Mohan, D.-J. Lee, & S. K. Khanal (Eds.), *Waste Biorefinery* (pp. 409–444). Elsevier. <https://doi.org/https://doi.org/10.1016/B978-0-444-63992-9.00014-8>
- Albornoz-Palma, G., Ching, D., Valerio, O., Mendonça, R. T., & Pereira, M. (2020). Effect of lignin and hemicellulose on the properties of lignocellulose nanofibril suspensions. In *Cellulose* (Vol. 27, Issue 18, pp. 10631–10647). Springer Science and Business Media B.V. <https://doi.org/10.1007/s10570-020-03304-5>
- Albornoz-Palma, G., Ortega-Sanhueza, I., Teruel-Juanes, R., Henríquez-Gallegos, S., Ribes-Greus, A., & Pereira, M. (2023a). Effect of lignin on the morphological, rheological, and dielectric characteristics of lignocellulose nanofibrils from *Pinus radiata*. *Industrial Crops and Products*, 204. <https://doi.org/10.1016/j.indcrop.2023.117323>
- Albornoz-Palma, G., Ortega-Sanhueza, I., Teruel-Juanes, R., Henríquez-Gallegos, S., Ribes-Greus, A., & Pereira, M. (2023b). Understanding the effect of lignin on the production

process and characteristics of lignocellulose nanofibrils from *Eucalyptus nitens*.

Cellulose, 30(11), 6811–6831. <https://doi.org/10.1007/s10570-023-05299-1>

Albornoz-Palma, G., Ortega-Sanhueza, I., Teruel-Juanes, R., Henríquez-Gallegos, S., Ribes-Greus, A., & Pereira, M. (2023c). Understanding the effect of lignin on the production process and characteristics of lignocellulose nanofibrils from *Eucalyptus nitens*.

Cellulose, 30(11), 6811–6831. <https://doi.org/10.1007/s10570-023-05299-1>

Amini, E., Hafez, I., Tajvidi, M., & Bousfield, D. W. (2020). Cellulose and lignocellulose nanofibril suspensions and films: A comparison. *Carbohydrate Polymers*, 250(August), 117011. <https://doi.org/10.1016/j.carbpol.2020.117011>

Andresen, M., Johansson, L. S., Tanem, B. S., & Stenius, P. (2006). Properties and characterization of hydrophobized microfibrillated cellulose. *Cellulose*, 13(6), 665–677. <https://doi.org/10.1007/s10570-006-9072-1>

Ang, S., Haritos, V., & Batchelor, W. (2019a). Effect of refining and homogenization on nanocellulose fiber development, sheet strength and energy consumption. *Cellulose*, 26(8), 4767–4786. <https://doi.org/10.1007/s10570-019-02400-5>

Ang, S., Haritos, V., & Batchelor, W. (2019b). Effect of refining and homogenization on nanocellulose fiber development, sheet strength and energy consumption. *Cellulose*, 26(8), 4767–4786. <https://doi.org/10.1007/s10570-019-02400-5>

Anukiruthika, T., Sethupathy, P., Wilson, A., Kashampur, K., Moses, J. A., & Anandharamakrishnan, C. (2020). Multilayer packaging: Advances in preparation techniques and emerging food applications. *Comprehensive Reviews in Food Science and Food Safety*, 19(3), 1156–1186. <https://doi.org/10.1111/1541-4337.12556>

- Argyropoulos, D. S. (1995). 31p NMR IN WOOD CHEMISTRY: A REVIEW OF RECENT PROGRESS. In *Res. Chem. Intermed* (Vol. 21).
- Arvidsson, R., Nguyen, D., & Svanström, M. (2015). Life cycle assessment of cellulose nanofibrils production by mechanical treatment and two different pretreatment processes. *Environmental Science and Technology*, 49(11), 6881–6890.
<https://doi.org/10.1021/acs.est.5b00888>
- Asadollahi, S., Profili, J., Farzaneh, M., & Stafford, L. (2019). Development of Organosilicon-based superhydrophobic coatings through atmospheric pressure plasma polymerization of HMDSO in nitrogen plasma. *Materials*, 12(2).
<https://doi.org/10.3390/ma12020219>
- ASTM E96. (2000). *Standard Test Methods for Water Vapor Transmission of Materials*.
www.astm.org
- Aulin, C., Ahok, S., Josefsson, P., Nishino, T., Hirose, Y., Österberg, M., & Wågberg, L. (2009). Nanoscale cellulose films with different crystallinities and mesostructures - Their surface properties and interaction with water. *Langmuir*, 25(13), 7675–7685.
<https://doi.org/10.1021/la900323n>
- Babaei, S., Profili, J., Al Rashidi, M., Dorris, A., Beck, S., Asadollahi, S., Sarkissian, A., & Stafford, L. (2023). Permeation properties of a plasma-processed organosilicon–carboxymethylcellulose bilayer on fibrillated cellulosic films for sustainable packaging applications. *Cellulose*. <https://doi.org/10.1007/s10570-023-05367-6>
- Babaei, S., Profili, J., Asadollahi, S., Sarkassian, A., Dorris, A., Beck, S., & Stafford, L. (2020). Analysis of transport phenomena during plasma deposition of hydrophobic coatings on porous cellulosic substrates in plane-to-plane dielectric barrier discharges at

atmospheric pressure. *Plasma Processes and Polymers*, 17(12).

<https://doi.org/10.1002/ppap.202000091>

Baglioni, P., Chelazzi, D., & Giorgi, R. (2021). Nanorestart: Nanomaterials for the restoration of works of art. *Heritage Science*, 9(1), 1–5. <https://doi.org/10.1186/s40494-020-00477-x>

Balakshin, M. Y., Capanema, E. A., Chen, C. L., & Gracz, H. S. (2003). Elucidation of the structures of residual and dissolved pine kraft lignins using an HMQC NMR technique. *Journal of Agricultural and Food Chemistry*, 51(21), 6116–6127.

<https://doi.org/10.1021/jf034372d>

Barreca, D., Gasparotto, A., Maccato, C., Maragno, C., Tondello, E., & Rossetto, G. (2007).

Low-temperature PECVD of transparent SiO_xCyH_z thin films. *Chemical Vapor Deposition*, 13(5), 205–210. <https://doi.org/10.1002/cvde.200606518>

Bauer, A. S., Tacker, M., Uysal-Unalan, I., Cruz, R. M. S., Varzakas, T., & Krauter, V.

(2021). Recyclability and redesign challenges in multilayer flexible food packaging—a review. In *Foods* (Vol. 10, Issue 11). MDPI. <https://doi.org/10.3390/foods10112702>

Bedane, A. H., Eić, M., Farmahini-Farahani, M., & Xiao, H. (2016). Theoretical modeling of water vapor transport in cellulose-based materials. *Cellulose*, 23(3), 1537–1552.

<https://doi.org/10.1007/s10570-016-0917-y>

Bendtsen, B. A., & Senft, J. (1986). MECHANICAL AND ANATOMICAL PROPERTIES IN INDIVIDUAL GROWTH RINGS OF PLANTATION-GROWN EASTERN COTTONWOOD AND LOBLOLLY PINE. *Wood and Fiber Science*, 18(1), 23–38.

Benítez, A. J., & Walther, A. (2017). Cellulose nanofibril nanopapers and bioinspired

nanocomposites: A review to understand the mechanical property space. In *Journal of*

Materials Chemistry A (Vol. 5, Issue 31, pp. 16003–16024). Royal Society of Chemistry. <https://doi.org/10.1039/c7ta02006f>

Bian, H., Chen, L., Dong, M., Wang, L., Wang, R., Zhou, X., Wu, C., Wang, X., Ji, X., & Dai, H. (2021). Natural lignocellulosic nanofibril film with excellent ultraviolet blocking performance and robust environment resistance. *International Journal of Biological Macromolecules*, *166*, 1578–1585.

<https://doi.org/10.1016/j.ijbiomac.2020.11.037>

Bian, H., Gao, Y., Wang, R., Liu, Z., Wu, W., & Dai, H. (2018). Contribution of lignin to the surface structure and physical performance of cellulose nanofibrils film. *Cellulose*, *25*(2), 1309–1318. <https://doi.org/10.1007/s10570-018-1658-x>

Butler, T. I., & Morris, B. A. (2009). PE based multilayer film structures. In *Multilayer Flexible Packaging: Technology and Applications for the Food, Personal Care, and Over-the-Counter Pharmaceutical Industries* (pp. 205–230). Elsevier.

<https://doi.org/10.1016/B978-0-8155-2021-4.10015-2>

Camargos, C. H. M., Poggi, G., Chelazzi, D., Baglioni, P., & Rezende, C. A. (2022).

Protective Coatings Based on Cellulose Nanofibrils, Cellulose Nanocrystals, and Lignin Nanoparticles for the Conservation of Cellulosic Artifacts. *ACS Applied Nano Materials*, *5*(9), 13245–13259. <https://doi.org/10.1021/acsanm.2c02968>

<https://doi.org/10.1021/acsanm.2c02968>

Cao, S., Pu, Y., Studer, M., Wyman, C., & Ragauskas, A. J. (2012). Chemical transformations of *Populus trichocarpa* during dilute acid pretreatment. *RSC Advances*, *2*(29), 10925–10936. <https://doi.org/10.1039/c2ra22045h>

Cazón, P., Morales-Sanchez, E., Velazquez, G., & Vázquez, M. (2022). Measurement of the Water Vapor Permeability of Chitosan Films: A Laboratory Experiment on Food

Packaging Materials. *Journal of Chemical Education*, 99(6), 2403–2408.

<https://doi.org/10.1021/acs.jchemed.2c00449>

Chaker, A., Alila, S., Mutjé, P., Vilar, M. R., & Boufi, S. (2013a). Key role of the hemicellulose content and the cell morphology on the nanofibrillation effectiveness of cellulose pulps. *Cellulose*, 20(6), 2863–2875. <https://doi.org/10.1007/s10570-013-0036-y>

Chaker, A., Alila, S., Mutjé, P., Vilar, M. R., & Boufi, S. (2013b). Key role of the hemicellulose content and the cell morphology on the nanofibrillation effectiveness of cellulose pulps. *Cellulose*, 20(6), 2863–2875. <https://doi.org/10.1007/s10570-013-0036-y>

CHANG, R. P. H. (1983). PLASMA OXIDATION OF SEMICONDUCTOR AND METAL SURFACES. In M. FROMENT (Ed.), *Passivity of Metals and Semiconductors* (pp. 437–444). Elsevier. [https://doi.org/https://doi.org/10.1016/B978-0-444-42252-1.50070-9](https://doi.org/10.1016/B978-0-444-42252-1.50070-9)

Chen, M., Parot, J., Hackley, V. A., Zou, S., & Johnston, L. J. (2021). AFM characterization of cellulose nanocrystal height and width using internal calibration standards. *Cellulose*, 28(4), 1933–1946. <https://doi.org/10.1007/s10570-021-03678-0>

Chen, S., Song, Y., & Xu, F. (2018). Highly Transparent and Hazy Cellulose Nanopaper Simultaneously with a Self-Cleaning Superhydrophobic Surface. *ACS Sustainable Chemistry and Engineering*, 6(4), 5173–5181. <https://doi.org/10.1021/acssuschemeng.7b04814>

Chen, W., Yu, H., Liu, Y., Chen, P., Zhang, M., & Hai, Y. (2011). Individualization of cellulose nanofibers from wood using high-intensity ultrasonication combined with

chemical pretreatments. *Carbohydrate Polymers*, 83(4), 1804–1811.

<https://doi.org/10.1016/j.carbpol.2010.10.040>

Cheng, D., Wei, P., Zhang, L., & Cai, J. (2018). Surface-initiated atom transfer radical polymerization grafting from nanoporous cellulose gels to create hydrophobic nanocomposites. *RSC Advances*, 8(48), 27045–27053.

<https://doi.org/10.1039/c8ra04163f>

Cheremisinoff, N. P., & Rosenfeld, P. E. (2010). Structure and Characteristics of Lignin. In *Lignin Chemistry and Applications* (pp. 25–50). Elsevier. <https://doi.org/10.1016/b978-0-12-813941-7.00002-3>

Cvelbar, U., Walsh, J. L., Černák, M., de Vries, H. W., Reuter, S., Belmonte, T., Corbella, C., Miron, C., Hojnik, N., Jurov, A., Puliyalil, H., Gorjanc, M., Portal, S., Laurita, R., Colombo, V., Schäfer, J., Nikiforov, A., Modic, M., Kylian, O., ... Weltmann, K. D. (2019). White paper on the future of plasma science and technology in plastics and textiles. *Plasma Processes and Polymers*, 16(1), 1–37.

<https://doi.org/10.1002/ppap.201700228>

Davidsdottir, B. (2013). Forest Products and Energy. In *Reference Module in Earth Systems and Environmental Sciences*. Elsevier. <https://doi.org/10.1016/b978-0-12-409548-9.01454-8>

Delgado-Aguilar, M., González, I., Tarrés, Q., Pèlach, M. À., Alcalà, M., & Mutjé, P. (2016). The key role of lignin in the production of low-cost lignocellulosic nanofibres for papermaking applications. *Industrial Crops and Products*, 86, 295–300.

<https://doi.org/10.1016/j.indcrop.2016.04.010>

- Deng, S., Huang, R., Zhou, M., Chen, F., & Fu, Q. (2016). Hydrophobic cellulose films with excellent strength and toughness via ball milling activated acylation of microfibrillated cellulose. *Carbohydrate Polymers*, *154*, 129–138.
<https://doi.org/10.1016/j.carbpol.2016.07.101>
- Djafari Petroudy, S. R., Chabot, B., Loranger, E., Naebe, M., Shojaeiarani, J., Gharehkhani, S., Ahvazi, B., Hu, J., & Thomas, S. (2021). Recent advances in cellulose nanofibers preparation through energy-efficient approaches: A review. *Energies*, *14*(20), 1–31.
<https://doi.org/10.3390/en14206792>
- Dong, S., Bortner, M. J., & Roman, M. (2016). Analysis of the sulfuric acid hydrolysis of wood pulp for cellulose nanocrystal production: A central composite design study. *Industrial Crops and Products*, *93*, 76–87.
<https://doi.org/10.1016/j.indcrop.2016.01.048>
- Durán, I. R., Profili, J., Stafford, L., & Laroche, G. (2020). Unveiling the origin of the anti-fogging performance of plasma-coated glass: Role of the structure and the chemistry of siloxane precursors. *Progress in Organic Coatings*, *141*.
<https://doi.org/10.1016/j.porgcoat.2019.105401>
- Fahlteich, J., Mogck, S., Wanski, T., Schiller, N., Amerg-Shwab, S., Weber, U., Miesbauer, O., Küçükpinar-Niarchos, E., Noller, K., & Boeffel, C. (2015). The Role of Defects in Single- and Multi-Layer Barriers for Flexible Electronics. *Society of Vacuum Coaters 57th (2014) Annual Technical Conference Proceedings*, *57*, 403–413.
<https://doi.org/10.14332/svc14.proc.1881>
- Fávaro, S. L., Freitas, A. R., Ganzerli, T. A., Pereira, A. G. B., Cardozo, A. L., Baron, O., Muniz, E. C., Giroto, E. M., & Radovanovic, E. (2013a). PET and aluminum recycling

from multilayer food packaging using supercritical ethanol. *Journal of Supercritical Fluids*, 75, 138–143. <https://doi.org/10.1016/j.supflu.2012.12.015>

Fávaro, S. L., Freitas, A. R., Ganzerli, T. A., Pereira, A. G. B., Cardozo, A. L., Baron, O., Muniz, E. C., Giroto, E. M., & Radovanovic, E. (2013b). PET and aluminum recycling from multilayer food packaging using supercritical ethanol. *Journal of Supercritical Fluids*, 75, 138–143. <https://doi.org/10.1016/j.supflu.2012.12.015>

Fazeli, M., Florez, J. P., & Simão, R. A. (2019). Improvement in adhesion of cellulose fibers to the thermoplastic starch matrix by plasma treatment modification. *Composites Part B: Engineering*, 163, 207–216. <https://doi.org/10.1016/j.compositesb.2018.11.048>

Ferrer, A., Quintana, E., Filpponen, I., Solala, I., Vidal, T., Rodríguez, A., Laine, J., & Rojas, O. J. (2012). Effect of residual lignin and heteropolysaccharides in nanofibrillar cellulose and nanopaper from wood fibers. *Cellulose*, 19(6), 2179–2193. <https://doi.org/10.1007/s10570-012-9788-z>

Fotie, G., Limbo, S., & Piergiovanni, L. (2020). Manufacturing of food packaging based on nanocellulose: Current advances and challenges. *Nanomaterials*, 10(9), 1–26. <https://doi.org/10.3390/nano10091726>

Frank, B. P., Durkin, D. P., Caudill, E. R., Zhu, L., White, D. H., Curry, M. L., Pedersen, J. A., & Fairbrother, D. H. (2018). Impact of Silanization on the Structure, Dispersion Properties, and Biodegradability of Nanocellulose as a Nanocomposite Filler. *ACS Applied Nano Materials*, 1(12), 7025–7038. <https://doi.org/10.1021/acsanm.8b01819>

Froass, P. M., Ragauskas, A. J., Mcdonough, T. J., & Jiang, J. E. (1996). *IPST Technical Paper Series Number 606 Relationship Between Residual Lignin Structure and Pulp Bleachability*.

- Gierer, J. (1980). Chemical Aspects of Kraft Pulping. *Wood Sci. Technol.*, 241–266.
- Håkansson, K. M. O. (2021). Effect of carboxymethylated cellulose nanofibril concentration regime upon material forming on mechanical properties in films and filaments. *Cellulose*, 28(2), 881–895. <https://doi.org/10.1007/s10570-020-03566-z>
- Han, J. W., Ruiz-Garcia, L., Qian, J. P., & Yang, X. T. (2018). Food Packaging: A Comprehensive Review and Future Trends. In *Comprehensive Reviews in Food Science and Food Safety* (Vol. 17, Issue 4, pp. 860–877). Blackwell Publishing Inc. <https://doi.org/10.1111/1541-4337.12343>
- Hasan, I., Wang, J., & Tajvidi, M. (2021). Tuning physical, mechanical and barrier properties of cellulose nanofibril films through film drying techniques coupled with thermal compression. *Cellulose*, 28(18), 11345–11366. <https://doi.org/10.1007/s10570-021-04269-9>
- He, J., Wen, X., Wu, L., Chen, H., Hu, J., & Hou, X. (2022). Dielectric barrier discharge plasma for nanomaterials: Fabrication, modification and analytical applications. In *TrAC - Trends in Analytical Chemistry* (Vol. 156). Elsevier B.V. <https://doi.org/10.1016/j.trac.2022.116715>
- Henriksson, M., Berglund, L. A., Isaksson, P., Lindström, T., & Nishino, T. (2008). Cellulose nanopaper structures of high toughness. *Biomacromolecules*, 9(6), 1579–1585. <https://doi.org/10.1021/bm800038n>
- Herrick, F., Shelton, & Wash. (1984). *Process for preparing microfibrillated cellulose* (Patent 4,481,077).

- Hofstetter, K., Hinterstoisser, B., & Salmén, L. (2006). Moisture uptake in native cellulose - The roles of different hydrogen bonds: A dynamic FT-IR study using Deuterium exchange. *Cellulose*, *13*(2), 131–145. <https://doi.org/10.1007/s10570-006-9055-2>
- Hu, C., Zhao, Y., Li, K., Zhu, J. Y., & Gleisner, R. (2015). Optimizing cellulose fibrillation for the production of cellulose nanofibrils by a disk grinder. *Holzforschung*, *69*(8), 993–1000. <https://doi.org/10.1515/hf-2014-0219>
- Ishikawa, G., & Kondo, T. (2021). Characterization of dual nano-size effects of ACC-cellulose nanofibrils on crystallization behavior of hydrophilic poly(vinyl alcohol). *Journal of Wood Science*, *67*(1). <https://doi.org/10.1186/s10086-021-01957-9>
- Isogai, A. (2020). Cellulose Nanofibers: Recent Progress and Future Prospects. *Journal of Fiber Science and Technology*, *76*(10), 310–326. <https://doi.org/10.2115/FIBERST.2020-0039>
- Iwamoto, S., Abe, K., & Yano, H. (2008). The effect of hemicelluloses on wood pulp nanofibrillation and nanofiber network characteristics. *Biomacromolecules*, *9*(3), 1022–1026. <https://doi.org/10.1021/bm701157n>
- Jannatyha, N., Shojaee-Aliabadi, S., Moslehishad, M., & Moradi, E. (2020). Comparing mechanical, barrier and antimicrobial properties of nanocellulose/CMC and nanochitosan/CMC composite films. *International Journal of Biological Macromolecules*, *164*, 2323–2328. <https://doi.org/10.1016/j.ijbiomac.2020.07.249>
- Jardim, J. M., Hart, P. W., Lucia, L. A., Jameel, H., & Chang, H. M. (2022). The Effect of the Kraft Pulping Process, Wood Species, and pH on Lignin Recovery from Black Liquor. *Fibers*, *10*(2). <https://doi.org/10.3390/fib10020016>

- Jardim, J. M., Hart, P. W., Lucia, L., & Jameel, H. (2020). Insights into the potential of hardwood kraft lignin to be a green platform material for emergence of the biorefinery. *Polymers*, *12*(8). <https://doi.org/10.3390/polym12081795>
- Jiang, B., Chen, C., Liang, Z., He, S., Kuang, Y., Song, J., Mi, R., Chen, G., Jiao, M., & Hu, L. (2020). Lignin as a Wood-Inspired Binder Enabled Strong, Water Stable, and Biodegradable Paper for Plastic Replacement. *Advanced Functional Materials*, *30*(4). <https://doi.org/10.1002/adfm.201906307>
- Jonasson, S., Bänder, A., Berglund, L., Niittylä, T., & Oksman, K. (2022). Characteristics of Cellulose Nanofibrils from Transgenic Trees with Reduced Expression of Cellulose Synthase Interacting 1. *Nanomaterials*, *12*(19). <https://doi.org/10.3390/nano12193448>
- Jonasson, S., Bänder, A., Das, O., Niittylä, T., & Oksman, K. (2021). Comparison of tension wood and normal wood for oxidative nanofibrillation and network characteristics. *Cellulose*, *28*(2), 1085–1104. <https://doi.org/10.1007/s10570-020-03556-1>
- Jonoobi, M., Harun, J., Mathew, A. P., Hussein, M. Z. B., & Oksman, K. (2010). Preparation of cellulose nanofibers with hydrophobic surface characteristics. *Cellulose*, *17*(2), 299–307. <https://doi.org/10.1007/s10570-009-9387-9>
- Jonoobi, M., Oladi, R., Davoudpour, Y., Oksman, K., Dufresne, A., Hamzeh, Y., & Davoodi, R. (2015). Different preparation methods and properties of nanostructured cellulose from various natural resources and residues: a review. *Cellulose*, *22*(2), 935–969. <https://doi.org/10.1007/s10570-015-0551-0>
- Joshi, P. P., Pulikollu, R., Higgins, S. R., Hu, X., & Mukhopadhyay, S. M. (2006). Investigation of growth, coverage and effectiveness of plasma assisted nano-films of

fluorocarbon. *Applied Surface Science*, 252(16), 5676–5686.

<https://doi.org/10.1016/j.apsusc.2005.07.061>

Jung, Y. H., Chang, T. H., Zhang, H., Yao, C., Zheng, Q., Yang, V. W., Mi, H., Kim, M., Cho, S. J., Park, D. W., Jiang, H., Lee, J., Qiu, Y., Zhou, W., Cai, Z., Gong, S., & Ma, Z. (2015). High-performance green flexible electronics based on biodegradable cellulose nanofibril paper. *Nature Communications*, 6(May).

<https://doi.org/10.1038/ncomms8170>

Kaiser, K., Schmid, M., & Schlummer, M. (2018a). Recycling of polymer-based multilayer packaging: A review. *Recycling*, 3(1). <https://doi.org/10.3390/recycling3010001>

Kaiser, K., Schmid, M., & Schlummer, M. (2018b). Recycling of polymer-based multilayer packaging: A review. *Recycling*, 3(1). <https://doi.org/10.3390/recycling3010001>

Kakkar, S., Harjani, B., Ledwani, N., & Ledwani, L. (2020). *Nanotechnology for Energy and Environmental Engineering*. http://link.springer.com/10.1007/978-3-030-33774-2_2
<http://link.springer.com/10.1007/978-3-030-33774-2>

Kandhola, G., Djiroleu, A., Rajan, K., Batta-Mpouma, J., Labbé, N., Sakon, J., Babst, B. A., Ghosh, A., Carrier, D. J., & Kim, J. W. (2022). Impact of species-based wood feedstock variability on physicochemical properties of cellulose nanocrystals. *Cellulose*, 29(15), 8213–8228. <https://doi.org/10.1007/s10570-022-04762-9>

Karande, V. S., Mhaske, S. T., Bharimalla, A. K., Hadge, G. B., & Vigneshwaran, N. (2013). Evaluation of two-stage process (refining and homogenization) for nanofibrillation of cotton fibers. *Polymer Engineering and Science*, 53(8), 1590–1597.

<https://doi.org/10.1002/pen.23413>

- Khakalo, A., Mäkelä, T., Johansson, L. S., Orelma, H., & Tammelin, T. (2020a). High-Throughput Tailoring of Nanocellulose Films: From Complex Bio-Based Materials to Defined Multifunctional Architectures. *ACS Applied Bio Materials*, 3(11), 7428–7438. <https://doi.org/10.1021/acsabm.0c00576>
- Khakalo, A., Mäkelä, T., Johansson, L. S., Orelma, H., & Tammelin, T. (2020b). High-Throughput Tailoring of Nanocellulose Films: From Complex Bio-Based Materials to Defined Multifunctional Architectures. *ACS Applied Bio Materials*, 3(11), 7428–7438. <https://doi.org/10.1021/acsabm.0c00576>
- Kim, H. J., Roy, S., & Rhim, J. W. (2021). Effects of various types of cellulose nanofibers on the physical properties of the CNF-based films. *Journal of Environmental Chemical Engineering*, 9(5), 106043. <https://doi.org/10.1016/j.jece.2021.106043>
- Kondo, T. (2022). Cellulose Nanofibrils Pulverized from Biomass Resources: Past, Present, and Future Perspectives. *KONA Powder and Particle Journal*, February, 2023003. <https://doi.org/10.14356/kona.2023003>
- Kondo, T., Kose, R., Naito, H., & Kasai, W. (2014). Aqueous counter collision using paired water jets as a novel means of preparing bio-nanofibers. *Carbohydrate Polymers*, 112, 284–290. <https://doi.org/10.1016/j.carbpol.2014.05.064>
- Kondo, T., Morita, M., Hayakawa K., & Onda, Y. (2008). *WET PULVERIZING OF POLYSACCHARDES* (Patent US 7,357,339 B2).
- Kondo, T., Morita, M., Hayakawa, K., & Onda, Y. (2008). *WET PULVERIZING OF POLYSACCHARDES* (Patent US 7,357,339 B2).
- Koppolu, R., Lahti, J., Abitbol, T., Swerin, A., Kuusipalo, J., & Toivakka, M. (2019a). Continuous Processing of Nanocellulose and Polylactic Acid into Multilayer Barrier

Coatings. *ACS Applied Materials and Interfaces*, 11(12), 11920–11927.

<https://doi.org/10.1021/acsami.9b00922>

Koppolu, R., Lahti, J., Abitbol, T., Swerin, A., Kuusipalo, J., & Toivakka, M. (2019b).

Continuous Processing of Nanocellulose and Polylactic Acid into Multilayer Barrier Coatings. *ACS Applied Materials and Interfaces*, 11(12), 11920–11927.

<https://doi.org/10.1021/acsami.9b00922>

Kriechbaum, K., Munier, P., Apostolopoulou-Kalkavoura, V., & Lavoine, N. (2018).

Analysis of the Porous Architecture and Properties of Anisotropic Nanocellulose Foams: A Novel Approach to Assess the Quality of Cellulose Nanofibrils (CNFs). *ACS Sustainable Chemistry and Engineering*, 6(9), 11959–11967.

<https://doi.org/10.1021/acssuschemeng.8b02278>

Krutul, D., Antczak, A., Radomski, A., Drożdżek, M., Kłosińska, T., & Zawadzki, J. (2019).

The chemical composition of poplar wood in relation to the species and age of trees. In *Forestry and Wood Technology* (Vol. 105).

Kumar, A., Sood, A., Maiti, P., & Han, S. S. (2023). Lignin-containing nanocelluloses

(LNCs) as renewable and sustainable alternatives: Prospects, and challenges. In *Current Opinion in Green and Sustainable Chemistry* (Vol. 41). Elsevier B.V.

<https://doi.org/10.1016/j.cogsc.2023.100830>

Kumar, V., Bollström, R., Yang, A., Chen, Q., Chen, G., Salminen, P., Bousfield, D., &

Toivakka, M. (2014). Comparison of nano- and microfibrillated cellulose films.

Cellulose, 21(5), 3443–3456. <https://doi.org/10.1007/s10570-014-0357-5>

- Labosky, P., Bowersox, T. W., & Blankenhorn, P. R. (1983). KRAFT PULP YIELDS AND PAPER PROPERTIES OBTAINED FROM FIRST AND SECOND ROTATIONS OF THREE HYBRID POPLAR CLONES¹. *Wood and Fiber Science*.
- Lahtinen, P., Liukkonen, S., Pere, J., Sneek, A., & Kangas, H. (2014). *A Comparative Study of Fibrillated Fibers from Different Mechanical and Chemical Pulps*.
- Laroussi, M. (2020). Cold Plasma in Medicine and Healthcare: The New Frontier in Low Temperature Plasma Applications. In *Frontiers in Physics* (Vol. 8). Frontiers Media SA. <https://doi.org/10.3389/fphy.2020.00074>
- Le Gars, M., Dhuiège, B., Delvart, A., Belgacem, M. N., Missoum, K., & Bras, J. (2020). High-barrier and antioxidant poly(lactic acid)/nanocellulose multilayered materials for packaging. *ACS Omega*, 5(36), 22816–22826. <https://doi.org/10.1021/acsomega.0c01955>
- Levasseur, O., Stafford, L., Gherardi, N., Naudé, N., Beche, E., Esvan, J., Blanchet, P., Riedl, B., & Sarkissian, A. (2013). Role of substrate outgassing on the formation dynamics of either hydrophilic or hydrophobic wood surfaces in atmospheric-pressure, organosilicon plasmas. *Surface and Coatings Technology*, 234, 42–47. <https://doi.org/10.1016/j.surfcoat.2013.05.045>
- Li, H., Cui, B., Janaswamy, S., & Guo, L. (2019). Structural and functional modifications of kudzu starch modified by branching enzyme. *International Journal of Food Properties*, 22(1), 952–966. <https://doi.org/10.1080/10942912.2019.1619576>
- Li, J., Wei, X., Wang, Q., Chen, J., Chang, G., Kong, L., Su, J., & Liu, Y. (2012). Homogeneous isolation of nanocellulose from sugarcane bagasse by high pressure

homogenization. *Carbohydrate Polymers*, 90(4), 1609–1613.

<https://doi.org/10.1016/j.carbpol.2012.07.038>

Li, W., Wang, S., Wang, W., Qin, C., & Wu, M. (2019). Facile preparation of reactive hydrophobic cellulose nanofibril film for reducing water vapor permeability (WVP) in packaging applications. *Cellulose*, 26(5), 3271–3284. <https://doi.org/10.1007/s10570-019-02270-x>

Lichtenstein, K., & Lavoine, N. (2017). Toward a deeper understanding of the thermal degradation mechanism of nanocellulose. *Polymer Degradation and Stability*, 146, 53–60. <https://doi.org/10.1016/j.polymdegradstab.2017.09.018>

Liu, K., Du, H., Zheng, T., Liu, W., Zhang, M., Liu, H., Zhang, X., & Si, C. (2021). Lignin-containing cellulose nanomaterials: Preparation and applications. In *Green Chemistry* (Vol. 23, Issue 24, pp. 9723–9746). Royal Society of Chemistry. <https://doi.org/10.1039/d1gc02841c>

Liu, X., Jiang, Y., Qin, C., Yang, S., Song, X., Wang, S., & Li, K. (2018). Enzyme-assisted mechanical grinding for cellulose nanofibers from bagasse: energy consumption and nanofiber characteristics. *Cellulose*, 25(12), 7065–7078. <https://doi.org/10.1007/s10570-018-2071-1>

Maechler, L., Sarra-Bournet, C., Chevallier, P., Gherardi, N., & Laroche, G. (2011). Anti-fog layer deposition onto polymer materials: A multi-step approach. *Plasma Chemistry and Plasma Processing*, 31(1), 175–187. <https://doi.org/10.1007/s11090-010-9261-4>

Mahardika, M., Amelia, D., Azril, & Syafri, E. (2023). Applications of nanocellulose and its composites in bio packaging-based starch. *Materials Today: Proceedings*, 74, 415–418. <https://doi.org/10.1016/j.matpr.2022.11.138>

- Malucelli, L. C., Matos, M., Jordão, C., Lomonaco, D., Lacerda, L. G., Carvalho Filho, M. A. S., & Magalhães, W. L. E. (2019a). Influence of cellulose chemical pretreatment on energy consumption and viscosity of produced cellulose nanofibers (CNF) and mechanical properties of nanopaper. *Cellulose*, 26(3), 1667–1681.
<https://doi.org/10.1007/s10570-018-2161-0>
- Malucelli, L. C., Matos, M., Jordão, C., Lomonaco, D., Lacerda, L. G., Carvalho Filho, M. A. S., & Magalhães, W. L. E. (2019b). Influence of cellulose chemical pretreatment on energy consumption and viscosity of produced cellulose nanofibers (CNF) and mechanical properties of nanopaper. *Cellulose*, 26(3), 1667–1681.
<https://doi.org/10.1007/s10570-018-2161-0>
- Martinu, L., Werthelmer, M. R., & Klemberg-Sapieha, L. (1999). *RECENT ADVANCES IN PLASMA DEPOSITION OF FUNCTIONAL COATINGS ON POLYMERS*.
- Meng, Q., & Wang, T. J. (2019a). Mechanics of Strong and Tough Cellulose Nanopaper. *Applied Mechanics Reviews*, 71(4), 1–30. <https://doi.org/10.1115/1.4044018>
- Meng, Q., & Wang, T. J. (2019b). Mechanics of Strong and Tough Cellulose Nanopaper. *Applied Mechanics Reviews*, 71(4), 1–30. <https://doi.org/10.1115/1.4044018>
- Meng, X., Crestini, C., Ben, H., Hao, N., Pu, Y., Ragauskas, A. J., & Argyropoulos, D. S. (2019). Determination of hydroxyl groups in biorefinery resources via quantitative ³¹P NMR spectroscopy. *Nature Protocols*, 14(9), 2627–2647.
<https://doi.org/10.1038/s41596-019-0191-1>
- Merche, D., Vandecasteele, N., & Reniers, F. (2012). Atmospheric plasmas for thin film deposition: A critical review. In *Thin Solid Films* (Vol. 520, Issue 13, pp. 4219–4236).
<https://doi.org/10.1016/j.tsf.2012.01.026>

- Mokhena, T. C., & John, M. J. (2020). Cellulose nanomaterials: new generation materials for solving global issues. In *Cellulose* (Vol. 27, Issue 3). Springer Netherlands.
<https://doi.org/10.1007/s10570-019-02889-w>
- Mokhena, T. C., Sadiku, E. R., Mochane, M. J., Ray, S. S., John, M. J., & Mtibe, A. (2021a). Mechanical properties of cellulose nanofibril papers and their bionanocomposites: A review. In *Carbohydrate Polymers* (Vol. 273). Elsevier Ltd.
<https://doi.org/10.1016/j.carbpol.2021.118507>
- Mokhena, T. C., Sadiku, E. R., Mochane, M. J., Ray, S. S., John, M. J., & Mtibe, A. (2021b). Mechanical properties of cellulose nanofibril papers and their bionanocomposites: A review. *Carbohydrate Polymers*, 273(May), 118507.
<https://doi.org/10.1016/j.carbpol.2021.118507>
- Moon, D., Sagisaka, M., Tahara, K., & Tsukahara, K. (2017). Progress towards sustainable production: Environmental, economic, and social assessments of the cellulose nanofiber production process. *Sustainability (Switzerland)*, 9(12).
<https://doi.org/10.3390/su9122368>
- Nadeem, H., Athar, M., Dehghani, M., Garnier, G., & Batchelor, W. (2022). Recent advancements, trends, fundamental challenges and opportunities in spray deposited cellulose nanofibril films for packaging applications. *Science of the Total Environment*, 836(May), 155654. <https://doi.org/10.1016/j.scitotenv.2022.155654>
- Nagarajan, K. J., Ramanujam, N. R., Sanjay, M. R., Siengchin, S., Surya Rajan, B., Sathick Basha, K., Madhu, P., & Raghav, G. R. (2021). A comprehensive review on cellulose nanocrystals and cellulose nanofibers: Pretreatment, preparation, and characterization. In *Polymer Composites* (Vol. 42, Issue 4). <https://doi.org/10.1002/pc.25929>

- Najahi, A., Tarrés, Q., Delgado-Aguilar, M., Putaux, J. L., & Boufi, S. (2023). High-Lignin-Containing Cellulose Nanofibrils from Date Palm Waste Produced by Hydrothermal Treatment in the Presence of Maleic Acid. *Biomacromolecules*, 24(8), 3872–3886. <https://doi.org/10.1021/acs.biomac.3c00515>
- Nakagaito, A. N., & Yano, H. (2004). The effect of morphological changes from pulp fiber towards nano-scale fibrillated cellulose on the mechanical properties of high-strength plant fiber based composites. *Applied Physics A: Materials Science and Processing*, 78(4), 547–552. <https://doi.org/10.1007/s00339-003-2453-5>
- Nechyporchuk, O., Belgacem, M. N., & Bras, J. (2016). Production of cellulose nanofibrils: A review of recent advances. *Industrial Crops and Products*, 93, 2–25. <https://doi.org/10.1016/j.indcrop.2016.02.016>
- Noremylia, M. B., Hassan, M. Z., & Ismail, Z. (2022a). Recent advancement in isolation, processing, characterization and applications of emerging nanocellulose: A review. *International Journal of Biological Macromolecules*, 206(January), 954–976. <https://doi.org/10.1016/j.ijbiomac.2022.03.064>
- Noremylia, M. B., Hassan, M. Z., & Ismail, Z. (2022b). Recent advancement in isolation, processing, characterization and applications of emerging nanocellulose: A review. *International Journal of Biological Macromolecules*, 206(March), 954–976. <https://doi.org/10.1016/j.ijbiomac.2022.03.064>
- NREL/TP-510-42618. (2012). *Determination of Structural Carbohydrates and Lignin in Biomass*.

- Osong, S. H., Norgren, S., & Engstrand, P. (2013). An approach to produce nano-ligno-cellulose from mechanical pulp fine materials. *Nordic Pulp and Paper Research Journal*, 28(4), 472–479. <https://doi.org/10.3183/npprj-2013-28-04-p472-479>
- Osong, S. H., Norgren, S., & Engstrand, P. (2016). Processing of wood-based microfibrillated cellulose and nanofibrillated cellulose, and applications relating to papermaking: a review. *Cellulose*, 23(1), 93–123. <https://doi.org/10.1007/s10570-015-0798-5>
- Österberg, M., Vartiainen, J., Lucenius, J., Hippi, U., Seppälä, J., Serimaa, R., & Laine, J. (2013). A fast method to produce strong NFC films as a platform for barrier and functional materials. *ACS Applied Materials and Interfaces*, 5(11), 4640–4647. <https://doi.org/10.1021/am401046x>
- Otoupal, P. B., Geiselman, G. M., Oka, A. M., Barcelos, C. A., Choudhary, H., Dinh, D., Zhong, W., Hwang, H. J., Keasling, J. D., Mukhopadhyay, A., Sundstrom, E., Haushalter, R. W., Sun, N., Simmons, B. A., & Gladden, J. M. (2022). Advanced one-pot deconstruction and valorization of lignocellulosic biomass into triacetic acid lactone using *Rhodosporidium toruloides*. *Microbial Cell Factories*, 21(1). <https://doi.org/10.1186/s12934-022-01977-0>
- Panchal, P., Ogunsona, E., & Mekonnen, T. (2019). Trends in advanced functional material applications of nanocellulose. *Processes*, 7(1). <https://doi.org/10.3390/pr7010010>
- Pasquier, E., Mattos, B. D., Koivula, H., Khakalo, A., Belgacem, M. N., Rojas, O. J., & Bras, J. (2022a). Multilayers of Renewable Nanostructured Materials with High Oxygen and Water Vapor Barriers for Food Packaging. *ACS Applied Materials and Interfaces*, 14(26), 30236–30245. <https://doi.org/10.1021/acsami.2c07579>

- Pasquier, E., Mattos, B. D., Koivula, H., Khakalo, A., Belgacem, M. N., Rojas, O. J., & Bras, J. (2022b). Multilayers of Renewable Nanostructured Materials with High Oxygen and Water Vapor Barriers for Food Packaging. *ACS Applied Materials and Interfaces*, *14*(26), 30236–30245. <https://doi.org/10.1021/acsami.2c07579>
- Pasquier, E., Mattos, B. D., Koivula, H., Khakalo, A., Belgacem, M. N., Rojas, O. J., & Bras, J. (2022c). Multilayers of Renewable Nanostructured Materials with High Oxygen and Water Vapor Barriers for Food Packaging. *ACS Applied Materials and Interfaces*, *14*(26), 30236–30245. <https://doi.org/10.1021/acsami.2c07579>
- Peng, X., Tong, B., Lee, J., Wang, K., Yu, X., Huang, X., Wen, J., Makarem, M., Pang, H., Hinjan, S., Yan, X., Yao, S., Lu, F., Wang, B., Peng, F., Ralph, J., Kim, S. H., Sederoff, R. R., & Li, Q. (2023). Overexpression of a gibberellin 20-oxidase gene in poplar xylem led to an increase in the size of nanocellulose fibrils and improved paper properties. *Carbohydrate Polymers*, *314*. <https://doi.org/10.1016/j.carbpol.2023.120959>
- Pennells, J., Chaléat, C., & Martin, D. J. (2022). Benchmarking the Production of Cellulose Nanofibres: Biomass Feedstock, Mechanical Processing, and Nanopaper Performance. *Journal of Polymers and the Environment*. <https://doi.org/10.1007/s10924-022-02672-2>
- Petersen, J., Bechara, R., Bardon, J., Fouquet, T., Ziarelli, F., Daheron, L., Ball, V., Toniazco, V., Michel, M., Dinia, A., & Ruch, D. (2011). Atmospheric plasma deposition process: A versatile tool for the design of tunable siloxanes-based plasma polymer films. *Plasma Processes and Polymers*, *8*(10), 895–903. <https://doi.org/10.1002/ppap.201100022>

- Poothanari, M. A., & Leterrier, Y. (2024). Fluorine Free Surface Modification of Microfibrillated Cellulose-Clay Composite Films: Effect of Hydrophobicity on Gas Barrier Performance. *Surfaces*, 7(2), 283–295. <https://doi.org/10.3390/surfaces7020019>
- Profili, J., Asadollahi, S., Vinchon, P., Dorris, A., Beck, S., Sarkassian, A., & Stafford, L. (2020a). Recent progress on organosilicon coatings deposited on bleached unrefined Kraft paper by non-thermal plasma process at atmospheric pressure. *Progress in Organic Coatings*, 147(July). <https://doi.org/10.1016/j.porgcoat.2020.105865>
- Profili, J., Asadollahi, S., Vinchon, P., Dorris, A., Beck, S., Sarkassian, A., & Stafford, L. (2020b). Recent progress on organosilicon coatings deposited on bleached unrefined Kraft paper by non-thermal plasma process at atmospheric pressure. *Progress in Organic Coatings*, 147. <https://doi.org/10.1016/j.porgcoat.2020.105865>
- Profili, J., Babaei, S., Al Rashidi, M., Dorris, A., Asadollahi, S., Sarkissian, A., & Stafford, L. (2023). Plasma-Deposited Organosilicon Hydrophobic Coatings on Cellulosic Materials for Wet Packaging Applications. *Coatings*, 13(5). <https://doi.org/10.3390/coatings13050924>
- Pu, Y., Zhang, D., Singh, P. M., & Ragauskas, A. J. (2008). The new forestry biofuels sector. In *Biofuels, Bioproducts and Biorefining* (Vol. 2, Issue 1, pp. 58–73). <https://doi.org/10.1002/bbb.48>
- Rajasekaran, P., Mertmann, P., Bibinov, N., Wandke, D., Viöl, W., & Awakowicz, P. (2010). Filamentary and homogeneous modes of dielectric barrier discharge (DBD) in air: Investigation through plasma characterization and simulation of surface irradiation. *Plasma Processes and Polymers*, 7(8), 665–675. <https://doi.org/10.1002/ppap.200900175>

- Ralph, J., MacKay, J. J., Hatfield, R. D., O'Malley, D. M., Whetten, R. W., & Sederoff, R. R. (1997). *Abnormal Lignin in a Loblolly Pine Mutant*.
<https://doi.org/10.1126/science.277.5323.235>
- Rebuzzi, F., & Evtuguin, D. V. (2005). Effect of glucuronoxylan on the hornification of *Eucalyptus globulus* bleached pulps. *Macromolecular Symposia*, 232, 121–128.
<https://doi.org/10.1002/masy.200551414>
- Reuter, R., Gherardi, N., & Benedikt, J. (2012a). Effect of N₂ dielectric barrier discharge treatment on the composition of very thin SiO₂-like films deposited from hexamethyldisiloxane at atmospheric pressure. *Applied Physics Letters*, 101(19).
<https://doi.org/10.1063/1.4764938>
- Reuter, R., Gherardi, N., & Benedikt, J. (2012b). Effect of N₂ dielectric barrier discharge treatment on the composition of very thin SiO₂-like films deposited from hexamethyldisiloxane at atmospheric pressure. *Applied Physics Letters*, 101(19).
<https://doi.org/10.1063/1.4764938>
- Ribeiro, R. A., Júnior, S. V., Jameel, H., Chang, H. M., Narron, R., Jiang, X., & Colodette, J. L. (2019). Chemical Study of Kraft Lignin during Alkaline Delignification of *E. urophylla* x *E. grandis* Hybrid in Low and High Residual Effective Alkali. *ACS Sustainable Chemistry and Engineering*, 7(12), 10274–10282.
<https://doi.org/10.1021/acssuschemeng.8b06635>
- Rincón, E., De Haro-Niza, J., Morcillo-Martín, R., Espinosa, E., & Rodríguez, A. (2023). Boosting functional properties of active-CMC films reinforced with agricultural residues-derived cellulose nanofibres. *RSC Advances*, 13(35), 24755–24766.
<https://doi.org/10.1039/d3ra04003h>

- Rodionova, G., Lenes, M., Eriksen, Ø., & Gregersen, Ø. (2011). Surface chemical modification of microfibrillated cellulose: Improvement of barrier properties for packaging applications. *Cellulose*, *18*(1), 127–134. <https://doi.org/10.1007/s10570-010-9474-y>
- Rodríguez Durán, I., Durocher-Jean, A., Profili, J., Stafford, L., & Laroche, G. (2020a). Atmospheric pressure Townsend discharges as a promising tool for the one-step deposition of antifogging coatings from N₂O/TMCTS mixtures. *Plasma Processes and Polymers*, *17*(7). <https://doi.org/10.1002/ppap.201900186>
- Rodríguez Durán, I., Durocher-Jean, A., Profili, J., Stafford, L., & Laroche, G. (2020b). Atmospheric pressure Townsend discharges as a promising tool for the one-step deposition of antifogging coatings from N₂O/TMCTS mixtures. *Plasma Processes and Polymers*, *17*(7). <https://doi.org/10.1002/ppap.201900186>
- Rojo, E., Peresin, M. S., Sampson, W. W., Hoeger, I. C., Vartiainen, J., Laine, J., & Rojas, O. J. (2015). Comprehensive elucidation of the effect of residual lignin on the physical, barrier, mechanical and surface properties of nanocellulose films. *Green Chemistry*, *17*(3), 1853–1866. <https://doi.org/10.1039/c4gc02398f>
- Santos, R. B., Capanema, E. A., Balakshin, M. Y., Chang, H. M., & Jameel, H. (2012). Lignin structural variation in hardwood species. *Journal of Agricultural and Food Chemistry*, *60*(19), 4923–4930. <https://doi.org/10.1021/jf301276a>
- Sasai, Y., Kondo, S., Yamauchi, Y., & Kuzuya, M. (2011). Cold Plasma Techniques for Pharmaceutical and Biomedical Engineering. In A. N. Laskovski (Ed.), *Biomedical Engineering* (p. Ch. 5). IntechOpen. <https://doi.org/10.5772/13366>

- Scallan, A. M., & Grignon, J. L. (1979). The effect of cations on pulp and paper properties. *Svensk Papperstidning-Nordisk Cellulosa*, 2, 40–47.
- Schaider, L. A., Balan, S. A., Blum, A., Andrews, D. Q., Strynar, M. J., Dickinson, M. E., Lunderberg, D. M., Lang, J. R., & Peaslee, G. F. (2017). Fluorinated Compounds in U.S. Fast Food Packaging. *Environmental Science and Technology Letters*, 4(3), 105–111. <https://doi.org/10.1021/acs.estlett.6b00435>
- Sehaqui, H., Kulasinski, K., Pfenninger, N., Zimmermann, T., & Tingaut, P. (2017). Highly Carboxylated Cellulose Nanofibers via Succinic Anhydride Esterification of Wheat Fibers and Facile Mechanical Disintegration. *Biomacromolecules*, 18(1), 242–248. <https://doi.org/10.1021/acs.biomac.6b01548>
- Sehaqui, H., Zimmermann, T., & Tingaut, P. (2014). Hydrophobic cellulose nanopaper through a mild esterification procedure. *Cellulose*, 21(1), 367–382. <https://doi.org/10.1007/s10570-013-0110-5>
- Shen, F., He, C., Wang, Y., Hu, J., Huang, M., Zhao, L., Zhang, S., Tian, D., & Shen, F. (2023). Fully upgrade lignocellulose to three nanomaterials by combinational pretreatment: Refining straw waste to pesticide nanocarrier. *Chemical Engineering Journal*, 467. <https://doi.org/10.1016/j.cej.2023.143376>
- Siró, I., & Plackett, D. (2010). Microfibrillated cellulose and new nanocomposite materials : a review. *Cellulose*, 17, 459–494. <https://doi.org/10.1007/s10570-010-9405-y>
- Solala, I., Iglesias, M. C., & Peresin, M. S. (2020). On the potential of lignin-containing cellulose nanofibrils (LCNFs): a review on properties and applications. *Cellulose*, 27(4), 1853–1877. <https://doi.org/10.1007/s10570-019-02899-8>

- Solala, I., Volperts, A., Andersone, A., Dizhbite, T., Mironova-Ulmane, N., Vehniäinen, A., Pere, J., & Vuorinen, T. (2012). Mechanoradical formation and its effects on birch kraft pulp during the preparation of nanofibrillated cellulose with Masuko refining. *Holzforchung*, 66(4), 477–483. <https://doi.org/10.1515/HF.2011.183>
- Solhi, L., Guccini, V., Heise, K., Solala, I., Niinivaara, E., Xu, W., Mihhels, K., Kröger, M., Meng, Z., Wohlert, J., Tao, H., Cranston, E. D., & Kontturi, E. (2023). Understanding Nanocellulose-Water Interactions: Turning a Detriment into an Asset. In *Chemical Reviews* (Vol. 123, Issue 5, pp. 1925–2015). American Chemical Society. <https://doi.org/10.1021/acs.chemrev.2c00611>
- Song, Z., Tang, J., Li, J., & Xiao, H. (2013). Plasma-induced polymerization for enhancing paper hydrophobicity. *Carbohydrate Polymers*, 92(1), 928–933. <https://doi.org/10.1016/j.carbpol.2012.09.089>
- Spence, K. L., Venditti, R. A., Rojas, O. J., Habibi, Y., & Pawlak, J. J. (2010). The effect of chemical composition on microfibrillar cellulose films from wood pulps: Water interactions and physical properties for packaging applications. *Cellulose*, 17(4), 835–848. <https://doi.org/10.1007/s10570-010-9424-8>
- Spence, K. L., Venditti, R. A., Rojas, O. J., Habibi, Y., & Pawlak, J. J. (2011). A comparative study of energy consumption and physical properties of microfibrillated cellulose produced by different processing methods. *Cellulose*, 18(4), 1097–1111. <https://doi.org/10.1007/s10570-011-9533-z>
- Spence, K. L., Venditti, R. A., Rojas, O. J., Pawlak, J. J., & Hubbe, M. A. (2011). WATER VAPOR BARRIER PROPERTIES OF COATED AND FILLED

MICROFIBRILLATED CELLULOSE COMPOSITE FILMS. *BioResources*, 6(4), 4370–4388.

Spori, D. M., Drobek, T., Zürcher, S., Ochsner, M., Sprecher, C., Mühlebach, A., & Spencer, N. D. (2008). Beyond the lotus effect: Roughness influences on wetting over a wide surface-energy range. *Langmuir*, 24(10), 5411–5417. <https://doi.org/10.1021/la800215r>

Steven, M. D., & Hotchkiss, J. H. (2002a). Comparison of flat film to total package water vapour transmission rates for several commercial food wraps. *Packaging Technology and Science*, 15(1), 17–27. <https://doi.org/10.1002/pts.562>

Steven, M. D., & Hotchkiss, J. H. (2002b). Comparison of flat film to total package water vapour transmission rates for several commercial food wraps. *Packaging Technology and Science*, 15(1), 17–27. <https://doi.org/10.1002/pts.562>

Sulis, D. B., Jiang, X., Yang, C., Marques, B. M., Matthews, M. L., Miller, Z., Lan, K., Cofre-Vega, C., Liu, B., Sun, R., Sederoff, H., Bing, R. G., Sun, X., Williams, C. M., Jameel, H., Phillips, R., Chang, H.-M., Peszlen, I., Huang, Y.-Y., ... Wang, J. P. (2023). *Multiplex CRISPR editing of wood for sustainable fiber production*. <https://doi.org/10.1126/science.add4514>

Svagan, A. J., Azizi Samir, M. A. S., & Berglund, L. A. (2007). Biomimetic polysaccharide nanocomposites of high cellulose content and high toughness. *Biomacromolecules*, 8(8), 2556–2563. <https://doi.org/10.1021/bm0703160>

T 248 sp-00. (2000). *T 248 sp-00 Laboratory beating of pulp (PFI mill method)*.

TAPPI 410 om. (2008). *Grammage of paper and paperboard (weight per unit area)*.

TAPPI 441 om-09. (2013). *T441- Water absorption*.

TAPPI WI 3021. (2013). *TAPPI WI 3021*.

- Tarrés, Q., Oliver-Ortega, H., Ferreira, P. J., Àngels Pèlach, M., Mutjé, P., & Delgado-Aguilar, M. (2018). Towards a new generation of functional fiber-based packaging: cellulose nanofibers for improved barrier, mechanical and surface properties. *Cellulose*, 25(1), 683–695. <https://doi.org/10.1007/s10570-017-1572-7>
- Tayeb, A. H., Tajvidi, M., & Bousfield, D. (2020). Paper-based oil barrier packaging using lignin-containing cellulose nanofibrils. *Molecules*, 25(6). <https://doi.org/10.3390/molecules25061344>
- Taylor, L., Phipps, J., Blackburn, S., Greenwood, R., & Skuse, D. (2020). Using fibre property measurements to predict the tensile index of microfibrillated cellulose nanopaper. *Cellulose*, 27(11), 6149–6162. <https://doi.org/10.1007/s10570-020-03226-2>
- Tendero, C., Tixier, C., Tristant, P., Desmaison, J., & Leprince, P. (2006). Atmospheric pressure plasmas: A review. In *Spectrochimica Acta - Part B Atomic Spectroscopy* (Vol. 61, Issue 1, pp. 2–30). Elsevier. <https://doi.org/10.1016/j.sab.2005.10.003>
- Theelen, M., Habets, D., Staemmler, L., Winands, H., & Bolt, P. (2012). Localised plasma deposition of organosilicon layers on polymer substrates. *Surface and Coatings Technology*, 211, 9–13. <https://doi.org/10.1016/j.surfcoat.2011.10.022>
- Todd Ryan, E., Gates, S. M., Cohen, S. A., Ostrovski, Y., Adams, E., Virwani, K., & Grill, A. (2014). Effect of low-frequency radio frequency on plasma-enhanced chemical vapor deposited ultra low- κ dielectric films for very large-scale integrated interconnects. *Journal of Applied Physics*, 115(14). <https://doi.org/10.1063/1.4870453>
- Tóth, A., Černáková, L., Černák, M., & Kunovská, K. (2007). Surface analysis of groundwood paper treated by diffuse coplanar surface barrier discharge (DCSBD) type

atmospheric plasma in air and in nitrogen. *Holzforschung*, 61(5), 528–531.

<https://doi.org/10.1515/HF.2007.080>

Trache, D., Tarchoun, A. F., Derradji, M., Hamidon, T. S., Masruchin, N., Brosse, N., & Hussin, M. H. (2020). Nanocellulose: From Fundamentals to Advanced Applications. In *Frontiers in Chemistry* (Vol. 8). Frontiers Media S.A.

<https://doi.org/10.3389/fchem.2020.00392>

Trovagunta, R., Kelley, S. S., & Lavoine, N. (2021). Highlights on the mechanical pre-refining step in the production of wood cellulose nanofibrils. *Cellulose*, 28(18), 11329–11344. <https://doi.org/10.1007/s10570-021-04226-6>

Tsalagkas, D., Zhai, L., Kafy, A., Kim, J. W., Kim, H. C., & Kim, J. (2020). Production of Micro- and Nanofibrillated Cellulose through an Aqueous Counter Collision System Followed by Ultrasound: Effect of Mechanical Pretreatments. *Journal of Natural Fibers*, 17(8), 1099–1110. <https://doi.org/10.1080/15440478.2018.1558144>

Turbak, A., Snyder, F., & Sandberg, K. (1983). MICROFIBRILLATED CELLULOSE, A NEW CELLULOSE PRODUCT: PROPERTIES, USES, AND COMMERCIAL POTENTIAL. *Journal of Applied Polymer Science: Applied Polymer Symposium*, 37, 815–827.

Tyl, C., Lin, X., Bouzidi, M. C., Dap, S., Caquineau, H., Ségur, P., Gherardi, N., & Naudé, N. (2018). Investigation of memory effect in atmospheric pressure dielectric barrier discharge in nitrogen with small oxygen or nitric oxide addition. *Journal of Physics D: Applied Physics*, 51(35). <https://doi.org/10.1088/1361-6463/aad472>

Ügdüler, S., De Somer, T., Van Geem, K. M., Roosen, M., Kulawig, A., Leineweber, R., & De Meester, S. (2021). Towards a Better Understanding of Delamination of Multilayer

Flexible Packaging Films by Carboxylic Acids. *ChemSusChem*, 14(19), 4198–4213.

<https://doi.org/10.1002/cssc.202002877>

UM 256. (1991). *Water retention value (WRV)*.

U.S. Plastic Pact: 2021 Annual report. (2021). *U.S. Plastics Pact: 2021 Annual report*.

<https://usplasticspact.org/2021-report/>

Utsunomiya, H., Tsujita, Y., & Kondo, T. (2022). Cellulose nanoanemone: an asymmetric form of nanocellulose. *Cellulose*, 29(5), 2899–2916. <https://doi.org/10.1007/s10570-021-04231-9>

Vähä-Nissi, M., Koivula, H. M., Räisänen, H. M., Vartiainen, J., Ragni, P., Kenttä, E., Kaljunen, T., Malm, T., Minkkinen, H., & Harlin, A. (2017). Cellulose nanofibrils in biobased multilayer films for food packaging. *Journal of Applied Polymer Science*, 134(19). <https://doi.org/10.1002/app.44830>

Van Assche, F. J. H., Unnikrishnan, S., Michels, J. J., Van Mol, A. M. B., Van De Weijer, P., Van De Sanden, M. C. M., & Creatore, M. (2014). On the intrinsic moisture permeation rate of remote microwave plasma-deposited silicon nitride layers. *Thin Solid Films*, 558, 54–61. <https://doi.org/10.1016/j.tsf.2014.02.069>

Van Hai, L., Zhai, L., Kim, H. C., Kim, J. W., Choi, E. S., & Kim, J. (2018). Cellulose nanofibers isolated by TEMPO-oxidation and aqueous counter collision methods. *Carbohydrate Polymers*, 191(December 2017), 65–70.

<https://doi.org/10.1016/j.carbpol.2018.03.008>

Vander Wielen, L. C., Östenson, M., Gatenholm, P., & Ragauskas, A. J. (2006). Surface modification of cellulosic fibers using dielectric-barrier discharge. *Carbohydrate Polymers*, 65(2), 179–184. <https://doi.org/10.1016/j.carbpol.2005.12.040>

- Vartiainen, J., & Malm, T. (2016). Surface hydrophobization of CNF films by roll-to-roll HMDSO plasma deposition. *Journal of Coatings Technology and Research*, 13(6), 1145–1149. <https://doi.org/10.1007/s11998-016-9833-1>
- Vartiainen, J., Pasanen, S., Kenttä, E., & Vähä-Nissi, M. (2018). Mechanical recycling of nanocellulose containing multilayer packaging films. *Journal of Applied Polymer Science*, 135(19). <https://doi.org/10.1002/app.46237>
- Vera, R. E., Suarez, A., Zambrano, F., Marquez, R., Bedard, J., Vivas, K. A., Pifano, A., Farrell, M., Ankeny, M., Jameel, H., & Gonzalez, R. (2023). Upcycling cotton textile waste into bio-based building blocks through an environmentally friendly and high-yield conversion process. *Resources, Conservation and Recycling*, 189(July 2022), 106715. <https://doi.org/10.1016/j.resconrec.2022.106715>
- Vigneshwaran, N., Satyamurthy, P., & Jain, P. (2015). Biological Synthesis of Nanocrystalline Cellulose by Controlled Hydrolysis of Cotton Fibers and Linters. In *Handbook of Polymer Nanocomposites. Processing, Performance and Application*. Springer, Berlin, Heidelberg. [https://doi.org/https://doi.org/10.1007/978-3-642-45232-1_62](https://doi.org/10.1007/978-3-642-45232-1_62)
- Wang, J., Gardner, D. J., Stark, N. M., Bousfield, D. W., Tajvidi, M., & Cai, Z. (2018). Moisture and Oxygen Barrier Properties of Cellulose Nanomaterial-Based Films. *ACS Sustainable Chemistry and Engineering*, 6(1), 49–70. <https://doi.org/10.1021/acssuschemeng.7b03523>
- Wang, J. P., Matthews, M. L., Williams, C. M., Shi, R., Yang, C., Tunlaya-Anukit, S., Chen, H. C., Li, Q., Liu, J., Lin, C. Y., Naik, P., Sun, Y. H., Loziuk, P. L., Yeh, T. F., Kim, H., Gjersing, E., Shollenberger, T., Shuford, C. M., Song, J., ... Chiang, V. L. (2018).

- Improving wood properties for wood utilization through multi-omics integration in lignin biosynthesis. *Nature Communications*, 9(1). <https://doi.org/10.1038/s41467-018-03863-z>
- Wang, Q., Chen, W., Zhu, W., McClements, D. J., Liu, X., & Liu, F. (2022). A review of multilayer and composite films and coatings for active biodegradable packaging. *Npj Science of Food*, 6(1). <https://doi.org/10.1038/s41538-022-00132-8>
- Wang, W., Gu, F., Deng, Z., Zhu, Y., Zhu, J., Guo, T., Song, J., & Xiao, H. (2021). Multilayer surface construction for enhancing barrier properties of cellulose-based packaging. *Carbohydrate Polymers*, 255. <https://doi.org/10.1016/j.carbpol.2020.117431>
- Wang, W., Guo, T., Sun, K., Jin, Y., Gu, F., & Xiao, H. (2019). Lignin redistribution for enhancing barrier properties of cellulose-based materials. *Polymers*, 11(12). <https://doi.org/10.3390/polym11121929>
- Wang, W., Sabo, R. C., Mozuch, M. D., Kersten, P., Zhu, J. Y., & Jin, Y. (2015). Physical and Mechanical Properties of Cellulose Nanofibril Films from Bleached Eucalyptus Pulp by Endoglucanase Treatment and Microfluidization. *Journal of Polymers and the Environment*, 23(4), 551–558. <https://doi.org/10.1007/s10924-015-0726-7>
- Wu, Y., Gao, X., Wu, J., Zhou, T., Nguyen, T. T., & Wang, Y. (2023). Biodegradable Polylactic Acid and Its Composites: Characteristics, Processing, and Sustainable Applications in Sports. In *Polymers* (Vol. 15, Issue 14). Multidisciplinary Digital Publishing Institute (MDPI). <https://doi.org/10.3390/polym15143096>
- Yang, X., Li, R., & Liu, N. (2024). Effect of remote Plasma assisted WPU/CNF multilayer coating assembly on PLA film properties. *Colloids and Surfaces A: Physicochemical and Engineering Aspects*, 688. <https://doi.org/10.1016/j.colsurfa.2024.133519>

- Yu, J., Zhu, Y., Ma, H., Liu, L., Hu, Y., Xu, J., Wang, Z., & Fan, Y. (2019). Contribution of hemicellulose to cellulose nanofiber-based nanocomposite films with enhanced strength, flexibility and UV-blocking properties. *Cellulose*, 26(10), 6023–6034.
<https://doi.org/10.1007/s10570-019-02518-6>
- Zhai, L., Kim, H. C., Kim, J. W., Kang, J., & Kim, J. (2018). Elastic moduli of cellulose nanofibers isolated from various cellulose resources by using aqueous counter collision. *Cellulose*, 25(7), 4261–4268. <https://doi.org/10.1007/s10570-018-1836-x>
- Zhang, J., Wavhal, D. S., & Fisher, E. R. (2004). Mechanisms of SiO₂ film deposition from tetramethylcyclotetrasiloxane, dimethyldimethoxysilane, and trimethylsilane plasmas. *Journal of Vacuum Science & Technology A: Vacuum, Surfaces, and Films*, 22(1), 201–213. <https://doi.org/10.1116/1.1635392>
- Zhang, X., Zhang, L., Fan, Y., & Wang, Z. (2023). The case-dependent lignin role in lignocellulose nanofibers preparation and functional application-A review. In *Green Energy and Environment* (Vol. 8, Issue 6, pp. 1553–1566). KeAi Publishing Communications Ltd. <https://doi.org/10.1016/j.gee.2022.09.008>
- Zhao, Y. W., Tian, M. Z., & Huang, P. (2021). Starch/clay aerogel reinforced by cellulose nanofibrils for thermal insulation. *Cellulose*, 28(6), 3505–3513.
<https://doi.org/10.1007/s10570-021-03750-9>

APPENDICES

Appendix A: Supporting information for Chapter 2 Tailoring cellulose nanofibrils films for improved performance through optimization of aqueous counter collision processing conditions

Table 1: Compositional analysis of Never-dried bleached softwood Kraft pulp (NBSK)

Sample	(%)	Standard deviation
Glucan	81.0	0.3
Xylan	9.5	0.1
Galactan	0.69	0.0
Arabinan+Mannan	8.0	0.0
Klason	1.11	0.2
Acid Soluble	0.6	0.2
Total lignin	1.7	0.2
Ash	0.0	0.0

Table 2 - Summary of mechanical and physical properties of CNFs films

Sample	Factors			EC _{Low}			EC _{High}		
	Passes	pressure (MPa)	Concentration (wt. %)	Grammage (g/m ²)	Density (g/cm ³)	TI (MPa.m ² /g)	Grammage (g/m ²)	Density (g/cm ³)	TI (MPa.m ² /g)
1	6	120	0.1	9 ± 2 ^{a,b}	0.5 ± 0.1 ^{a-d}	58 ± 5	11 ± 1 ^{a,b}	1.2 ± 0.3 ^{a-d}	57 ± 3
2	1	170	0.1	10 ± 1 ^{a,b}	0.4 ± 0.1 ^{c,d}	50 ± 9	10 ± 0 ^{a,b,c}	0.9 ± 0.1 ^d	62 ± 4
3	11	170	0.1	10 ± 0 ^{a,b}	0.8 ± 0.1 ^a	42 ± 6	11 ± 1 ^{a,b}	1.2 ± 0.1 ^{b-d}	49 ± 2
4	6	220	0.1	11 ± 1 ^{a,b}	0.6 ± 0.1 ^{a-d}	46 ± 12	9 ± 0 ^c	1.7 ± 0.4 ^a	71 ± 6
5	1	120	0.33	13 ± 0 ^a	0.5 ± 0.1 ^{b,c,d}	53 ± 2	9 ± 0 ^c	1 ± 0.2 ^d	65 ± 5
6	11	120	0.33	8 ± 1 ^{a,b}	0.6 ± 0.1 ^{a-d}	7 ± 1	10 ± 1 ^{b,c}	1 ± 0.2 ^d	30 ± 12
7	6	170	0.33	12 ± 3 ^b	0.7 ± 0.1 ^{a-c}	20 ± 5	11 ± 1 ^{a,b}	1 ± 0.2 ^d	55 ± 8
8	6	170	0.33	8 ± 1 ^{a,b}	0.7 ± 0.1 ^{a-c}	15 ± 6	12 ± 1 ^a	1 ± 0.2 ^d	47 ± 4
9	6	170	0.33	11 ± 2 ^{a,b}	0.7 ± 0.1 ^{a-c}	8 ± 6	12 ± 1 ^a	1 ± 0.2 ^d	56 ± 27
10	1	220	0.33	10 ± 1 ^{a,b}	0.4 ± 0.1 ^d	52 ± 4	11 ± 1 ^{a,b}	1.2 ± 0.2 ^{a-d}	57 ± 7
11	11	220	0.33	9 ± 2 ^{a,b}	0.7 ± 0.1 ^{a-c}	35 ± 3	11 ± 1 ^{a,b}	1.6 ± 0.2 ^{a,b}	33 ± 7
12	6	120	0.55	10 ± 1 ^{a,b}	0.6 ± 0.1 ^{a-d}	59 ± 13	10 ± 1 ^{b,c}	1.1 ± 0.1 ^{c,d}	68 ± 4
13	1	170	0.55	10 ± 1 ^{a,b}	0.5 ± 0.1 ^{a-d}	59 ± 10	11 ± 0 ^{a,b}	1.2 ± 0.3 ^{a-d}	61 ± 5
14	11	170	0.55	9 ± 2 ^{a,b}	0.6 ± 0.1 ^{a-d}	32 ± 6	10 ± 1 ^{a-c}	1.1 ± 0.1 ^d	42 ± 10
15	6	220	0.55	12 ± 1 ^{a,b}	0.6 ± 0.2 ^{a-d}	50 ± 10	11 ± 1 ^{a,b}	1.6 ± 0.2 ^{a-c}	66 ± 10
Masuko	-	-	-	12 ± 1	0.4 ± 0.1	31 ± 2	10 ± 1	1.1 ± 0.1	66 ± 9

^{a-d} Means in the same column that do not share a letter are significantly different at the 0.05 level of confidence - One way

ANOVA – Tukey test.

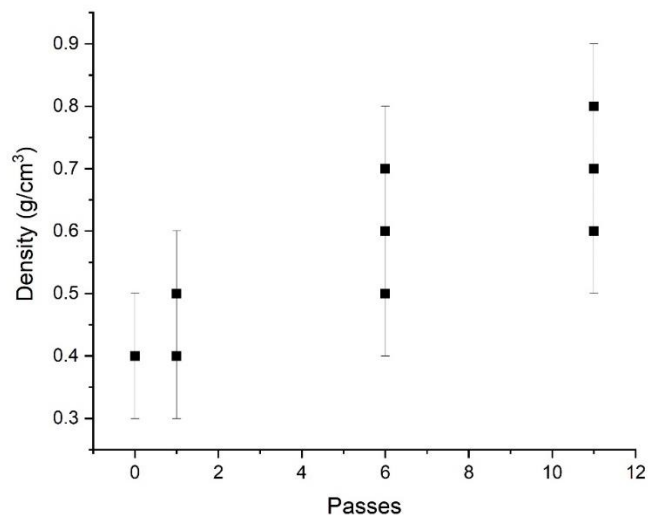


Fig S1. Density of EC_{Low}-CNFs at the 0.05 level of confidence, the population means are significantly different.

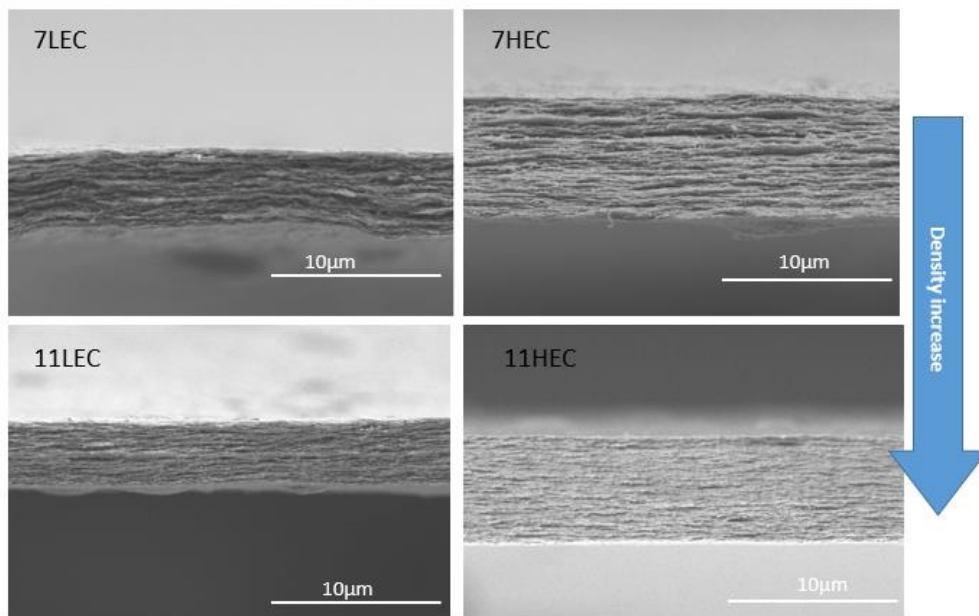


Fig S2. SEM images of the cross-sectional area of CNF films – Left samples 7 and 11 LEC, right: 7 and 11 HEC. Samples 7 and 11 LEC had porosity of 50% - Samples 7 and 11 HEC had a porosity of 0 and 30%

Table 4 – Water Vapor Barrier after ACC treatments

<i>Passes</i>	<i>Pressure (MPa)</i>	<i>Concentration (wt%)</i>	<i>WVP (g/Pa*s* m.10⁻¹⁰)</i>	<i>WVP std</i>	<i>WVTR g/(day*m²)</i>	<i>WVTR std</i>	<i>AR Sedimentation n</i>	<i>Diameter (nm)</i>	<i>Transmittance 500 nm</i>
6	120	0.1	0.173	4.32E-12	210	0	-	-	93
1	170	0.1	0.170	1.06E-12	270	0	-	-	89
11	170	0.1	0.147	2.12E-13	197	9	-	-	98
6	220	0.1	0.103	1.61E-13	207	2	-	-	97
1	120	0.33	0.200	6.36E-13	220	21	-	-	90
11	120	0.33	0.163	2.27E-12	197	5	80 ± 1	-	95
6	170	0.33	0.203	3.29E-12	236	30	-	-	95
6	170	0.33	0.215	6.95E-12	251	38	-	29 ± 8	96
6	170	0.33	0.237	7.07E-14	274	65	-	-	96
1	220	0.33	0.127	7.07E-14	191	1	-	-	90
11	220	0.33	0.144	3.34E-13	247	1	-	-	98
6	120	0.55	0.190	5.13E-12	284	69	-	-	92
1	170	0.55	0.191	7.07E-13	168	41	254 ± 0	-	88
11	170	0.55	0.153	9.90E-13	179	6	-	35 ± 11	96
6	220	0.55	0.132	1.5E-13	190	11	213 ± 1	17 ± 6	96
EC _{high} CMF	-	-	0.210	4.32E-12	230	1	145 ± 0	-	91

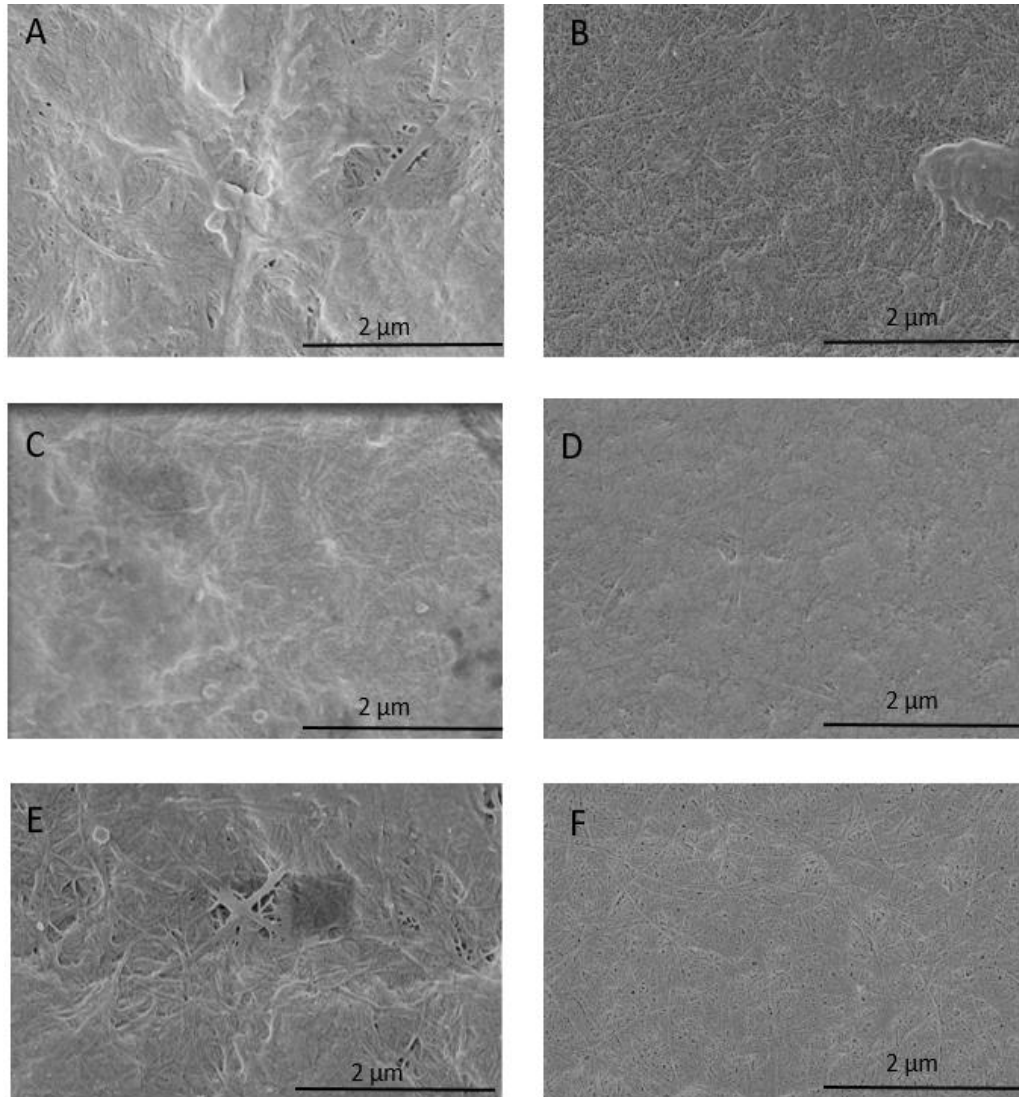


Fig S3. SEM: a) 1 and b) 11 passes at 0.10wt% and 170 MPa; c) 1 and 11 passes 0.33 wt% and 220MPa; e) 1 and b) 11 passes at 0.55 wt% and 170 MPa

Design of experiment code for JMP

```
DOE(
Make Table}
Response Surface Design,
{Add Response( Maximize, "Tensile Index", 30, 100, . ),
```

Add Response(Minimize, "WVP", 0, 1.1, .),
Change Factor Settings(1, 1, 11, "Passes"),
Change Factor Settings(2, 120, 220, "Pressure"),
Add Factor(Continuous, 0.1, 0.55, "Concentration", 0),
Set Random Seed(193144669), Make Design(1), Center Points(3),
Simulate Responses(0), Save X Matrix(0), Set Run Order(Sort Right to Left),

Appendix B: Supporting information for Chapter 3: Tuning the Surface Chemistry and Properties of Cellulose Nanofibril (CNF) Films by Dielectric Barrier Discharge (DBD) Plasma for Packaging Applications

Fig. S1 Plasma reactor

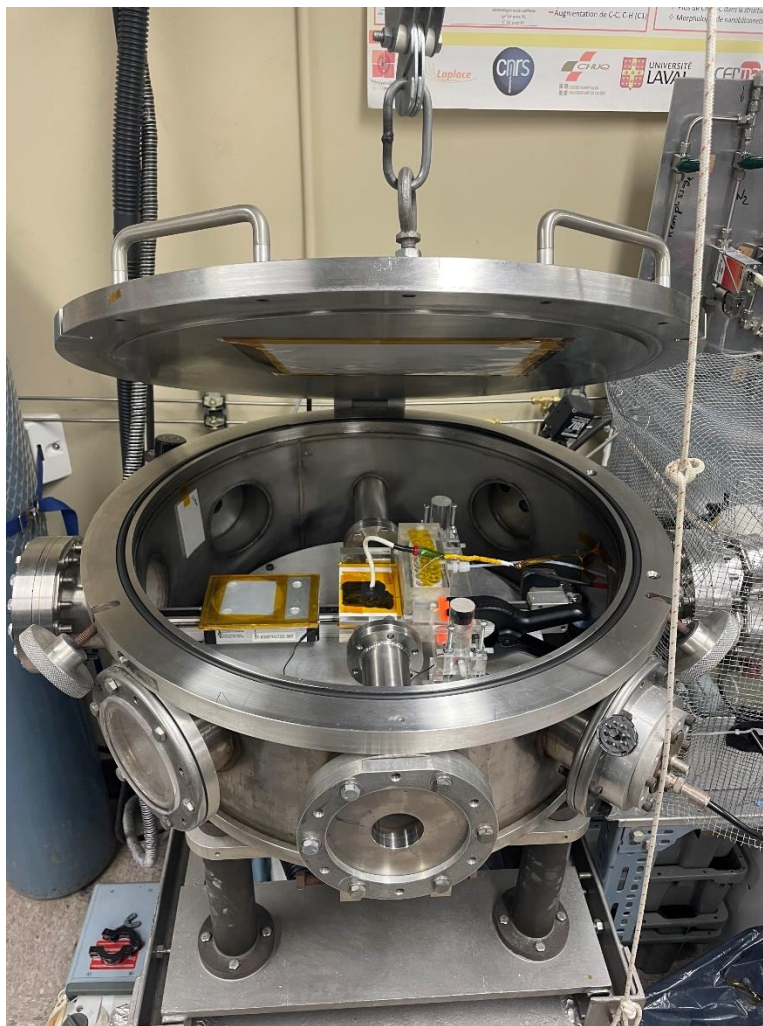


Figure S2; Atomic Force Microscopy images of organosilicon layer with the deposition in the static mode

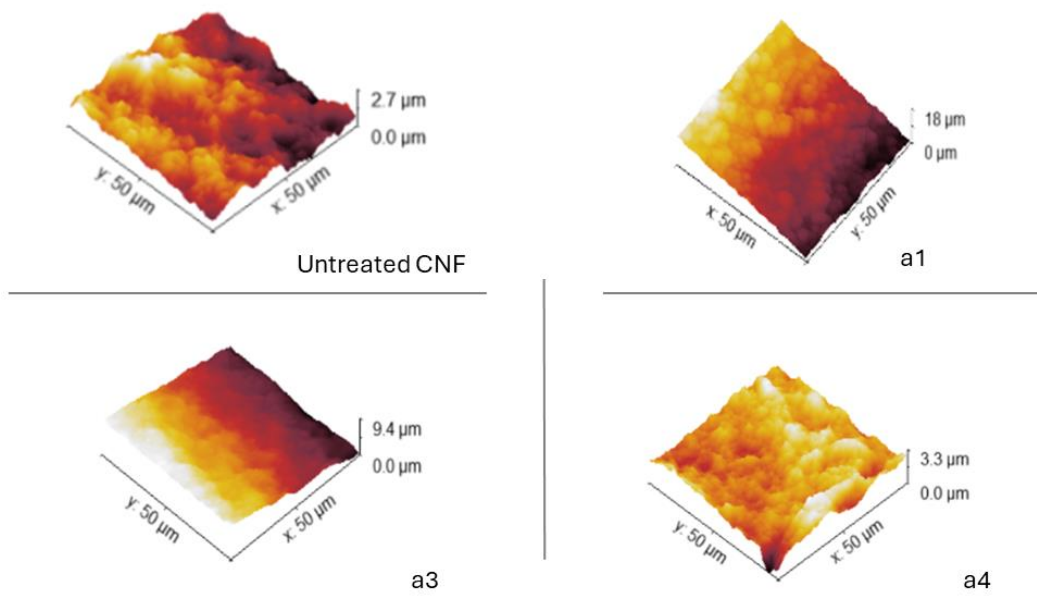
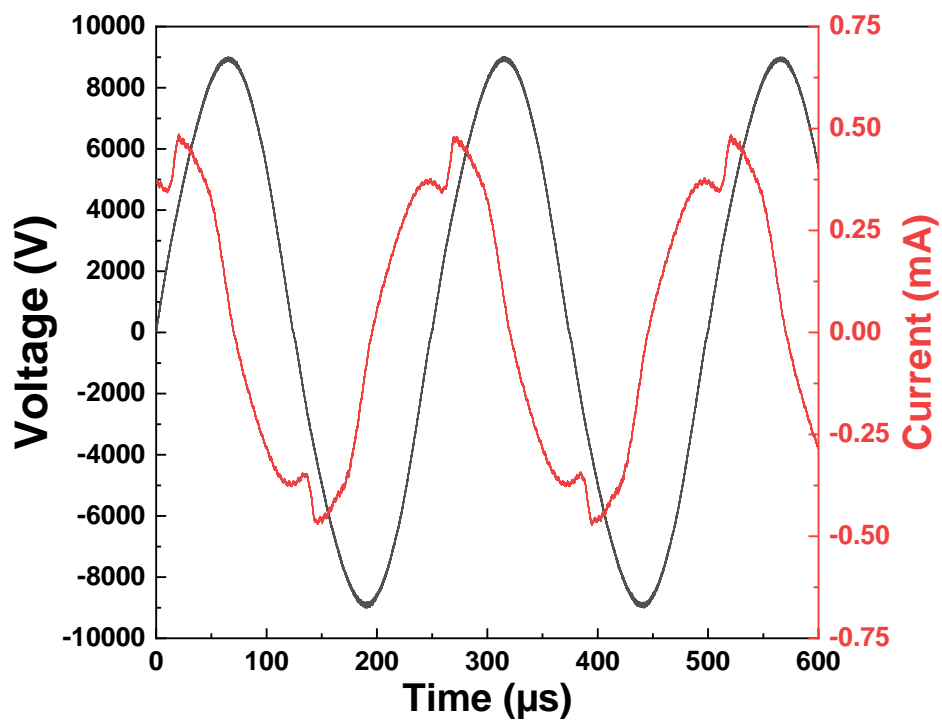


Figure S3 Townsend plasma discharge N_2 + TMCTS and CNF film



Appendix 3

Figure S4: Theoretical coating thickness and water contact angles in the static mode and comparison with dynamic mode

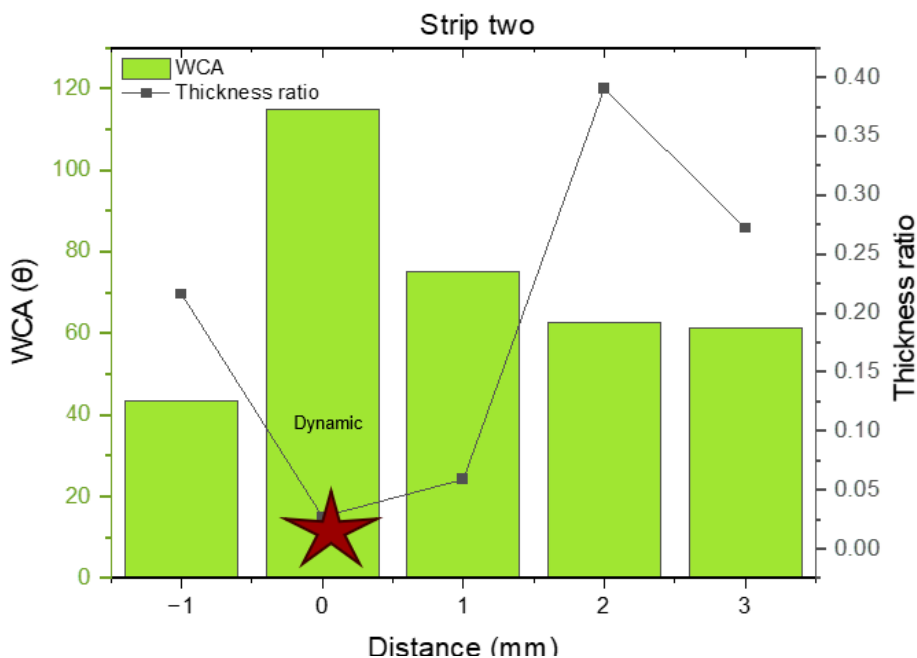
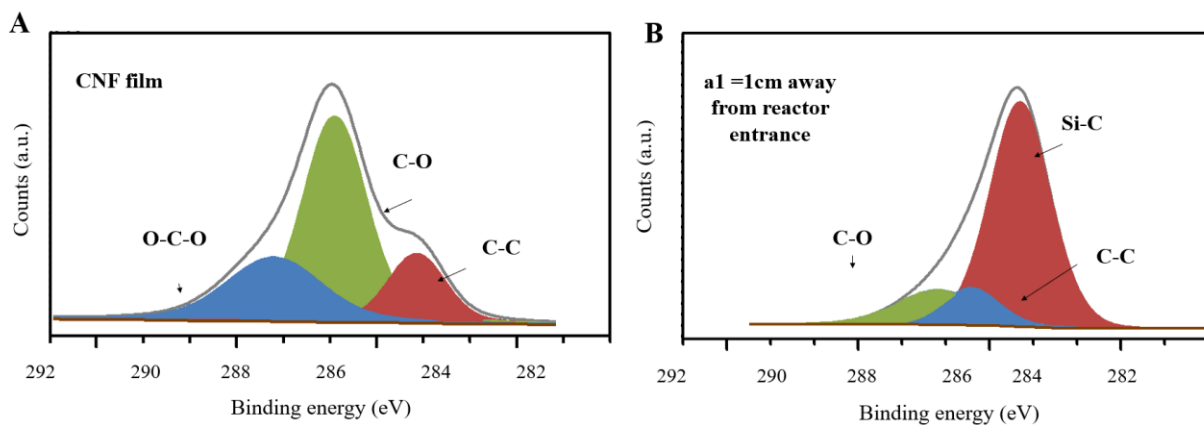
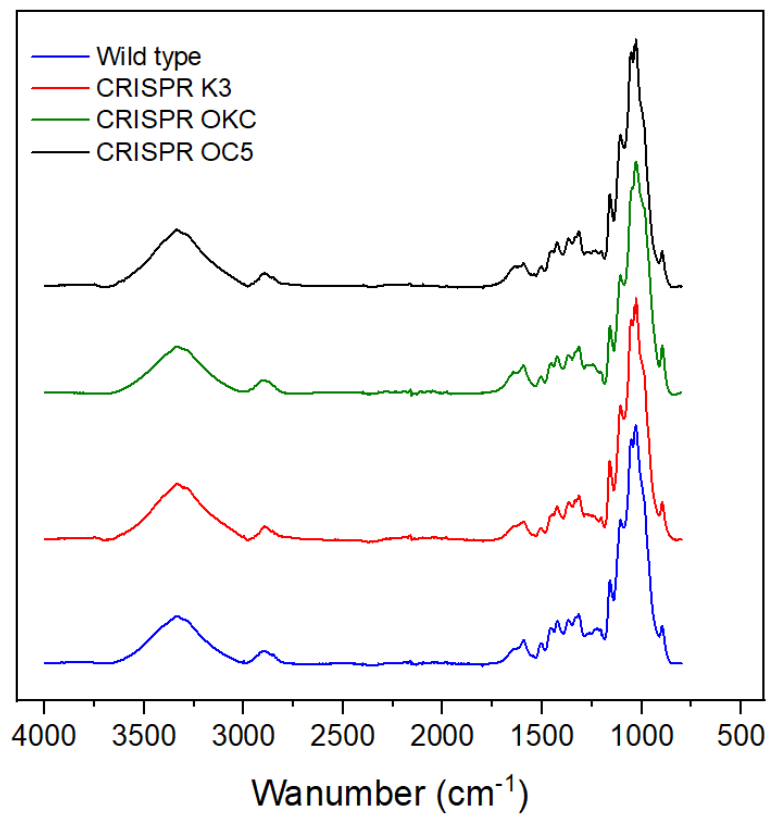


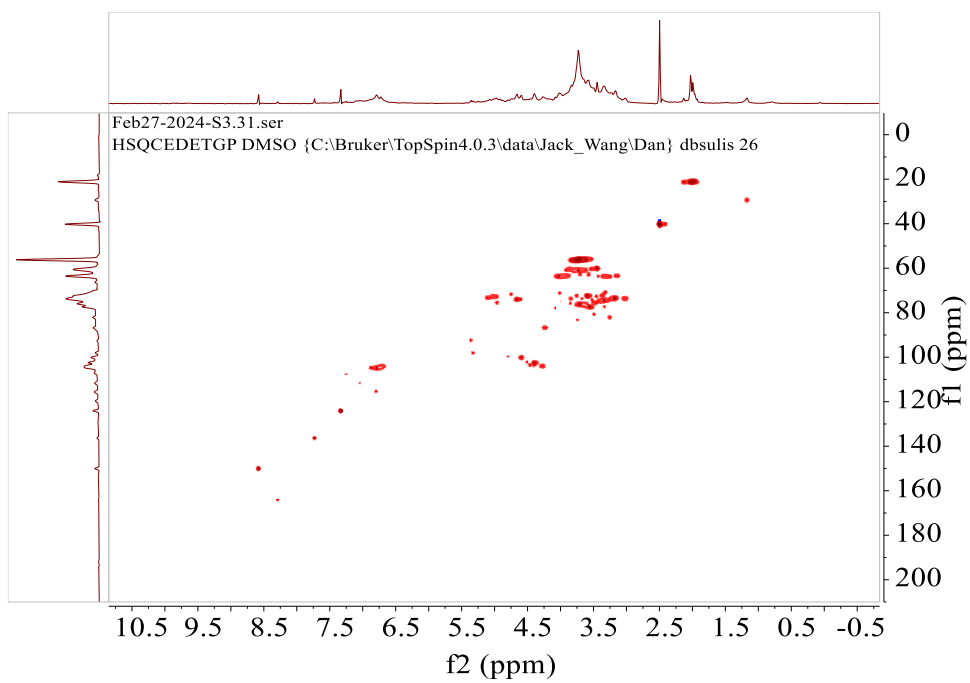
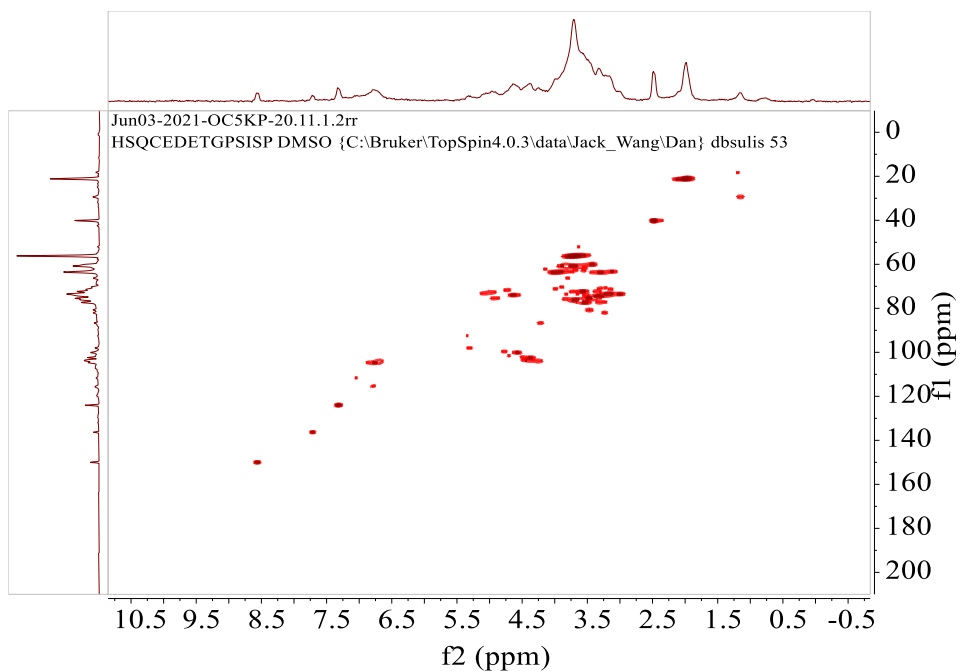
Figure S5. Deconvoluted Carbon 1s photoelectron spectrum of (A) Untreated CNF films, (B) after organosilicon deposition by plasma in the static mode at a1=1 cm away from the reactor entrance.



Appendix C: Supporting information for Chapter 4: Understanding the Effect of Residual Lignin on the Processing-Structure-Properties of Lignin-Containing Cellulose Nanofibrils

Fig S1: ATR- FTIR of Wildtype and CRISPR pulps and HQSC





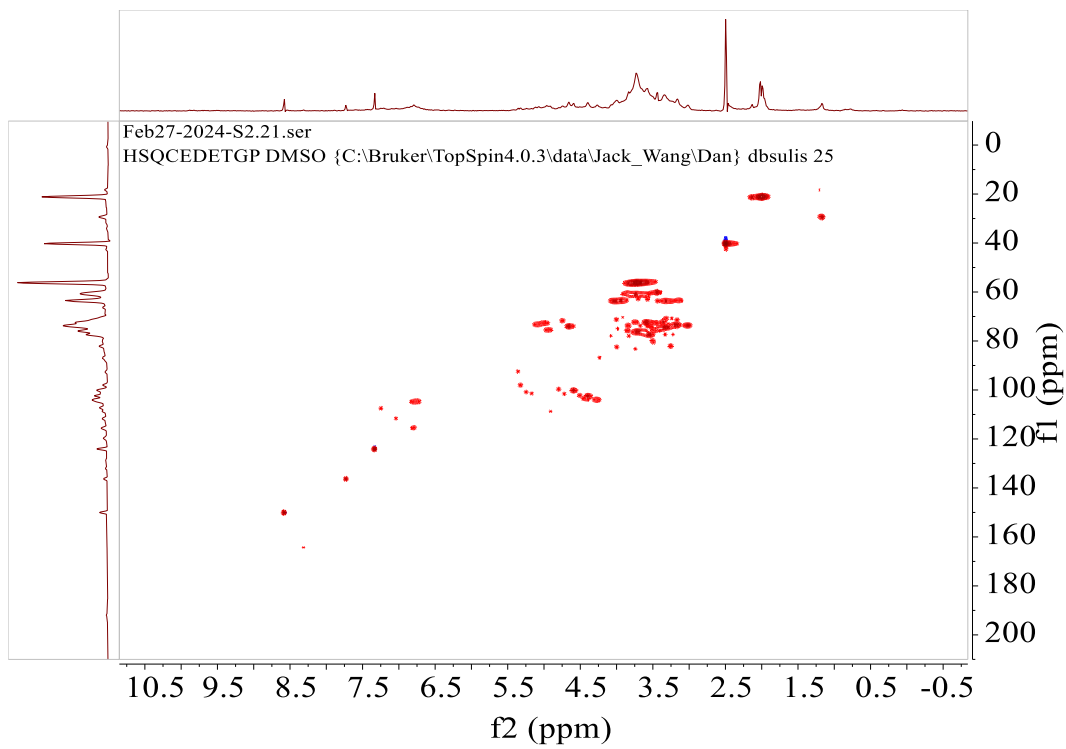
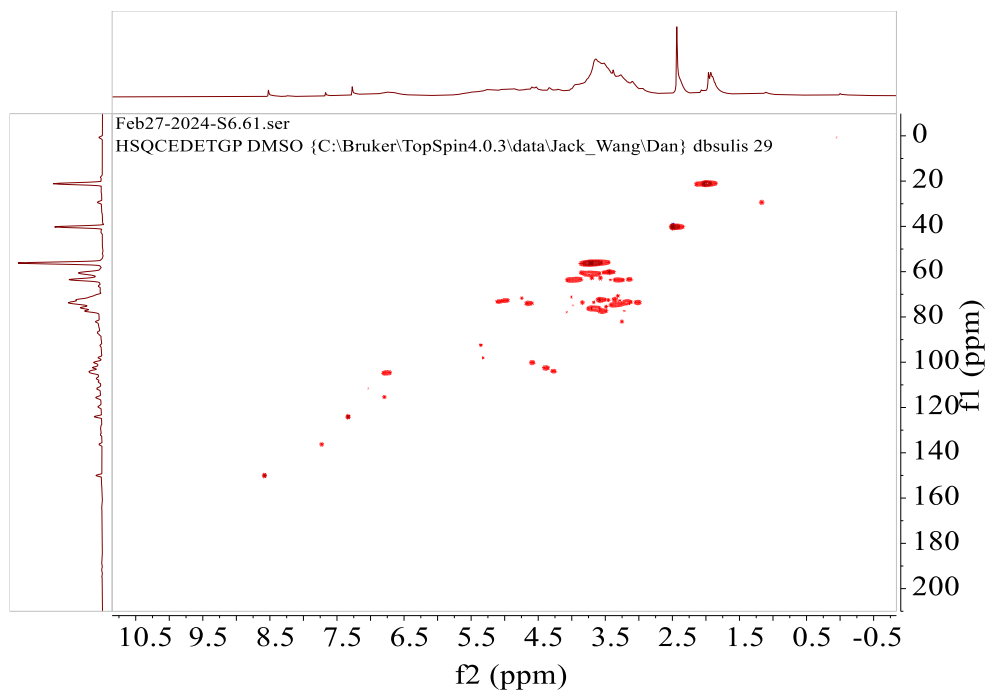
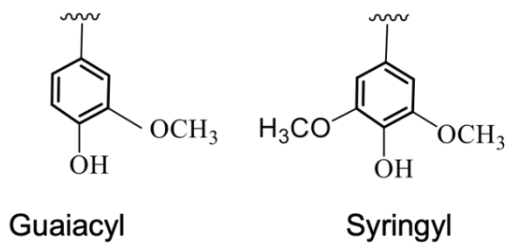


Fig S2: Lignin substructures; Guaiacyl and syringil and lignin interunit linkages

Lignin composition



Lignin Interunit Linkages

